Master Thesis

Faculty of Science

University of Bern

Global Assessment of Marine Heatwaves and Their Impact on Sea-Air CO_2 Fluxes

---

Handed in by Catherine Li

Supervisor: Prof. Dr. Thomas Frölicher
Co-supervisor: Prof. Dr. Christoph Raible
Advisor: Dr. Friedrich Burger

January 2024

Acknowledgements

I would like to sincerely thank my supervisor, Thomas Frölicher, for his valuable time and patience in guiding me through this thesis. I also want to thank Friedrich Burger, as I am extremely grateful for the time he dedicated to helping me think through things, answering my questions, and all the troubleshooting. Lastly, I want to thank the Ocean Modelling Group at KUP for welcoming me and providing an enjoyable working environment.

Contents

1 Abstract

The exchange of carbon dioxide (CO_2) between the atmosphere and ocean encompasses a critical role in the global carbon cycle. Currently, the global ocean acts as a net sink absorbing atmospheric CO_2 and contributing to the mitigation of anthropogenic CO_2 emissions. The flux of CO_2 between the ocean and atmosphere is mainly caused by the differences in partial pressure of CO_2 in the surface ocean and overlying air. The partial pressure of CO_2 (pCO_2) in seawater varies with temperature, making the flux of CO_2 highly sensitive to changes in sea surface temperature. Periods of extremely warm sea surface temperature - also known as marine heatwaves are increasing in frequency, duration, and intensity in all ocean basins due to anthropogenic climate change. These extremely warm sea surface temperatures have the potential to alter the flux of CO_2 between the ocean and atmosphere. The dynamics of marine heatwaves and their impact on sea-air CO_2 fluxes has recently gained attention with studies investigating specific regions or specific marine heatwave events and their impacts on sea-air CO_2 fluxes. However, a global assessment of the impacts and drivers of marine heatwaves on sea-air CO_2 fluxes is currently lacking.

In this thesis we consider observation-based data and Earth System model data to assess the impacts of marine heatwaves on monthly mean sea-air CO_2 fluxes from 1990 to 2019. The sea-air CO_2 flux anomalies are then decomposed into the six driving factors: solubility, gas transfer velocity, oceanic partial pressure of CO_2, atmospheric partial pressure of CO_2, and sea ice. Oceanic partial pressure of CO_2, the dominating term driving the flux anomalies during marine heatwaves is further broken down into its contributing terms.

Averaged across the global ocean, we find a reduction in the sea-air CO_2 flux of 0.126 (-0.144 to 0.427) PgC/yr (observation-based data) and 0.717 (0.622 to 0.838) PgC/yr (model-based data). These reductions are mainly caused by increases in the partial pressure of CO_2 in the ocean. Results show the anomalies of oceanic partial pressure of CO_2 during marine heatwaves are a net result of two competing mechanisms: a thermal effect and a dissolved inorganic carbon (DIC) effect. In agreement with previous findings, a substantial reduction in the equatorial Pacific's mean outgassing flux -0.086 (-0.135 to -0.008) PgC/yr (observation-based) and -0.143 (-0.190 to -0.091) PgC/yr (model), is due to lower than usual oceanic pCO_2, caused by anomalously low DIC. In this tropical outgassing region, the DIC driven decrease in oceanic pCO_2 outweighs the thermally driven increase in oceanic pCO_2. For the low to mid latitudes, which are generally characterized by a net uptake of CO_2, the thermal effect on oceanic pCO_2 dominates during marine heatwaves. This leads to higher than usual pCO_2 in the ocean and as a result anomalous outgassing of CO_2 in these regions. In the high latitudes, there is greater variation in the mean sea-air CO_2 flux, which leads to more areas of potential mismatch in terms of the flux anomalies during MHWs and their drivers between the observation-based and model data. The model data suggests flux anomalies in the high latitudes are mainly due to the thermally-driven increase in oceanic pCO_2. The observation-based data suggests flux anomalies in the high latitudes are also driven by the non-thermal DIC effect on oceanic pCO_2, depending on the specific region. Mismatch in the high latitudes and Southern Ocean can be partly attributed to the coarse horizontal resolution of the ESM model and monthly temporal resolution of the analysis.

In general, we find the ESM model is able to represent well the sea-air CO_2 fluxes and anomalies

during MHWs as well as the drivers of such flux anomalies compared to the observation-based data.

2 Introduction

The ocean and the exchange of carbon dioxide (CO_2) between the ocean and the atmosphere play a critical role in the global carbon cycle and Earth's climate. The ocean with 38,000 Gt of carbon is the largest rapidly exchanging carbon reservoir and due to its exchange of carbon with the atmosphere it has a major control on atmospheric CO_2 concentrations (Ciais et al., 2013; Sarmiento and Gruber, 2006). The surface ocean and atmosphere exchange CO_2 through gas exchange. This gas exchange is mainly driven by the difference in partial pressure of CO_2 between the atmosphere and surface ocean (Ciais et al., 2013). With humans emitting substantial quantities of carbon dioxide into the atmosphere, due to activities such as fossil fuel burning, production of cement and land-use changes, the partial pressure of CO_2 in the atmosphere is increasing. In response to increased atmospheric pCO_2 levels, the ocean uptakes CO_2 in order to equilibrate the sea-air interface. Thus, the global ocean also plays an important role in mitigating global warming. Each year, the ocean takes up about a quarter of anthropogenic carbon dioxide emissions (Sabine et al., 2004; Gruber et al., 2009; Friedlingstein et al., 2022). Furthermore, the ocean comprises the only true net sink (195 ± 35 GtC since 1790) for anthropogenic CO_2 over the past 200 years - for a carbon balance defined as the difference between the fossil-fuel emissions and the combination of the ocean inventory and atmospheric inventory change (Sabine et al., 2004). Without the ocean, atmospheric CO_2 levels would be more than 80ppm higher than they are today (based on the 419ppm 2022 annual average) (Jiang et al., 2023). Model simulations project an increase in the strength of the oceanic sink over the next few decades under increasing CO_2 emissions, but the spatial distribution of the oceanic sink strength is still uncertain (Lee et al., 2021).

While the global ocean is a net sink for anthropogenic CO_2, it is not evenly distribution throughout the ocean. For example, high anthropogenic CO_2 concentrations are found in the North Atlantic where upwelling in the subpolar gyre exposes deeper waters to the atmosphere, permitting them to take up anthropogenic CO_2; and deep water forming in the Labrador and Greenland Seas transports the anthropogenic carbon into the deep ocean (DeVris, 2022). As anthropogenic CO_2 invades the ocean via gas exchange at the sea-air interface, it reacts with seawater forming carbonic acid (H_2CO_3), which then dissociates into bicarbonate (HCO_3-) and carbonate ($CO_3{}^{2-}$) ions. The sum of these makes up dissolved inorganic carbon (DIC) in the ocean. DIC along with wind speed, sea surface temperature (SST), salinity (SSS), alkalinity (ALK, a measure of excess of bases over acids), and atmospheric partial pressure of CO_2 (pCO_2) determine the magnitude and sign of the sea-air CO_2 exchange. These variables themselves are governed by physical ocean conditions, ocean circulation patterns, air-sea interactions and biology (Mignot et al., 2021). For example, the ocean's ability to absorb carbon is partly dependent on temperature. As temperature increases, the solubility of CO_2 in the ocean water decreases, which increases oceanic pCO_2 and drives carbon into the atmosphere (Williams and Follows, 2011). Additionally, in the North Atlantic where deep water formation occurs and transports carbon to the deeper ocean, the surface ocean in this region is able to take up more CO_2 contributing to a flux of CO_2 into the ocean. Regional patterns in the sign of the sea-air exchange emerge: oceanic outgassing of CO_2 occurs in tropical regions and oceanic uptake of CO_2 occurs in mid-high and northern high latitudes (Gruber et al., 2009; Williams and Follows, 2011).

The increase in oceanic uptake of anthropogenic CO_2 is not the only change occurring in the oceans.

In the past century, marine heatwaves (MHWs) or prolonged periods of anomalously warm sea surface temperatures have globally increased in frequency, intensity, and duration on average (Oliver et al., 2018; Holbrook et al., 2019). For example, the number of MHW days has doubled between the beginning of the satellite period in 1982 and 2016. Projections show on average, an increase in this number by a factor of 16 for global warming of 1.5 degrees Celsius relative to pre-industrial levels, and by a factor of 23 for global warming of 2.0 degrees Celsius (Frölicher et al., 2018). Over the last few decades, MHWs were identified in all ocean basins. For instance, prominent and impactful MHW events occurred in the northern Mediterranean Sea in 2003, along the Western Australian coast in 2011, the northwest Atlantic in 2012, the northeast Pacific over 2013–2015, off southeastern Australia in 2015/16 and across northern Australia in 2016. The increase in the likelihood of recent MHWs is mainly due to the mean trend in sea surface temperatures as a result of anthropogenic climate change (Oliver et al., 2019; Laufkötter et al., 2020; Frölicher et al., 2018). For instance, as of 2018, 87% of MHWs were attributed to anthropogenic warming (Frölicher et al., 2018). Individual MHWs however can arise due to a combination of local oceanic and atmospheric processes including sea-air heat flux, horizontal temperature advection, horizontal and vertical mixing, and entrainment of water. Sea-air heat flux and horizontal temperature anomalies are the main contributors to MHW events; the horizontal and vertical mixing and entrainment terms contribute less to the temperature changes associated with MHWs (Oliver et al., 2021). A MHW event due to horizontal temperature advection can occur when the background state is perturbed by an anomalous flow creating high SST anomalies. For example, a poleward geostrophic flow in a western boundary current region perturbed by an anomalous Ekman flow associated with wind stress to the northeast, can cause anomalously high SSTs (Figure 1) (Oliver et al., 2021). A MHW event driven by air-sea heat flux anomalies is a result of changes in the net air-sea heat flux. This net flux is the sum of the net shortwave and longwave radiation, and latent and sensible turbulent heat fluxes. An air-sea heat flux MHW event can arise due higher net shortwave radiation and or sensible turbulent heat fluxes due to lower cloud cover and greater insolation (Oliver et al., 2021; Gupta et al., 2020). These cases are often accompanied by an atmospheric high-pressure system and reduced wind speeds, which weaken vertical mixing and reduce the mixed layer depth (Figure 1) (Gupta et al., 2020). Moreover, reduced wind speeds can cause anomalously lower latent heat loss from the ocean further contributing to sea surface temperature increases (Oliver et al., 2021). MHWs can also be modified by large-scale climate variability including remote sources via teleconnections (Oliver et al., 2021). This can be through oceanic Kelvin waves, Rossby waves, atmospheric blocking, intraseasonal modes (such as Madden-Julian Oscillation), interannual modes (such as El Niño Southern Oscillation and Indian Ocean Dipole), and decadal modes (Interdecadal Pacific Oscillation, Atlantic Multi-decadal Oscillation) or a combination of these (Holbrook et al., 2019).

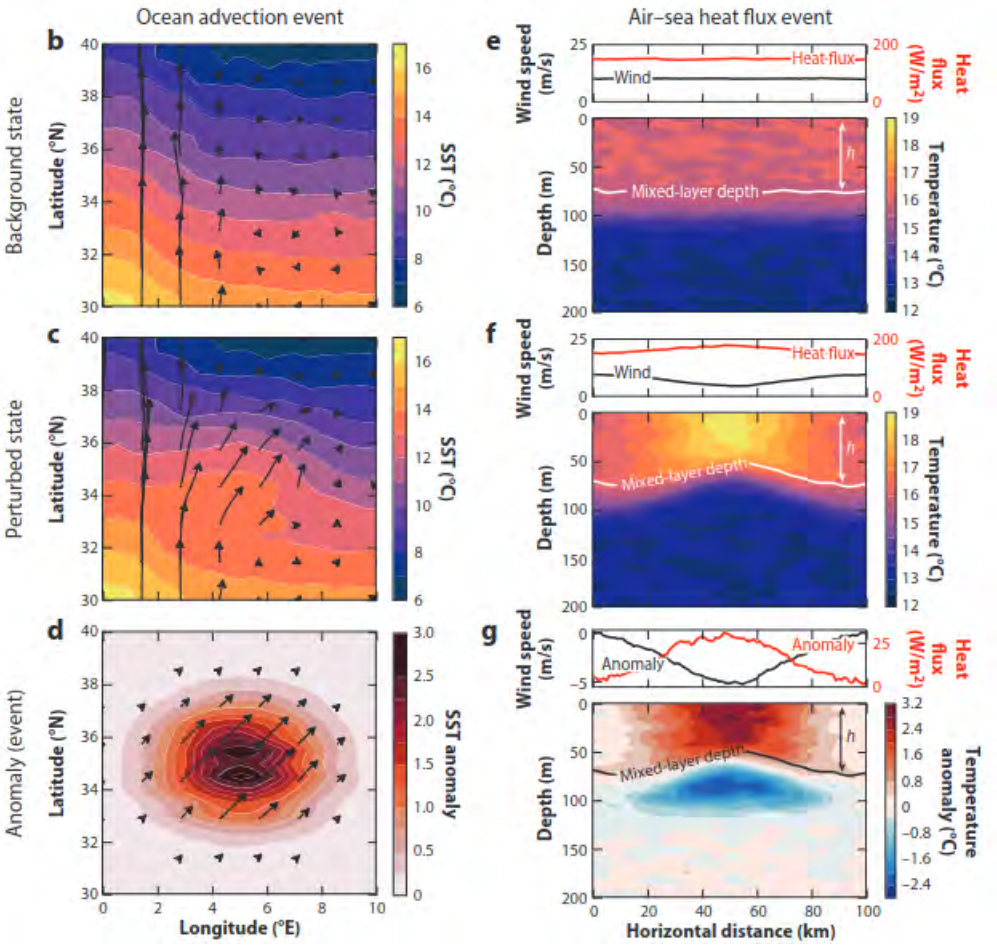

Figure 1: Idealized example of a MHW event caused by horizontal temperature advection (b-d), and a MHW event caused by air-sea heat flux anomaly (e-g). Figure from: Oliver et al. (2021).

The threats associated with MHWs can be severe. MHWs can cause devastating impacts on marine ecosystems and socio-economic systems (Collins et al., 2019). Observed impacts of MHWs include range shifts of marine species, toxic algal blooms, mass coral bleaching events, loss of biodiversity and ecologically important foundation species, and mortalities of important commercial fish species (Cheung and Frölicher, 2020; Hughes et al., 2017; Smale et al., 2019; Cheung et al., 2021; Frölicher and Laufkötter, 2018). In addition, Mignot et al. (2021) found that persistent MHWs cause a reduction in oceanic CO_2 release in the tropics linked to ENSO and a reduction in oceanic CO_2 uptake in the North Pacific. While Mignot et al. (2021) provides a strong foundation to investigate the interplay and impacts of MHWs on sea-air CO_2 fluxes, there are at least two aspects to build on. Firstly, they only consider 'persistent' MHWs, which they define as MHWs whose duration and mean sea surface temperature anomaly exceed the 95th percentile of their global historical distribution. This equates to a MHW duration greater than 38 days and mean sea surface temperature anomaly of 2.3 degrees Celsius (Mignot et al., 2021). Furthermore, they consider only points where persistent MHWs have reoccurred at least 3 times during the period 1985-2017. Applying such an extreme criteria leads to the exclusion of a large number of MHWs. For example, Vogt et al. (2022) applies a 90th percentile to identify sea surface temperature extremes for a similar time period (1981-2020) and found the global mean duration of MHWs to be 4.6 days with observation-based sea surface temperature data and 15 days with model sea surface temperature data.

Secondly, Mignot et al. (2021) focuses mostly on the Pacific Ocean where the strongest change in sea-air CO_2 flux during MHWs occurs. Mignot et al. (2021) describes the impact of MHWs on sea-air CO_2 fluxes as a result of two competing mechanisms: (1) increased sea surface temperatures reducing the solubility of CO_2, increasing oceanic pCO_2, and reducing oceanic CO_2 uptake and, (2) increased density stratification reducing vertical mixing and entrainment, decreasing surface dissolved inorganic carbon, and increasing oceanic CO_2 uptake. These competing mechanisms can be referred to as the thermal effect (1) and DIC advection effect (2). Mignot et al. 2021 concludes the temperature effect (1) outweighs the advection effect (2) in the north Pacific. Another recent case study by Duke et al. (2023) on estimating marine carbon uptake considers MHW impacts on the northeast Pacific ocean CO_2 sink. Duke et al. (2023) finds rather MHWs allow for enhanced atmospheric CO_2 uptake. In contrast to Mignot et al. (2021), Duke et al. (2023) attributes the flux anomalies in the northeast Pacific to the reduced winter mixing which is a result of weaker winds and increased density stratification, enhancing atmospheric CO_2 uptake (the advection effect dominates). The differences are potentially due to the study area, as Mignot et al. (2021) considers the North Pacific subtropical gyre and Duke et al. (2023) looks at the North Pacific subpolar gyre. Nevertheless the varying results underline the need for more studies focusing on the interplay of MHW events and sea-air CO_2 fluxes to understand how carbon sinks and sources react to climate change and eventually help humans plan their carbon reduction commitments.

This thesis involves a global approach to investigate the impacts of MHWs on the sea-air CO_2 fluxes and the drivers behind these CO_2 flux anomalies using both observation-based and model-based data. A comprehensive global approach to the impact of MHWs on sea-air CO_2 fluxes has not been done yet and is particularly important because oceanic regions vary greatly in terms of the magnitude and direction of the mean sea-air flux due to unique physical characteristics, ocean circulation patterns, biological net production and sea-air interactions. This thesis has three aspects. The first objective is to globally assess if and how MHWs impact sea-air CO_2 fluxes using observation-based data. The second objective is a replication of objective 1 but for the GFDL ESM2M model data. The third objective is to assess the drivers of the CO_2 flux anomalies during MHWs for both the observation and model-based data, by decomposing the sea-air CO_2 flux into it's individual contributions, and finally further decomposing the dominating contribution. The parallel approach of using observation-based and model data for each objective not only allows for an evaluation of the accuracy of the model data but can aid future downstream analyses furthering the investigation of the driving mechanisms behind changes in the sea-air CO_2 flux during MHWs.

3 Data & Methods

In this section, the observation-based data and the Earth System Model (ESM) data used to assess sea-air CO_2 fluxes during marine heatwaves and their drivers are described. Additionally, the analytical tools to derive the results are introduced.

3.1 Observation-based data

The global observational-based SST data used in this research to identify marine heatwaves is sourced from the National Oceanic and Atmospheric Administration (NOAA) Daily Optimum Interpolation Sea

Surface Temperature (OISST) dataset v2.1 (Huang et al., 2021). It is a long-term climate data record from 1 September 1981 to present day, available in daily mean time steps with a resolution of 0.25°x0.25°. The product incorporates in situ ship and buoy sea surface temperature observations with satellite sea surface temperatures derived from the Advanced Very High-Resolution Radiometer to provide a daily global record of surface ocean temperature observations on a regular global grid. The dataset is interpolated to fill any gaps and provide a spatially and temporally complete map of sea surface temperature. In this thesis, the daily mean SST data is regridded to 1°x1° and averaged to monthly timesteps for the period 1982-2021 to match the spatial and time resolution of the pCO_2 data.

For the observation-based sea-air CO_2 flux data, the SeaFlux version 2021.04 data product with 1°x1° grid is used (Fay et al. 2021). SeaFlux is an ensemble data product that utilizes six global observation-based pCO_2 products and five global wind reanalyses to generate sea-air CO_2 fluxes in monthly time steps for the time period 1990-2019. The six observation-based pCO_2 products used in SeaFlux consist of three neural network-derived products (CMEMS-FFNN, MPI-SOMFFN, NIES-FNN), one mixed layer scheme product (JENA-MLS), one multiple linear regression product (JMA-MLR), and one machine learning ensemble product (CSIR-ML6) which is an ensemble average of six machine-learning models. As seen in table 1, the six observation-based pCO_2 products use different versions of the raw pCO_2 data available from the Surface Ocean Carbon Dioxide Atlas (SOCAT) (Bakker et al., 2016). SOCAT is an activity of the international marine carbon research community, with the aim to provide public access to gridded monthly mean surface water fugacity of carbon dioxide on a 1°x1° grid with minimal temporal or spatial interpolation (Bakker et al., 2016). SOCAT data are released in versions, with each succeeding version containing new data sets as well as updates of older ones. More information on SOCAT can be found at the webpage: https://socat.info/. The five wind reanalysis products in SeaFlux are CCMPv2, ERA5, JRA55, NCEP2, NCEP1, which were created by extrapolating historical wind speed observations through modeling and data assimilation systems (Fay et al., 2021). In this research, the SeaFlux dataset (with the six different pCO_2 products and five different wind products) makes up an observation-based ensemble of 30 members. Refer to Table 1 and 2 for a complete summary of the differences between the pCO_2 and wind products.

The common approach to estimate the net flux of CO_2 across the sea-air interface is through the use of surface ocean CO_2 observations and a bulk parameterization approach. SeaFlux applies the standard bulk parameterization approach to estimate the net sea-air CO_2 flux ($F_{sea-air}$). This approach is based on the bulk formula (Wanninkhof, 1992):

$$F_{sea-air} = k_w \cdot \rho \cdot sol \cdot (pCO_2 - pCO_{2atm}) \cdot (1 - ice) \tag{1}$$

where k_w is the gas transfer velocity (in units m s^{-1}), ρ is a constant (1035 kg m^{-3}) representing the density of surface seawater, and it is only included depending on the units of solubility), sol is the solubility of CO_2 in seawater (in units of mol $kg^{-1}\mu atm^{-1}$ with ρ; or $mol^{-3}\mu atm^{-1}$ without ρ), pCO_2 is the partial pressure of surface ocean CO_2 (in units of μatm), and pCO_{2atm} represents the partial pressure of atmospheric CO_2 in the marine boundary layer (in units of μatm). The ice fraction is included to take into account the seasonal ice cover in high latitudes. Sea ice can act as a lid inhibiting sea-air carbon exchange (Gupta et al., 2020). Thus, the fluxes are then weighted by 1 minus the ice fraction, i.e. the open ocean fraction (Fay et al., 2021). The gas transfer velocity is calculated using the quadratic wind

speed dependence (Wanninkhof, 1992):

$$k_w = a \cdot U^2 \cdot (Sc/660)^{-0.5} \tag{2}$$

where the units of k_w are in m s^{-1}, Sc is the dimensionless Schmidt number, and U denotes the average monthly wind speed for 10m high winds (m s^{-1}) and a is the scaling of the coefficient of gas transfer in units (m s^{-1})^2. In the SeaFlux dataset, the coefficient, a, is not consistent for each wind product and is individually calculated based on Naegler (2009). Morever, the Schmidt number for CO_2 is defined as:

$$Sc = A - B \cdot T^2 + CT^2 - DT^3 \tag{3}$$

where A, B, C, and D are constants which differ between the observation-based and model calculations. For the observation-based, the coefficients for CO_2 are taken from Jähne et al. (1987). For the ESM2M data, A = 2068.9, B=118.63, C=2.9311, and D=0.027. T is temperature (in °C).

SeaFlux applies this uniform methodology for CO_2 flux calculations on the different pCO_2 and wind products. However, before this flux calculation is done two important steps occur: area filling for missing pCO_2 product data and calculation of the gas exchange coefficient a. The largest contributors to the methodological discrepancies can be attributed to these steps (Fay et al., 2021). For example, the pCO_2 area adjustment results in an increase in CO_2 uptake of 0-17% relative to the original (depending on the product) (Fay et al., 2021). The first step of pCO_2 area filling is necessary because the six pCO_2 products have variable spatial coverage (as seen in Table 1). There is variable spatial coverage because pCO_2 products are limited by the areal extent of proxy variables which help extrapolate in situ observations (Supplementary Figure 1). Some of the mapped pCO_2 products miss coastal and high latitude regions. To address this, SeaFlux applies Landschützer et al. (2020b)'s open and coastal merged climatology product which includes coverage in the coastal and Arctic regions to fill any missing grid cell with a scaled value based on this global-coverage climatology. This allows for consistent and complete global ocean coverage of the flux for each pCO_2 product despite missing areas in the original pCO_2 product. The second step pertains to the scaling of the gas transfer coefficient (a). The ideal coefficient depends on the wind speed product. SeaFlux scales the gas transfer coefficient for each product with Naegler (2009)'s equation for a, in which it chooses to scales k_w to a single global value of 16.5 cm h^{-1} for all wind products. Fay et al. (2021) states scaling k_w to a single global value for all wind products reduces the spread of flux estimates. Without scaling (a) for each product, and just applying a set value for the gas transfer coefficient, calculated global fluxes could be as high as 9% different depending on the pCO_2 and wind reanalysis product considered (Fay et al., 2021). By determining the optimal a coefficient for each of the reanalysis winds, uncertainty in the global fluxes is decreased. Results are presented in terms of the ensemble member average, but analyses were done for each ensemble member (i.e. each combination of one pCO_2 and one wind product). Additionally, we compare the sea-air flux anomalies between the individual pCO_2 products, and between the individual wind products.

Table 1: Summary of the six observation-based pCO_2 products used in SeaFlux to calculate the sea-air CO_2 flux.

pCO_2 mapping product	Area coverage (% global ocean)	Surface-ocean pCO_2 data	Reference
CMEMS-FFNN	89%	SOCAT v5	Denvil-Sommer et al. (2019), Chau et al. (2022)
CSIR-ML6	93%	SOCAT v5	Gregor et al. (2019)
JENA-MLS	100%	SOCAT v1.5	Rödenbeck et al. (2013)
JMA-MLR	85%	SOCAT v5	Iida et al. (2020)
MPI-SOMFFN	89%	SOCAT v5	Landschützer et al. (2014), Landschützer et al. (2020a)
NIES-FNN	91%	SOCAT v2	Zeng et al. (2014)

Table 2: Summary of five observation-based wind products used in combination with the observational pCO_2 products in SeaFlux. The date range starts for the first full year of data. Mean wind speed is given for the ice-free ocean for the three decade period 1990-2019.

Wind product name	Temporal Resolution (hr)	Spatial Resolution (°)	Date range	Mean speed (m s^{-1})	Scaled coefficient of gas transfer (a) $(m/s)^2$	Reference
Cross-Calibrated Multi-Platform v2	6	0.25	1988-present	7.7	0.257	Atlas R. et al. (2009)
ECMWF Reanalysis 5th Generation	1	0.25	1979-present	7.5	0.271	Hersbach et al. (2020)
Japanese 55-year Reanalysis	3	0.50	1958-present	7.6	0.260	Kobayashi et al. (2015)
NCEP-NCAR reanalysis 1	6	2.50	1948-present	7.2	0.287	Kalnay et al. (1996)
NCEP-NCAR reanalysis 2	6	2.50	1979-present	8.3	0.218	Kanamitsu et al. (2002)

3.2 ESM2M model data

The Earth System Model (ESM) data used in this thesis is from the global coupled carbon-climate Earth System Model, ESM2M developed at the Geophysical Fluid Dynamics Laboratory (GFDL) of the National Oceanic and Atmospheric Administration (NOAA) (Dunne et al., 2012, 2013). ESMs represent

major carbon reservoirs and fluxes based on atmosphere, ocean, land, and sea ice dynamics and include chemistry and ecological dynamics as well. ESM2M consists of an ocean model MOM4p1 (Griffies, 2009) which includes an ocean biogeochemistry model TOPAZ2 (Dunne et al., 2013), an atmospheric model AM2 (Anderson et al., 2004), a land model LM3.0 (Shevliakova et al., 2009), a sea ice model (Winton, 2000), and iceberg dynamics (Martin and Adcroft, 2010). A coupler allows the modules to pass fluxes across their interfaces, and ensures energy, mass and tracer conservation (Dunne et al., 2013). The ocean component runs with a two hour time step. Likewise, the fluxes between the ocean and atmosphere are exchanged on a two hour timestep. Thus, the sea-air flux data is calculated in 2 hourly timesteps. For this thesis, the original flux data was averaged into monthly timesteps to align with the observation-based data.

For the purpose of this research, the MOM4p1 and TOPAZv2 are briefly described. The MOM4p1 has a 1° horizontal grid up to 1/3° meridionally at the equator and tripolar grid above 65°N (two poles in the Northern Hemisphere and one in the Southern Hemisphere) with 50 vertical levels. The ocean biogeochemical and ecological component TOPAZ, includes 30 tracers to describe the cycles of carbon, nitrogen, phosphorous, silicon, iron, oxygen, alkalinity, lithogenic material, and lastly surface sediment calcite (Dunne et al., 2012). It includes processes such as gas exchange, atmospheric deposition, scavenging, N_2 fixation and denitrification, river inputs, and sediment processes to represent the interaction of biologically active elements and ecological cycling with the carbon cycle (Dunne et al., 2010). The carbonate chemistry and sea-air CO_2 exchange are based on the Ocean Carbon-Cycle Model Intercomparison Project (OCMIP2) recommendations of Najjar and Orr (1998). The carbonic acid and bicarbonate dissociation constants are based on Mehrbach et al. (1973), the solubility of CO_2 is consistent with Weiss (1974), and finally, the gas transfer velocity is calculated from the wind speed and Schmidt number based on Wanninkhof (1992).

ESM2M has been proven to successfully simulate sea surface temperature variability, and has been used in previous studies to analyze MHWs (Frölicher et al., 2018; Vogt et al., 2022; Bopp et al., 2013; Le Grix et al., 2022) as well as MHW events in terms of their impacts on carbonate chemistry related variables (Burger and Frölicher, 2023). For this thesis we use a model ensemble of 30 members each with differing initial conditions.

3.3 Marine heatwave definition

There are various options to quantitatively define a marine heatwave (Oliver et al., 2021). MHWs are often defined as periods in time where sea surface temperature exceeds a certain absolute or relative threshold, with definitions differing mainly in the choice of threshold. This thesis applies a seasonally varying threshold. A seasonally varying threshold allows extremes to occur at equal likelihood throughout the year regardless of the season (Hobday et al., 2016). A unique threshold is defined for each month which varies according to the seasonal cycle and seasonal variability. For the seasonally varying threshold a percentile for the threshold must be selected. The 90th percentile is selected, consistent with other extreme analyses (Hobday et al., 2016; LeGrix et al., 2021), as it is high enough to indicate extremes but also low enough to provide a sufficient sample of MHW months for statistical analyses. Detrended sea surface temperature data from January 1982 - December 2021 is used to identify the seasonally varying percentile. For every grid cell, a MHW is identified if the sea surface temperature anomaly for a month

is greater than 90 percent of anomalies for the same month in all years at that grid cell. This results in a marine heatwave mask of three dimensions (time, latitude, longitude). It can also be noted that the marine heatwave identification is unique for each model ensemble member, as in the seasonally varying threshold is recalculated for each model ensemble member. However, the ensemble variation is minimal in this regard.

3.4 Marine heatwave metrics

To assess the skill of the ESM2M model in simulating MHW events, three MHW metrics are compared between the model-based data and NOAA OISST v2.1 dataset. MHW magnitude, intensity, and duration on a monthly timescale between 1982-2021 are considered. MHW intensity is calculated as the maximum difference between the SST data and the seasonally varying threshold; MHW magnitude is calculated as the maximum difference between the SST data and the seasonal climatological cycle; and MHW duration quantifies the length in consecutive months when the data exceeds the seasonally varying threshold (Frölicher et al., 2018; Oliver et al., 2021; Holbrook et al., 2019). For observation-based and model comparisons, the calculated observation-based MHW metrics are regridded onto the model tripolar grid.

Figure 2 shows the model-observation comparison for all three metrics. Overall, the model simulates similar spatial patterns of the three metrics. The model and observation spatial patterns of maximum MHW intensity agree well. Global mean intensity is at 1.0 K in the NOAA dataset and 1.1 K in the model. The equatorial Pacific and western boundary currents emerge as regions with the highest maximum intensity (Figure 2d, 2e). For the equatorial Pacific this is most likely a result of El Niño events. For the western boundary currents, it is likely a result of the intense atmosphere-ocean interactions, strong currents, and sharp horizontal temperature gradients in these regions. The model shows slightly more intense heatwaves in these regions compared to the observations, as well as more intense heatwaves in the Southern Ocean and northern high latitudes. The high latitude and Southern Ocean deviations could be a result of limited or poor observation-based data.

Larger differences between the observation and model data occur for the maximum magnitude and duration metrics (Figure 2c, 2i). Although the spatial patterns of MHW magnitude agree well between the model and observations, the model predicts greater magnitudes than the observation data. The global maximum magnitude is 1.9 K in the NOAA dataset and 2.1 K in the model. The model overestimates the maximum magnitude mainly in the equatorial Pacific, Southern Ocean, northwest Pacific. On the other hand the model predicts a lower magnitude for the latitudinal strip around 45°S and off the west coast of the United States. In terms of mean duration, the model clearly overestimates the mean duration compared to observations (Figure 2i). The global average duration of MHWs is 1.867 months in the NOAA dataset and 2.377 months in the model. MHWs are longer at almost all locations globally in the model, and longest in the equatorial pacific region, where it is directly impacted by El Niño events. The model shows a larger area in the equatorial Pacific with the longest events, where the MHW duration is 4 months or longer. This is consistent with the overly strong simulated ENSO variability in ESM2M model (Dunne et al., 2012).

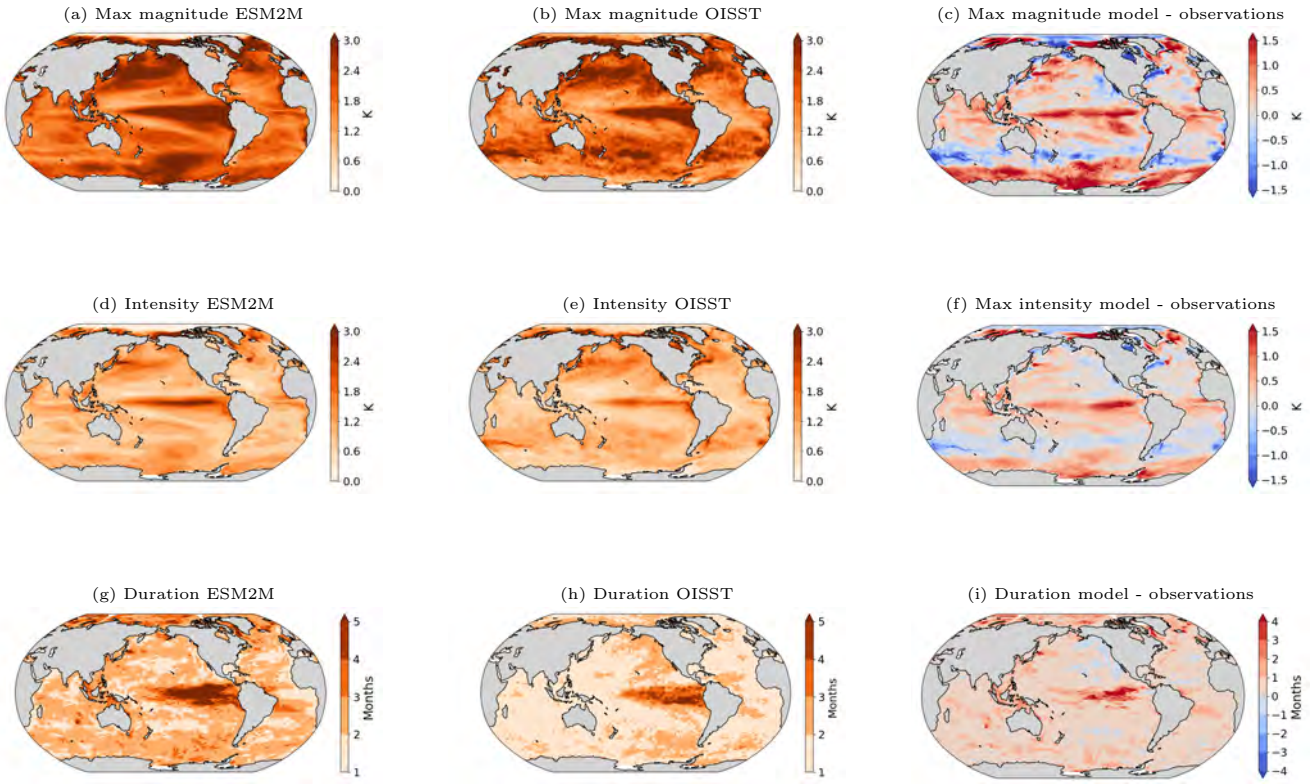

Figure 2: Global comparison between model and observation-based marine heatwave metrics: magnitude (top row), max intensity (middle row), and duration (bottom row). The difference between the model and observational values are presented in the far right column. Intensity is calculated as the maximum magnitude, meaning the maximum exceedance of the SST data to the seasonally varying percentile threshold. Magnitude is calculated as the maximum exceedance of the SST data to the seasonal climatological cycle. Duration is calculated as the length of time in which the data exceeds the seasonally varying threshold in months. These metrics are from MHWs over the period January 1982 through December 2021.

Although these metrics are considered on the monthly timescale, monthly data is able to capture the spatial trends seen in these metrics with daily data. Similar patterns are observed between the global maps produced with monthly data presented above, and Vogt et al. (2022)'s global maps of the metrics produced with the same NOAA OISST v2.1 dataset at daily time steps.

3.5 Analysis Methods

3.5.1 Region definitions

A set of specific geographical regions is established in this thesis for more in depth analyses. Eight regions were selected in regard to the differing characteristics of ocean basins (e.g., strong or weak CO_2 sink or source regions) to highlight patterns and dynamics at play during MHWs with particular ocean basin characteristics. The regions are visualized in Figure 3, and the geographical coordinates can be found in Table 3. The data in all the grid cells of a rectangular box are averaged, weighted by their grid cell area.

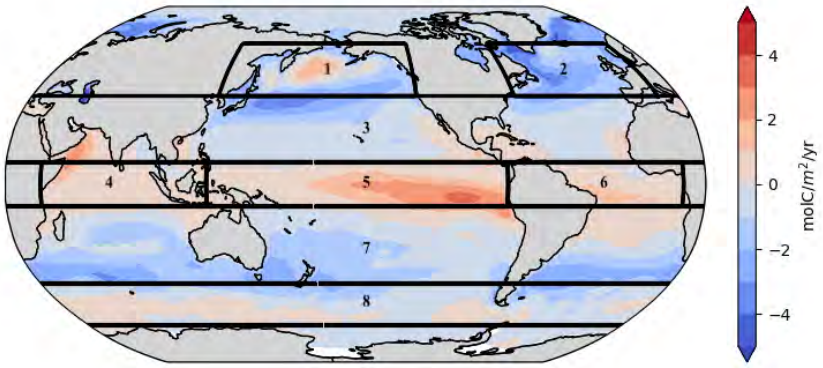

Figure 3: Definition of the eight study regions used for analysis. Each region is a rectangular box. The background coloring depicts the average sea-air CO_2 flux state from the 30 observation-based ensemble for the years 1990-2021, with blue indicating an ingassing of CO_2 into the ocean and red indicating an outgassing of CO_2 from the ocean.

Table 3: Definition of regional latitude–longitude boxes.

Region	Longitude range	Latitude range
Northern Pacific	140°E - 130°W	65°N - 40°N
Northern Atlantic	70°W - 10°E	65°N - 40°N
Low-Mid Latitude Northern Hemisphere	Full	10°N - 40°N
Equatorial Indian	40°E - 125°E	10°S - 10°N
Equatorial Pacific	125°E - 80°W	10°S - 10°N
Equatorial Atlantic	77°W - 10°E	10°S - 10°N
Low-Mid Latitude Southern Hemisphere	Full	10°S - 45°S
Southern Ocean	Full	65°S - 45°S

3.5.2 MHW sea-air CO_2 flux anomalies

The monthly sea-air CO_2 flux anomalies during MHWs are obtained for the period 1990-2019 by first removing a climatological value in the monthly mean flux data. The climatological values correspond to the sum of the long-term linear trends and seasonal monthly means. These flux anomalies are denoted as prime moving forward (eg. $F'_{sea-air}$). In order to find the flux anomalies during marine heatwaves, the three dimensional (time, latitude, longitude) marine heatwave mask is applied to this flux anomaly data to isolate data for only the time periods and grid cells that experienced MHWs, resulting in the sea-air CO_2 flux anomalies during MHWs. Flux anomalies during MHWs were calculated for each grid cell experiencing a heatwave and for each of the 8 study regions. The same MHW definition and process to calculate flux anomalies is applied to both observation-based and model data.

In order to determine if the sea-air CO_2 flux anomalies during MHWs present a significant change to the mean CO_2 flux, a two-mean statistical test for difference is conducted globally and for each region. This test is performed under the assumption that the two mean samples are independent and have identical variances. The null hypothesis is that the two samples have identical averages and the alternative hypothesis is that the averages are significantly unequal. The test statistic t is calculated as

the difference in means of sample 1 and 2, divided by the standard error. The test statistic outputs are used to determine the p-values. If the p-value is below the 0.05 level threshold for statistical significance (a 95% confidence interval), then the null hypothesis is rejected in favor of the alternative hypothesis.

3.5.3 Decomposition of sea-air flux anomalies

As a precursor to the Taylor decomposition of the flux anomalies during MHWs, monthly sea-air CO_2 fluxes are manually calculated using equation 1 and the five flux equation inputs. This step is done to ensure confidence in the individual flux input data before the Taylor decomposition is performed. Firstly, for the observation-based data, SeaFlux provides the flux input datasets: gas transfer velocity (k_w), solubility (sol), $pCO_{2_{\mathrm{oc}}}$, $pCO_{2_{\mathrm{atm}}}$, and sea ice fraction, all in monthly time steps. The gas transfer velocity (k_w) can be recalculated based on equation 2. The solubility can be recalculated according to Weiss (1974), where:

$$\begin{aligned} sol = &-60.2409 + 93.4517\left(\frac{100}{\mathrm{SST}}\right) + 23.3585\log\left(\frac{\mathrm{SST}}{100}\right) + \\ &\mathrm{SSS}\left(0.023517 - 0.023656\left(\frac{\mathrm{SST}}{100}\right) + 0.0047036\left(\frac{\mathrm{SST}}{100}\right)^2\right) \end{aligned} \tag{4}$$

The observation-based $p\mathrm{CO}_2$ atmosphere can be recalculated as the dry air mixing ratio of atmospheric CO_2 multiplied by sea level pressure at monthly resolution, and then corrected for water vapor according to Dickson et al. (2007). Using these individual datasets of solubility, gas transfer velocity, $pCO_{2_{\mathrm{oc}}}$, $pCO_{2_{\mathrm{atm}}}$, and sea ice, we recalculate the flux and refer to this as the observation-based 'manually recalculated' monthly flux.

In terms of the model data, the existing model data for sea surface temperature, salinity, wind speed (U), and oceanic $p\mathrm{CO}_2$ is used. The gas transfer velocity (k_w), solubility, and atmospheric $p\mathrm{CO}_2$ need to be calculated. The gas transfer can be calculated with equation 2, with the constant a equal to 0.337. Solubility can be calculated with equation 4 based on Weiss (1974). Finally, the model atmospheric $p\mathrm{CO}_2$ data is calculated according to Najjar and Orr (1998), where sea level pressure is first subtracted by the water vapor pressure at saturation and then multiplied by the dry air mixing ratio of atmospheric CO_2:

$$[A]_{\mathrm{sat}} = K_0 f_A = K_0 C_f p_A = K_0 C_f (P_a - p\mathrm{H_2O}) x_A \tag{5}$$

For a gas A, K_0 is its solubility, C_f is its fugacity coefficient, P_a is the total atmospheric pressure (atm), $\mathrm{pH_2O}$ is the water vapor pressure at saturation (atm), and x_A is its mole fraction in dry air (Orr et al., 2017).

After manually recalculating the fluxes for both the observation-based and model data, flux anomalies during MHWs for these recalculated data are determined using the same definition outlined in 3.3. These manually recalculated anomalies will be compared to the 'true' SeaFlux and model simulated flux anomalies and eventually to the sum of the flux decomposition terms. It must be noted that in this thesis, the model simulated data for the flux variables (sea surface temperature, salinity, wind speed, pCO_2 ocean) were only available in monthly time steps (the data with the original 2 hourly timestep was

not currently available but could be obtained for future analyses). As a result, the model 'recalculated flux' is in monthly timesteps whereas the 'true' ESM2M flux data is originally for 2 hourly timesteps and then averaged to monthly timesteps.

To determine the driving mechanisms causing the sea-air CO_2 flux anomalies during MHWs, a first-order Taylor series decomposition is performed in terms of the flux equation components. This allows to see how much sea surface temperature, oceanic pCO_2, atmospheric pCO_2, salinity, wind, and sea ice each contribute to the overall sea-air CO_2 flux anomaly during MHWs. The first order Taylor series decomposition for equation (1) is:

$$F'_{\text{sea-air}} \approx \frac{\partial F_{\text{sea-air}}}{\partial \text{sol}} \cdot \Delta_{\text{sol}} + \frac{\partial F_{\text{sea-air}}}{\partial \text{kw}} \cdot \Delta_{\text{kw}} + \frac{\partial F_{\text{sea-air}}}{\partial pCO2_{\text{oc}}} \cdot \Delta_{pCO2_{\text{oc}}} + \frac{\partial F_{\text{sea-air}}}{\partial pCO2_{\text{atm}}} \cdot \Delta_{pCO2_{\text{atm}}} + \frac{\partial F_{\text{sea-air}}}{\partial \text{ice}} \cdot \Delta_{\text{ice}} \tag{6a}$$

$$\frac{\partial F_{\text{sea-air}}}{\partial \text{sol}} = k_w \cdot \rho \cdot (pCO_2 - pCO_{2\text{atm}}) \cdot (1 - \text{ice}) \tag{6b}$$

$$\frac{\partial F_{\text{sea-air}}}{\partial \text{kw}} = \text{sol} \cdot \rho \cdot (pCO_2 - pCO_{2\text{atm}}) \cdot (1 - \text{ice}) \tag{6c}$$

$$\frac{\partial F_{\text{sea-air}}}{\partial pCO2_{\text{oc}}} = k_w \cdot \rho \cdot \text{sol} \cdot (1 - \text{ice}) \tag{6d}$$

$$\frac{\partial F_{\text{sea-air}}}{\partial pCO2_{\text{atm}}} = -k_w \cdot \rho \cdot \text{sol} \cdot (1 - \text{ice}) \tag{6e}$$

$$\frac{\partial F_{\text{sea-air}}}{\partial \text{ice}} = -k_w \cdot \rho \cdot \text{sol} \cdot (pCO_2 - pCO_{2\text{atm}}) \tag{6f}$$

The right hand side of equation (6a) represents the contributions of solubility, the gas transfer velocity, partial pressure of CO_2 for the ocean and atmosphere, and sea ice fraction. The delta values represent the anomalies of the variable during MHWs. As noted in section 3.1, the density of surface seawater (ρ) is a constant and only applied with the model data to satisfy the solubility unit. Thus, ρ does not constitute a term in the decomposition. The partial derivatives were calculated for each grid cell.

The decomposition was done for each of the 30 observation-based ensemble members, the six observation-based $p\text{CO}_2$ products (using the average of the 5 wind products), and for each model ensemble member. Results are presented in terms of the ensemble average (observation-based and model). The sum of the decomposition terms is then compared to true and recalculated anomalies for the SeaFlux and model data. If the sum of the decomposition terms is close to the true and recalculated observation-based/model data sea-air CO_2 flux anomalies, it suggests the decomposition results are meaningful and interpretable. A mismatch between the sum of the decomposition terms with the true and recalculated anomalies can be due to the non-linearity in the function that maps solubility, gas transfer velocity, oceanic and atmospheric $p\text{CO}_2$ and sea ice fraction to sea-air CO_2 flux.

3.5.4 Decomposition of pCO_2 anomalies

Contingent on successfully similar values for the sum of decomposition terms and flux anomalies, the dominating flux component can be decomposed to further comprehend the drivers behind flux anomalies during MHWs. The initial flux decomposition reveals oceanic pCO_2 as the dominating factor behind sea-air CO_2 flux anomalies and is decomposed as:

$$pCO_2' \approx \frac{\partial pCO_2}{\partial DIC} \cdot \Delta_{DIC} + \frac{\partial pCO_2}{\partial ALK} \cdot \Delta_{ALK} + \frac{\partial pCO_2}{\partial SST} \cdot \Delta_{SST} + \frac{\partial pCO_2}{\partial SSS} \cdot \Delta_{SSS} \tag{7}$$

where oceanic pCO_2 is a function of dissolved inorganic carbon, alkalinity, sea surface temperature, and salinity. Variations in these variables, and thus oceanic pCO_2, stem from a complex interplay of chemical, biological, and physical processes. Since the seawater carbonate system is well constrained, it is common to measure or simulate two passive variables (dissolved inorganic carbon and total alkalinity) and compute all other carbonate system variables such as corresponding pH, partial pressure of carbon dioxide, concentrations of aqueous CO_2, carbonate and bicarbonate ions, related Revelle factors, and saturation state of aragonite and calcite from associated thermodynamics (Orr and Epitalon, 2015). OCMIP first provided routines to compute surface pCO_2 and sea-air CO_2 fluxes from total alkalinity and DIC and were adapted to include the full suite of other carbonate system variables (Orr and Epitalon, 2015). These equilibrium computations can be made with software packages. In this thesis, we use the public 'mocsy 2.0' Fortran 95 routines to model the ocean carbonate system. The mocsy package is based on the OCMIP model code, and computes other carbonate system variables from two passive tracers (DIC and ALK) and requires only additional input for temperature, salinity, total dissolved inorganic phosphorus, total dissolved inorganic silicon as well as pressure or depth. Mocsy applies the recommendations of Dickson et al. (2007), including the formula for solubility of CO_2 in seawater according to Weiss (1974); Lueker et al. (2000) for the first and second dissociation constants of carbonic acid; measurements from Mehrbach et al. (1973) for the NBS scale to the total pH scale; Millero (1995) for equilibrium constants of boric acid, phosphoric acid, silicic acid and water (which mocsy converts from the seawater scale to the total scale); Dickson (1990) for the equilibrium constant for the dissociation of bisulfate on the free scale; Perez and Fraga (1987) for the equilibrium constant for hydrogen fluoride on the total scale; and Mucci (1983) for the $CaCO_3$ solubility products for aragonite and calcite. The equations for carbonate system thermodynamics require in situ temperature, concentrations in moles per kilogram and in situ pressure. Mocsy provides the partial derivatives of temperature, salinity, DIC, and ALK with respect to pCO_2 for each grid cell.

For both the observation-based and model calculations, total dissolved inorganic phosphorous and silicate were obtained from World Atlas 2018 (WOA18) in monthly climatologies on a 1° grid for the year 1958. The climatologies were concatenated to match the 1990-2019 time frame of the analysis. For the observation-based decomposition, the same satellite-based sea surface temperature from the NOAA OISST v2.1 used in the MHW identification and salinity from the EN4.2.2 dataset of the Met Office Hadley Centre observations were used to calculate total alkalinity using the locally interpolated alkalinity regression (LIARv2) regression algorithm (Carter et al., 2018). DIC is then calculated with the PyCO2SYS package using the estimated total alkalinity, pCO_2 from the six different pCO_2 data products, temperature and salinity data. This results in a six different DIC datasets, one for each pCO_2 product.

Pressure is assumed to be 5 decibel (db) and atmospheric pressure is assumed to be 1 atm. The ESM2M model data output for SST, SSS, DIC, and ALK in monthly time steps for the years 1990-2019 is used for the model pCO_2 decomposition.

The pCO_2 Taylor decomposition was again done for the 30 observation-based ensemble members, each of the six observation-based DIC data products (using the average wind product), and the 30 model ensemble members. As done for the flux decomposition, the sum of the pCO_2 decomposition terms is compared to pCO_2 anomalies found with the SeaFlux data and model data. If the sum of the pCO_2 decomposition terms is close to the SeaFlux and model pCO_2 flux anomalies, it suggests the decomposition results are meaningful and interpretable.

4 Results

4.1 MHWs and Sea-air pCO_2 Fluxes

In this section, the impact of MHWs on sea-air CO_2 fluxes from observation-based and model-based data are presented at global and regional scales. Variations in the sea-air CO_2 flux anomalies between observation-based products and across individual simulated ensemble members are also analyzed.

4.1.1 Global

The observation-based and model-based data estimate on average a net global uptake of CO_2 of -0.481 (-0.574 to -0.418) mol C/m^2/yr (observation-based) and -0.537 (-0.544 to -0.529) mol C/m^2/yr (model). Globally, an opposite pattern between the mean CO_2 flux state and CO_2 flux anomalies during marine heatwaves emerges (Figure 4). For example, most regions with a mean state of oceanic CO_2 ingassing (indicated as blue in Figure 4a and Figure 4b) are mainly associated with anomalous CO_2 outgassing during MHWs (indicated as red in Figure 4g and Figure 4h). Regardless of the direction of the CO_2 flux, the flux is most often reduced during MHWs. As a result, the ocean's global net ingassing of CO_2 is weaker by 0.021 (-0.023 to 0.070) mol C/m^2/yr in the observation-based and 0.117 (0.101 to 0.137) mol C/m^2/y in the model data during MHWs.

In comparing the observation-based and model results, we find the model estimates the global mean flux within the observation-based ensemble spread. However the model seems to overestimate the magnitude of the global flux anomaly during MHWs beyond the observation-based ensemble spread. A two mean statistical tests find these globally averaged flux anomalies do not present a significant change compared to the mean state. This is possibly due to the counterbalancing direction of the fluxes and their resulting anomalies globally. Therefore, we investigate the regional anomalies that comprise this global result.

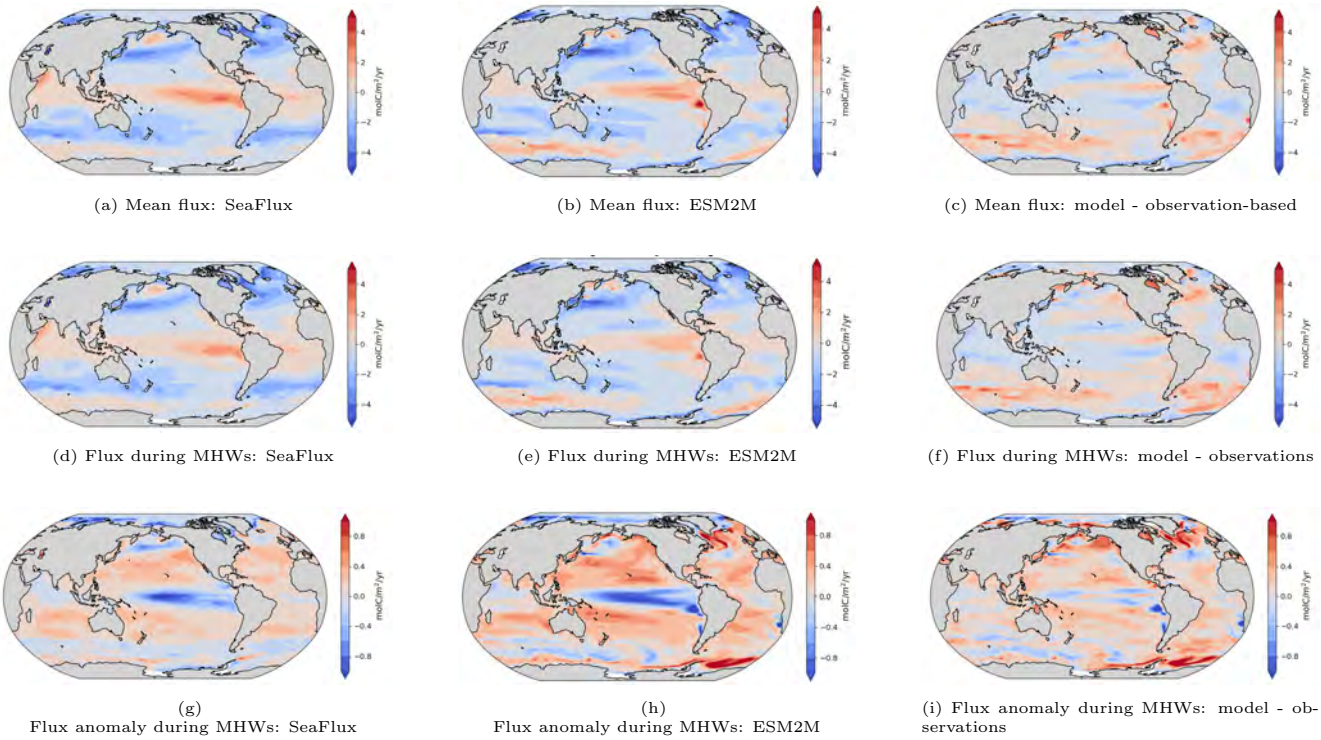

(a) Mean flux: SeaFlux (b) Mean flux: ESM2M (c) Mean flux: model - observation-based

(d) Flux during MHWs: SeaFlux (e) Flux during MHWs: ESM2M (f) Flux during MHWs: model - observations

(g) Flux anomaly during MHWs: SeaFlux (h) Flux anomaly during MHWs: ESM2M (i) Flux anomaly during MHWs: model - observations

Figure 4: Global comparison between model and observation-based ensemble averages for the mean sea-air CO_2 flux (top row), sea-air CO_2 flux during MHWs (middle row), and sea-air CO_2 flux anomalies during MHWs (bottom row) for the years 1990-2019. The difference between the model and observational values are the visualized in the third column. Observation-based data ensemble average is the average of the 6 pCO_2 and 5 wind products. Model based ensemble is average of the 30 GFDL ESM2M model ensemble members concatenated from historical simulations 1990-2005 and RCP8.5 forced simulations for 2006-2019. Negative values indicate oceanic uptake (blue), while positive values indicate oceanic outgassing (red) of CO_2.

For the observation-based data, three of the eight study regions experience significantly weaker sea-air CO_2 fluxes during MHWs compared to the mean flux state (Low-Mid latitudes regions in both hemispheres, and the Equatorial Pacific). Of the remaining five study regions, one experiences a significantly stronger sea-air flux during MHWs (Southern Ocean), and four experience insignificant changes to the sea-air flux during MHWs (Northern Atlantic, Northern Pacific, Equatorial Atlantic, Equatorial Indian). Results will focus on the regions with significant anomalies but all regions and their mean fluxes are depicted in Figure 5.

4.1.2 Equatorial pacific

The equatorial Pacific is one of the strongest oceanic CO_2 source regions. During MHWs, the region experiences a significant reduction to the mean oceanic CO_2 outgassing. It exhibits the largest absolute CO_2 flux anomaly -0.287 (-0.455 to -0.028) mol C/m^2/yr (observation-based) and -0.481 (-0.638 to -0.305) mol C/m^2/yr (model). This is equivalent to about a -31% (-3% to -49%) (observation-based) and -39% (26% to 50%) (model) reduction in the region's net outgassing of CO_2. In terms of observation-based and model comparisons, the model seems to overestimate the region's mean flux as it does not fall within the observation-based spread. However, the model predicted flux anomaly does fall within the observation-based anomaly spread.

4.1.3 Low-mid latitude regions

The low-mid latitude regions of the Northern and Southern Hemisphere (NH, SH), also experience weaker sea-air CO_2 fluxes. However, on average they act as net sinks, absorbing CO_2. Thus, the NH low-mid latitudes experience an anomalous outgassing of about 0.154 (0.104 to 0.201) mol C/m^2/yr (observation-based) and 0.267 (0.245 to 0.290) mol C/m^2/yr (model) (Figure 5). For the SH low-mid latitudes, flux anomalies are 0.118 (0.039 to 0.173) mol C/m^2/yr (observations) and 0.194 (0.172 to 0.225) mol C/m^2/yr (model). The flux anomaly in the NH low-mid latitudes equates to about a -30% (-20% to -39%) (observation-based) and -42% (-38% to -46%) (model) reduction in the ingassing flux relative to its mean flux; while for the SH low-mid latitude region the anomaly equates to a -14% (-5% to -21%) (observation-based) and -27% (-24% to -31%) (model) reduction to the mean ingassing flux. The low-mid latitude along with the equatorial Pacific represent the regions with the greatest flux anomalies during MHWs. The larger flux anomalies for the low-mid latitude regions and equatorial Pacific, suggests that regions with larger mean CO_2 fluxes are often areas associated with stronger CO_2 flux anomalies during MHWs (Figure 5). When integrating the mean flux and anomalies over the area of the region, the low-mid latitude regions result with the two largest mean CO_2 flux states and strongest CO_2 flux anomalies during MHWs (Figure 6). This is most likely a result of the large areal extent of the low-mid latitude study regions.

4.1.4 Southern Ocean

The Southern Ocean is a unique region due to its variable sea-air flux. It it encompasses both ingassing and outgassing regions of CO_2 and contrasting CO_2 flux anomalies (Figure 4g, 4h). In this thesis, the Southern Ocean region is identified with a mean net state of CO_2 ingassing for the observation-based data -0.462 (-0.635 to -0.310) mol C/m^2/yr, and for the model data -0.010 (-0.072 to 0.024) mol C/m^2/yr but to a lesser degree. The Southern Ocean is the sole study region where the sign of the flux anomaly diverges between observation-based and model results. For the observation-based data, the ingassing flux is enhanced by -0.057 (-0.162 to 0.038) molC/m^2/yr during MHWs. This counters the general pattern that sea-air CO_2 fluxes are reduced during MHWs. The model however, shows a transition of the mean ingassing flux into an outgassing flux 0.117 (0.069 to 0.167) C/m^2/yr. This model result is due to a combination of a weak mean ingassing flux and strong anomalous outgassing during MHWs. Additionally, the model flux anomaly during MHWs for the Southern Ocean is larger than the model's mean flux for the region. Low data availability in the region can be one reason behind the different sign anomalies found between the observation-based and simulated data. Additionally, in general models do not simulate well the Southern Ocean (Frölicher et al., 2015).

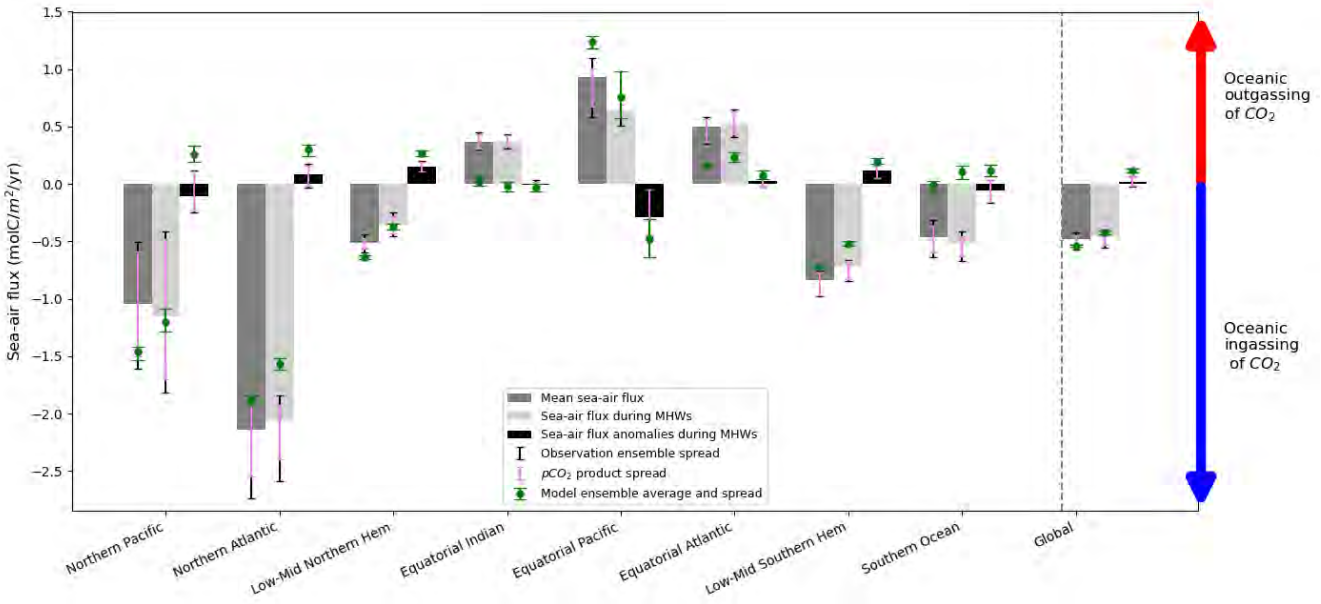

Figure 5: Mean sea-air CO_2 flux and sea-air CO_2 flux anomalies during MHWs for the years 1990-2019 in molC/m^2/yr. The bars represent the observation-based ensemble averages: the dark grey bars represent the flux at mean state, the light grey bars represent the flux during MHWs, and the black bars signify the flux anomalies during MHWs. The flux during MHWs is the sum of the anomaly and mean flux. The black error lines associated with the bars represent the spread of the 30 observation-based member ensemble (minimum and maximum values). The purple errors bars represent just the spread between the six observation-based pCO_2 products. The model ensemble average results are also shown as green dots, and the green error lines represent the 30 member ensemble spread (minimum and maximum values). Positive values signify oceanic outgassing of CO_2 and negative values signify oceanic ingassing of CO_2.

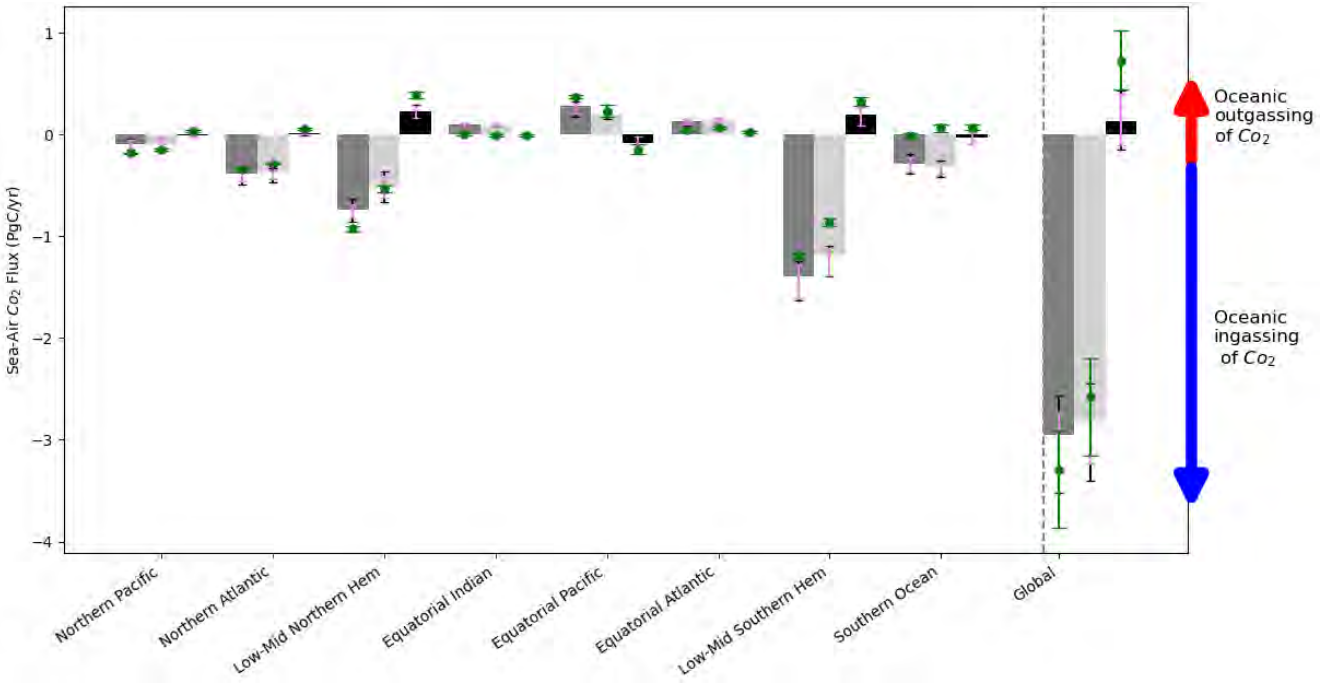

Figure 6: Mean sea-air CO_2 flux and sea-air CO_2 flux anomalies during MHWs for the years 1990-2019 integrated over the region's area in PgC/yr. The bars represent the observation-based ensemble averages: the dark grey bars represent the flux at mean state, the light grey bars represent the flux during MHWs, and the black bars signify the flux anomalies during MHWs. The flux during MHWs is the sum of the anomaly and mean flux. The black error lines associated with the bars represent the spread of the 30 observation-based member ensemble (minimum and maximum values). The purple errors bars represent just the spread between the six observation-based pCO_2 products. The model ensemble average results are also shown as green dots, and the green error lines represent the 30 member ensemble spread (minimum and maximum values). Positive values signify oceanic outgassing of CO_2 and negative values signify oceanic ingassing of CO_2.

4.1.5 Observation-based data product differences

We can see in Figure 5 a noticeable spread in the sea-air CO_2 flux anomalies among the 30 observation-based ensemble members. The anomaly spread among different pCO_2 products (violet error bars in Figure 5) seems to dominate the overall observation-based ensemble spread (black error bars in Figure 5). To confirm if the spread is mainly due to the variation in pCO_2 products or wind products, we compare flux anomalies calculated for each pCO_2 product with the average wind product to flux anomalies calculated for each wind product with the average pCO_2 product. Globally, minimal variation is found between CO_2 flux anomalies calculated with different wind products and the average pCO_2 product (Figure 7b). The anomaly values are also quite uniform between all products in each study region (Figure 8b). Comparing the flux anomalies calculated with different pCO_2 products and average wind, reveals the main source of variation within the observation-based. Globally, we observe a larger spread (0.082 molC/m^2/yr) in flux anomalies calculated with different pCO_2 products (Figure 7a). This effect is enhanced regionally. The spread of flux anomalies calculated with the different pCO_2 products across all regions ranges from 0.049 - 0.339 molC/m^2/yr, nearly 4 to 5 times greater than the wind product variation. This implies the choice of pCO_2 product to be a greater source of variation than the choice of wind product.

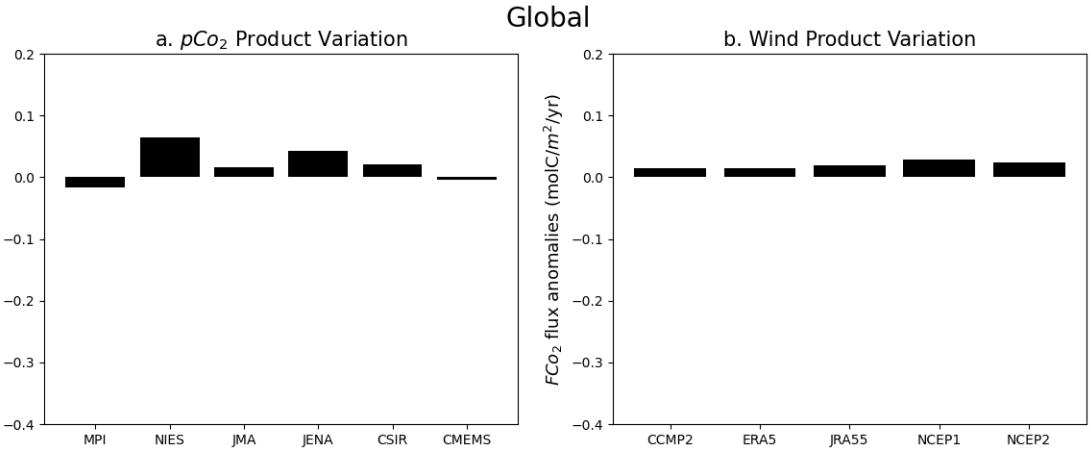

Figure 7: The global sea-air CO_2 flux anomalies (in mol C/m^2/yr) during MHWs for the years 1990 to 2019 for the different observation-based pCO_2 products (left) and observation-based wind products (right). The six pCO_2 products are MPI, NIES, JMA, JENA, CMEMS, CSIR. The five wind products are CCMPv2, ERA5, JRA55, NCEP2, NCEP1. The anomalies for each pCO_2 product are calculated with the average wind product; and the anomalies for each wind product are calculated with the average pCO_2 product. The y-axis scale for the anomalies is the same as Figure 8 to allow for easy comparison.

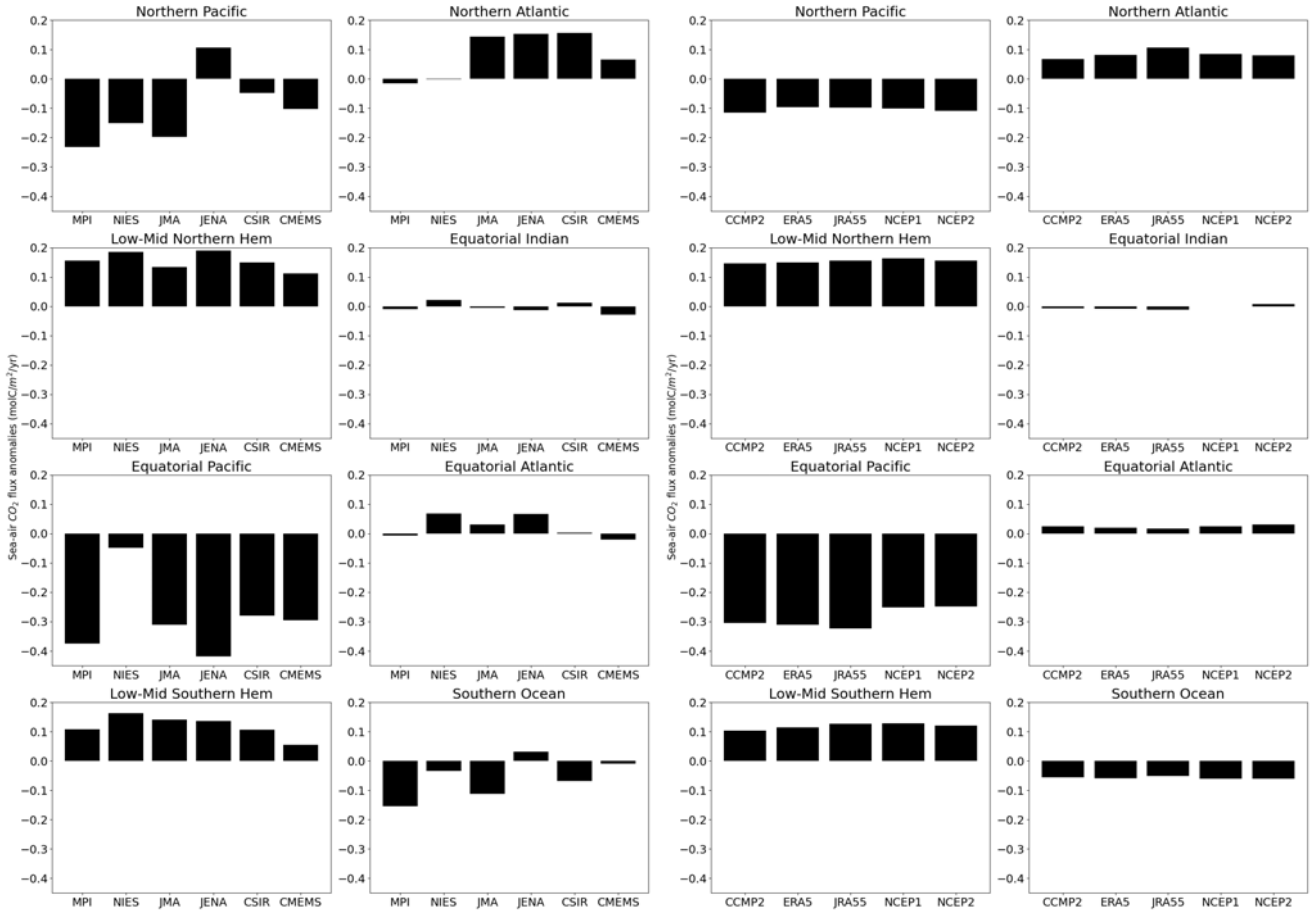

(a) pCO_2 Product Spread (b) Wind Product Spread

Figure 8: The pCO_2 and wind observation-based product spreads for the sea-air CO_2 flux anomalies (in molC/m^2/yr.) during MHWs in the eight study regions for the time period 1990-2019. The six pCO_2 products are MPI, NIES, JMA, JENA, CMEMS, CSIR. The five wind products are CCMPv2, ERA5, JRA55, NCEP2, NCEP1. The anomalies for each pCO_2 product are calculated with the average wind product; and anomalies for each wind product are calculated with the average pCO_2 product.

4.2 Drivers of Sea-Air CO_2 Flux Anomalies during MHWs

4.2.1 Mean state and anomalies of flux components

First, the five inputs to the sea-air CO_2 flux equation are presented at mean state and as anomalies during MHWs for both the observation-based (Figure 9) and model data (Figure 10) ensemble averages. This establishes a background understanding of how each flux driver changes during MHWs. This analysis is restricted to the area where all six observation-based pCO_2 products have data despite model data existing for the entire global ocean.

During MHWs, the gas transfer velocity (k_w) experiences a global decrease of -1.042 (-4.164 to 1.931) cm/hr (observation-based) and -2.262 (-2.390 to -2.078) cm/hr (model) compared to the mean state (Figure 9b, 10b). The regions experiencing stronger decreased gas transfer velocity are in the western Pacific, the western equatorial Pacific, north Atlantic, and tropical Indian Ocean. In both the observation-based and model results, a zonal dipole pattern emerges in the equatorial Pacific: an anomalous increase in k_w near the eastern equatorial Pacific off the coast of Peru and anomalous decrease in k_w in the western equatorial Pacific (Figure 9b, 10b). Since the gas transfer velocity is driven by wind speed, we can investigate

the model data mean wind speed and anomalies during MHWs to see if this is causing the dipole. We see the same zonal dipole pattern emerge in the equatorial Pacific for wind speed anomalies during MHWs (Supplementary Figure 4). Localized variations in wind patterns due to specific atmospheric responses and pressure gradients near the coast of South America/eastern equatorial Pacific could potentially cause this zonal dipole pattern in the wind speed and gas transfer velocity anomalies during MHWs. For instance, the shift in the Walker cell circulation that occurs during warmer sea surface temperatures leads to a decrease in atmospheric pressure in the eastern equatorial Pacific bringing more deep convection which could potentially cause positive anomalies in wind speed (and thus gas transfer velocity). Additionally, small areas of increased gas transfer velocity appear in some western boundary currents such as the Gulf Stream and Kuroshio currents. Lastly, a noticeable difference between the observation-based and model data is the magnitude of the gas transfer velocity anomalies. The model data shows larger gas transfer velocity anomalies across the global ocean compared to those of the observation-based data.

The solubility anomalies mirror the global MHW magnitude and intensity patterns (Figure 2b, 2e, 2a, 2d). This is expected as CO_2 solubility is mainly a function of temperature (equation 4). The higher the temperature, the lower the solubility. The global average solubility decrease during MHWs is -0.754 μmol/m^3/μatm (observation-based) and -0.996 (-1.005 to -0.891) μmol /m^2/μatm (model). The strongest decreases are observed in the equatorial Pacific, Northern Pacific, Northern Atlantic, and Southern Ocean regions (Figure 9d, 10d). The spatial patterns of the anomalies are in high agreement between the observation-based and model data.

The oceanic pCO_2 anomalies mirror the spatial pattern of sea-air flux anomalies during MHWs (Figure 9h, 10h). At the global scale, oceanic pCO_2 is increased during MHWs by 0.090 (-0.731 to 2.020) μatm (observation-based) and 2.324 (1.559 to 3.055) μatm (model). However, these global mean values are deceiving because there is great regional variation in the oceanic pCO_2 anomalies. For instance, in the equatorial Pacific there is anomalously lower partial pressure of CO_2 during MHWs. In contrast, we see anomalously higher pCO_2 in the mid latitudes. Additionally, hot-spots of particularly higher pCO_2 emerge off the northwestern coast of the United States, the North Atlantic, North Pacific and off the northwestern coast of Australia. The considerably different reactions of pCO_2 during MHWs emphasize the impact of regional characteristics and processes.

On average, atmospheric pCO_2 is higher in the mid-high latitudes and lower in the tropics. During MHWs, the atmospheric pCO_2 globally decreases by -0.444 μatm (observation-based) and -0.129 (-0.406 to 0.336) μatm (model) (Figure 9f, 10f). A decrease in atmospheric pCO_2 is possibly a result of the warmer SSTs increasing the water vapor in the atmosphere and reducing the atmosphere's capacity to intake pCO_2. Differences in the global spatial patterns between the observation-based and model based results arise, which will be further discussed in the regional results section. However it should be noted that the model data is based on 'concentration runs', where the atmosphere has a restoring flux. Restoring fluxes are often used so that values do not deviate too far from observations and defined equilibriums can be reached.

Unfortunately, due to the pCO_2 areal mask minimal areas with sea ice remain. We can initially see some areas of lower sea ice fraction during MHWs, however the pCO_2 mask prevents any substantial interpretation. Overall, the observation-based and model data are in agreement in terms of spatial patterns and magnitude for the flux component mean states. Some spatial and magnitude differences

appear when comparing the anomalies during MHWs for each flux component. For instance, the model estimates stronger anomalies than the observation-based data for the gas transfer velocity, solubility, and particularly oceanic pCO_2. The opposite holds for atmospheric pCO_2, where the model based results show weaker anomalies during MWHs. The observation-based and model data disagree most in spatial patterns for the gas transfer velocity and atmospheric pCO_2, particularly in the Southern Ocean for gas transfer velocity and the equatorial region for atmospheric pCO_2.

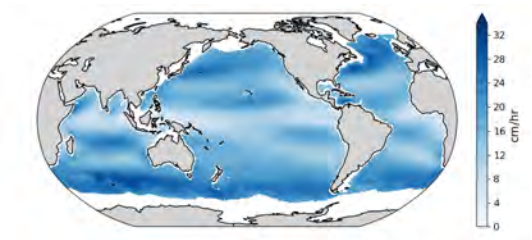

(a) k_w mean

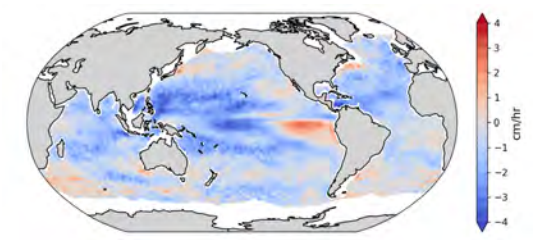

(b) k_w anomaly

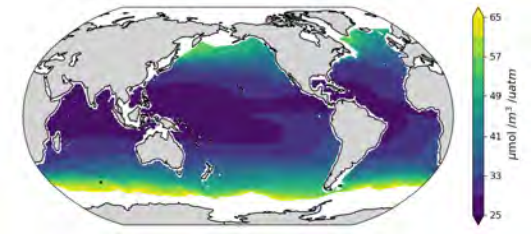

(c) solubility mean

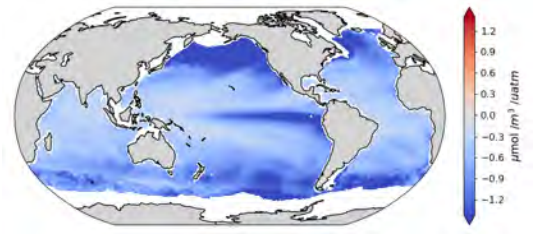

(d) solubility anomaly

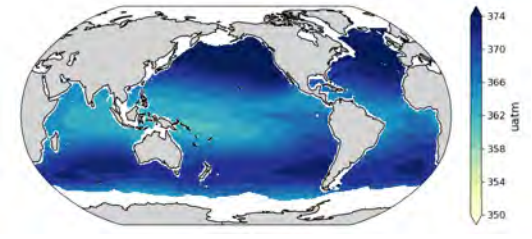

(e) $pCO_{2_{\text{atm}}}$ mean

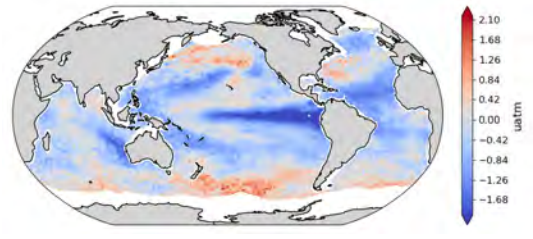

(f) $pCO_{2_{\text{atm}}}$ anomaly

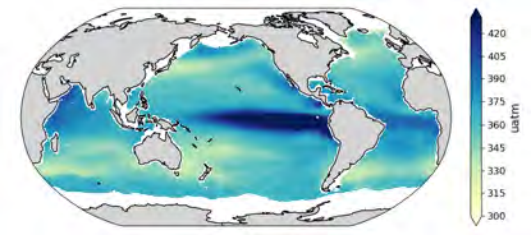

(g) $pCO_{2_{\text{oc}}}$ mean

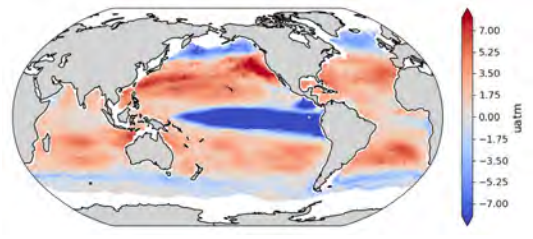

(h) $pCO_{2_{\text{oc}}}$ anomaly

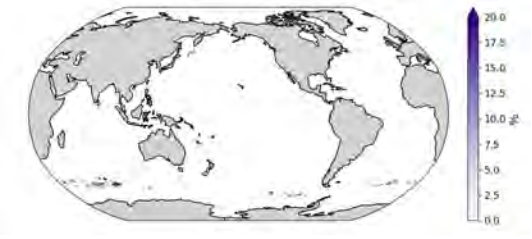

(i) ice fraction mean

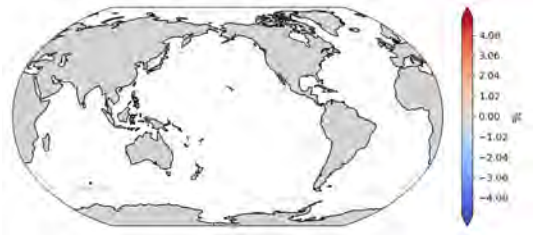

(j) ice fraction anomaly

Figure 9: Global depiction of the mean state (left column) and anomalies during MHWs (right column) for each component of the sea-air CO_2 flux equation for the observation-based data for 1990-2019. The gas transfer velocity (k_w) is the ensemble average across the five wind products. The oceanic CO_2 is the ensemble average across the six observation-based pCO_2 products. An areal pCO_2 product mask including only the areas where all six pCO_2 products have data is applied here for each driver.

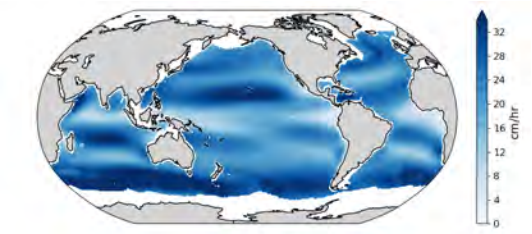

(a) k_w mean

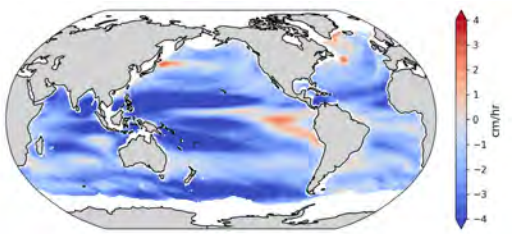

(b) k_w anomaly

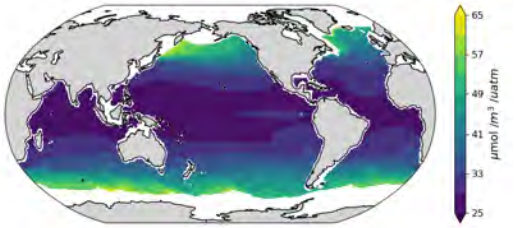

(c) solubility mean

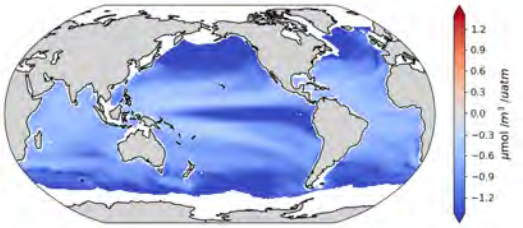

(d) solubility anomaly

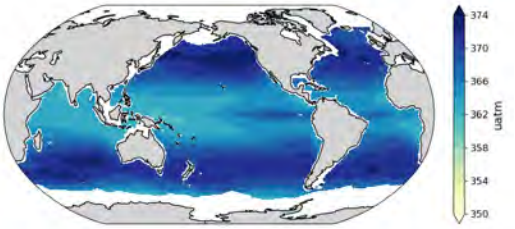

(e) $pCO_{2_{\text{atm}}}$ mean

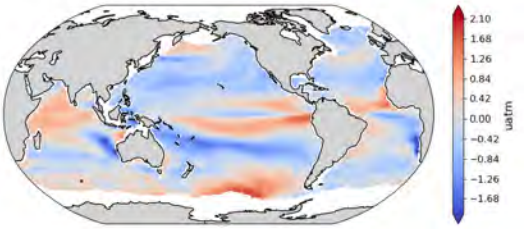

(f) $pCO_{2_{\text{atm}}}$ anomaly

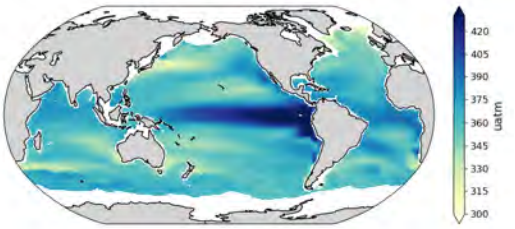

(g) $pCO_{2_{\text{oc}}}$ mean

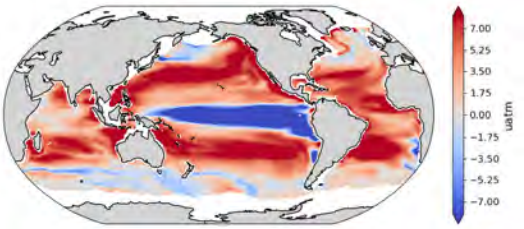

(h) $pCO_{2_{\text{oc}}}$ anomaly

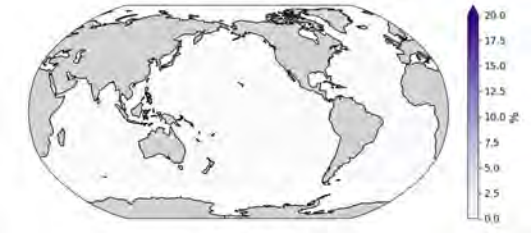

(i) ice fraction mean

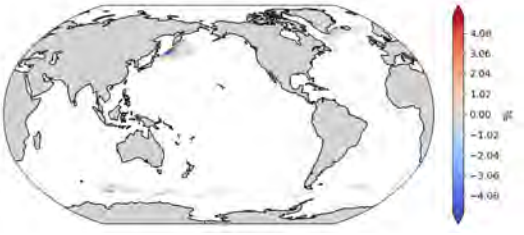

(j) ice fraction anomaly

Figure 10: Global depiction of the five sea-air CO_2 flux drivers in their mean state (left column) and anomalies during MHWs (right column) for the model ensemble average over the years 1990 to 2019. Original model data is available for the global ocean but is masked to match the area of the observation-based data.

4.2.2 Global patterns of sea-air CO_2 flux decomposition

For the observation-based data, we can directly compare the 'true' SeaFlux anomaly and the sum of the Taylor decomposition terms as they are both calculated with monthly data. For the model-based

data, the monthly recalculated flux anomalies and sum of decomposition terms are compared. The 'true' model flux anomalies are calculated with 2 hourly data that is then averaged to monthly means. Since the decomposition uses monthly data, it would be inconsistent if we compare the decomposition sum to the true 2-hour flux anomalies. Hence, we have to compare the decomposition results to the monthly recalculated flux anomalies.

For the observation-based product results, the sum of the decomposition contributions mirrors the true SeaFlux anomaly quite well (Figure 11a, 11b). The global mean difference between the masked SeaFlux anomaly (0.036 mol C/m^2/yr) and the sum of the Taylor decomposition contributions is -0.015 (-0.025 to -0.012) mol C/m^2/yr (Figure 11c). The largest differences stem from the north Pacific Ocean, particularly near the western boundary where the decomposition overestimates the outgassing anomaly, as well as in the equatorial Pacific and North Atlantic where the decomposition overestimates the ingassing anomaly.

For the model data, the sum of the Taylor decomposition terms also agrees well with the recalculated monthly flux anomaly. The mean difference between the masked model monthly flux anomaly (0.124 mol C/m^2/yr) and the sum of the decomposition terms is -0.043 (-0.057 to -0.025) mol C/m^2/yr (Figure 12c). The model decomposition seems to overestimate the flux anomaly on average. For instance, in the north Pacific, southwestern Pacific and southern Indian ocean the model decomposition overestimates the anomalous outgassing; and in the equatorial Pacific the decomposition overestimates the anomalous ingassing. More rare are regions where the decomposition underestimates the flux anomaly, such as in the North Atlantic where the decomposition underestimates the outgassing anomaly. The regions of disagreement are similar between the model and observation-based. The relative differences between the decomposition sums and true flux anomalies are similar for the observation-based and model data. The main difference between the observation-based and model data results seems to be the magnitude in which the decomposition overestimates the flux anomalies. This can be expected since the model flux anomalies are larger in magnitude than the observation-based flux anomalies to begin with.

Of the five flux contributions, oceanic $p\mathrm{CO}_2$ immediately emerges as the dominating contribution to the overall sea-air CO_2 flux anomaly during MHWs in the observation-based and model-based data (Figure 11g, 12g). If the flux anomaly is negative (positive), signifying anomalous ingassing (outgassing), then a negative (positive) contribution from the Taylor decomposition signifies a concordance or reinforcement of the flux anomaly. The oceanic $p\mathrm{CO}_2$ shows strong negative contributions in the equatorial Pacific and high latitudes and strong positive contributions in the mid latitudes. This corresponds with a negative flux anomaly (anomalous ingassing of CO_2) in the equatorial Pacific and a positive flux anomaly (anomalous outgassing) in the low-mid latitudes. Thus, for both the observation-based and model data the large contribution of oceanic $p\mathrm{CO}_2$ suggests the flux anomalies during MHWs are mainly a result of the changes in oceanic $p\mathrm{CO}_2$. The presence of both strong positive and negative contributions of oceanic $p\mathrm{CO}_2$ across the global ocean counteract each other. As a result, the global mean $pCO_{2_{\mathrm{oc}}}$ contribution is only 0.013 (-0.024 to 0.073) mol C/m^2/yr (observation-based) and 0.148 (0.112 to 0.196) mol C/m^2/yr (model). Oceanic $p\mathrm{CO}_2$ is the only flux component where the observation-based and model-based differ considerably in magnitudes.

The second greatest contribution to flux anomalies is the gas transfer velocity (k_w) which represents wind (Figure 11d, 12d). On average k_w has a positive global contribution 0.013 (0.005 to 0.019)

molC/m^2/yr (observation-based) and 0.029 (0.021 to 0.038) mol C/m^2/yr (model) to the sea-air CO_2 flux anomaly during MHW events. A positive contribution of the gas transfer velocity can be understood by considering a low-mid latitude region where there is mean ingassing of CO_2 into the ocean. Since the partial derivative of the sea-air flux with respect to the gas transfer velocity includes the difference of pCO_2 between the ocean and atmosphere at mean state, a decrease in the gas transfer velocity during MHWs would drive a reduction in the mean ingassing state, leading to a positive contribution of k_w to the flux anomaly. Thus, the positive contribution of the gas transfer velocity means the wind speed and subsequently the gas transfer velocity is reduced in regions of CO_2 ingassing and increased in regions of CO_2 outgassing. In both the observation-based and model results, a zonal dipole of the gas transfer velocity contribution emerges in the equatorial Pacific, which was already observed with the gas transfer velocity anomalies. The western equatorial Pacific, a mean outgassing region, experiences a decrease in gas transfer velocity, and thus a negative contribution of k_w to the flux anomaly. For the eastern equatorial Pacific, the anomalous increase in gas transfer velocity along with the mean outgassing state results in the gas transfer velocity having a positive contribution to the flux anomaly. In terms of observation-based-model comparison, the model replicates well the observation-based findings only the magnitude of the model contributions is larger than those of the observation-based data.

Solubility and atmospheric pCO_2 have less of an impact on the sea-air CO_2 flux anomalies during MHWs. In terms of global means, solubility has a slightly positive contribution of 0.010 (0.009 to 0.012) mol C/m^2/yr (observation-based) and 0.012 (0.011 to 0.013) mol C/m^2/yr (model) to the flux anomalies during MHWs. A positive contribution from anomalously lower solubility in regions of mean ingassing (negative flux) such as the Northern Atlantic means the mean ingassing flux is reduced because the ocean can not absorb as much carbon. Likewise, a negative contribution from lower solubility in a region of mean outgassing such as the equatorial Pacific means the ocean's ability to release carbon is reduced. Negative solubility anomalies reduce the flux for both an ingassing or outgassing region. The largest contributions of solubility occur in the equatorial Pacific and high latitudes. The low to mid latitudes have essentially weaker solubility anomalies during MHWs and thus nearly no contribution to the flux anomalies during MHWs. The model data shows stronger solubility contributions in the northwest Atlantic and northwest Pacific where warm and cold currents mix which is not present in observation-based results.

The global average contribution of atmospheric pCO_2 to flux anomalies is 0.012 (0.012 to 0.012) mol C/m^2/yr (observation-based) and 0.006 (-0.028 to 0.026) mol C/m^2/yr (model). There are no emerging spatial patterns in terms of atmospheric pCO_2's contribution. Both the observation-based and model results show a nearly uniform positive contribution with some negative contributions on the edge of the study area in the Southern Ocean. It can be noted that the sign of the atmospheric pCO_2 contribution will be the opposite to the oceanic pCO_2 contribution due to the minus sign in the partial derivative show in equation 6e. Lastly, with the limited study area to observe the sea ice contribution to sea-air CO_2 flux anomalies, it is just initially seen that sea ice has a global contribution of -0.015 (-0.091 to -0.000) mol C/m^2/yr (observation-based) and -0.022 (-0.030 to -0.010) mol C/m^2/yr (model) to sea-air flux anomalies during MHWs. A negative contribution from sea ice is a result of reduced sea ice in a net outgassing region. Less sea ice would mean a greater area for CO_2 exchange between the sea-air and thus enhanced fluxes. We can only hypothesize that the sea ice contribution to the sea-air CO_2 flux anomalies would be stronger with a larger study area encompassing more sea ice.

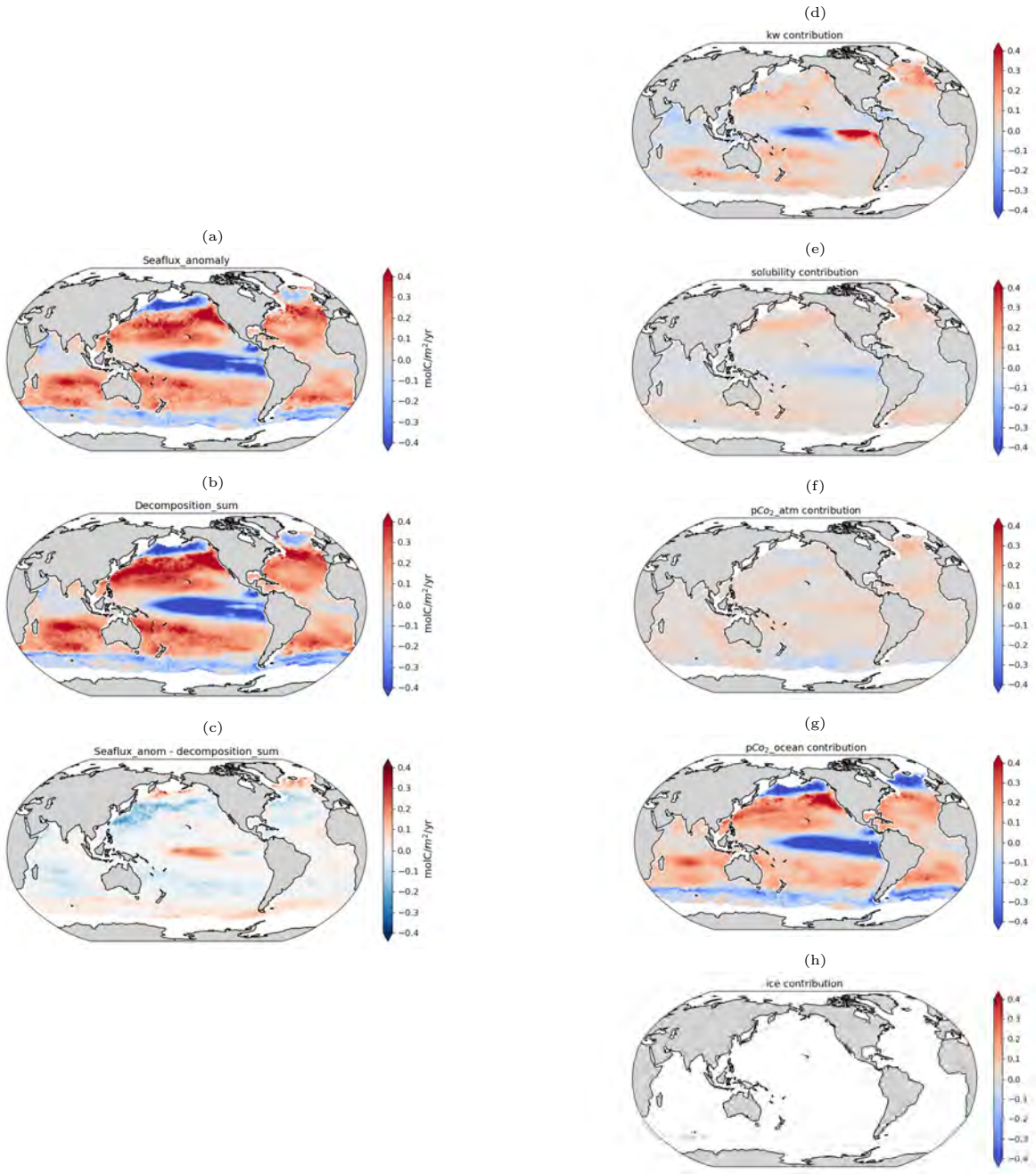

Figure 11: Global depiction of the flux decomposition for observation-based data using the average of $p\mathrm{CO}_2$ and wind products for the time-period 1990-2019. The right hand column shows the Taylor decomposition contributions of each flux component to the overall sea-air CO_2 flux anomaly during MHWs (k_w, solubility, $pCO_{2_{\mathrm{atm}}}$, $pCO_{2_{\mathrm{oc}}}$, ice). The left column shows the SeaFlux sea-air CO_2 flux anomaly during MHWs (a), the sum of the flux decomposition contributions (b), and the difference between the two (a - b). The data is masked to include only the regions where all six products have data.

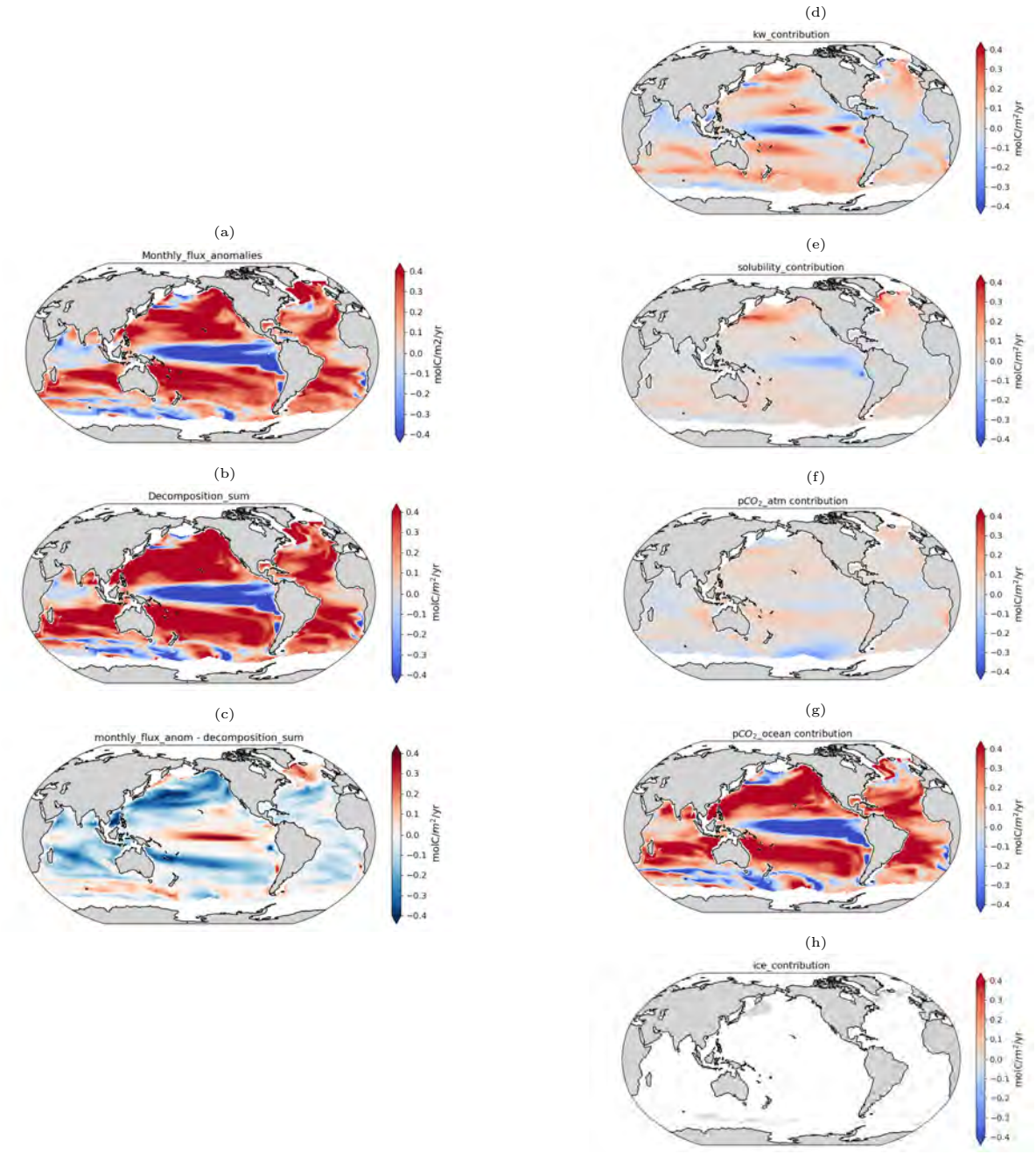

Figure 12: Global depiction of the flux decomposition for the ensemble average model data for the time period 1990-2019. The right hand column shows the Taylor decomposition contributions of each flux component (k_w, solubility, $pCO_{2_{\mathrm{atm}}}$, $pCO_{2_{\mathrm{oc}}}$, ice. The left column shows the recalculated monthly flux anomaly during MHWs (a), the sum of the flux decomposition contributions (b), and the difference between the two (a - b). The model data is masked to include only the regions where all six observation-based products have $p\mathrm{CO}_2$ data to allow for model-observation data comparisons.

4.2.3 Regional patterns sea-air CO_2 flux decomposition

The Taylor decomposition of the flux anomaly is presented for the 8 study regions in terms of the ensemble averages for both observation and model based data in Figure 13b, 14b. The sum of the five decomposition contributions is always compared to the 'true' flux anomaly (black line) and the manually recalculated flux anomaly (red line). We will consistently focus the results on the four regions that showed significant sea-air flux anomalies (equatorial Pacific, low-mid latitudes, and Southern Ocean). When interpreting these results, it must be remembered that the sea ice fraction is near zero due to the pCO_2 data product mask.

Beginning with the equatorial Pacific, the strong negative flux anomaly signifying anomalous ingassing, is clearly driven by oceanic pCO_2's negative contribution to the flux anomaly (Figure 13). The lower than usual oceanic pCO_2 anomalies combined with the region's mean outgassing state leads to a lower outgassing flux which is seen as a negative contribution. The oceanic pCO_2 contribution is -0.261 (-0.382 to -0.014) mol C/m^2/yr (observation-based) and -0.442 (-0.733 to -0.212) mol C/m^2/yr (model), which is equivalent to about 86% (observation-based) and 66% (model) of the region's total flux anomaly. At the same time, the reduced gas transfer velocity in the western equatorial Pacific as a result of weaker winds also contributes to the anomalous ingassing / negative flux anomaly. Often, warm SSTs are associated with the El Niño phenomenon, as it is an invasion of warm water off the west coast of northern South America (Holbrook et al., 2019; Oliver et al., 2018). El Niño is associated with low Southern Oscillation (ENSO) index which brings reduced trade winds and reduced middle-latitude westerlies (Bacastow, 1976). The lower solubility due to the warmer SSTs also contributes to the anomalous ingassing, but to a much lesser degree. Atmospheric pCO_2 is the only flux component that has a net contribution counteracting the overall flux anomaly. Summing the decomposition terms reveals the decomposition slightly overestimates the ingassing flux anomaly in the equatorial Pacific on average by 0.063 mol C/m^2/yr (observation-based) and 0.194 mol C/m^2/yr (model) compared to the 'true' or monthly recalculated flux anomaly.

For the low-mid latitudes regions, the contribution of oceanic pCO_2 continues to dominate the flux anomaly: 0.133 (0.092 to 0.184) mol C/m^2/yr (observation-based) and 0.148 (0.112 to 0.196) mol C/m^2/yr (model). This indicates the anomalous outgassing is a result of anomalously higher oceanic pCO_2. None of other flux components strongly impact the sea-air CO_2 flux anomaly. For example, the contribution of the gas transfer velocity in the NH low-mid latitudes is only 0.029 (0.020 to 0.036) mol C/m^2/yr (observation-based) and 0.030 (0.026 to 0.034) mol C/m^2/yr (model); and the solubility term contribution for the NH low-mid latitudes is 0.008 (0.006 to 0.009) mol C/m^2/yr (observation-based) and 0.009 (0.008 to 0.010) mol C/m^2/yr (model). For the SH low-mid latitudes, similar numbers prevail. The contribution of the gas transfer velocity in the SH low-mid latitudes is only 0.035 (0.032 to 0.044) mol C/m^2/yr (observation-based) and 0.046 (0.041 to 0.051) mol C/m^2/yr (model); and the solubility term contribution for the SH low-mid latitudes is 0.014 (0.013 to 0.018) mol C/m^2/yr (observation-based) and 0.014 (0.013 to 0.015) mol C/m^2/yr (model). For both low-mid latitude regions, all the flux components have a net positive contribution to the anomalous outgassing. In terms of observation-model comparisons, the decomposition replicates the true anomaly well in the observation-based data but less so with the model data. For instance, in the NH low-mid latitude region the decomposition overestimates the true anomaly by only 0.019 mol C/m^2/yr in the observation-based data but 0.106 mol C/m^2/yr in the model data. For the SH low-mid latitudes the decomposition overestimates the true anomaly on average by 0.040 mol C/m^2/yr

(observation-based) and 0.122 mol C/m^2/yr (model).

For the Southern Ocean, oceanic pCO$_2$ continues to drive the flux anomalies during MHWs in both the observation-based and model data (Figure 13,14). For the observation-based data, where the Southern Ocean experiences an enhanced ingassing flux during MHWs, the lower oceanic pCO$_2$ has on average a negative contribution to the negative flux anomaly of -0.108 (-0.226 to 0.021) mol C/m^2/yr (observation-based). In the model data, the Southern Ocean experiences anomalous outgassing which equates to a positive flux anomaly. The model data also does not predict such homogeneous pCO$_2$ anomalies as the observation-based data. Rather, the model predicts a mix of positive and negative pCO$_2$ anomalies in the Southern Ocean study region. On average the pCO$_2$ anomaly for the Southern Ocean in the model data is positive. Thus, the higher pCO$_2$ anomalies have a positive contribution to the outgassing anomaly of 0.214 (0.129 to 0.354) mol C/m^2/yr (model). The gas transfer velocity also has a positive contribution to flux anomalies: 0.009 (0.006 to 0.011) mol C/m^2/yr for the observation-based data and 0.058 (0.048 to 0.070) mol C/m^2/yr in the model data. This can be expected because the model predicts stronger gas transfer velocity anomalies in the Southern Ocean, compared to the observations which shows nearly no change in gas transfer velocity during MHWs in the Southern Ocean. The contribution of atmospheric pCO$_2$ contributes to more ingassing in the observation-based and model data. However due to the different signs of the flux anomalies, the atmospheric pCO$_2$ contribution strengthens the negative flux anomaly in the observation-based data, and weakens the positive flux anomaly in the model-based data results. Finally, the Southern Ocean is one of the few study regions with remaining sea ice after applying the pCO$_2$ areal mask. In both the observation-based and model data, since the Southern Ocean is a net ingassing region, the reduced sea ice coverage provides a greater extent for sea-air exchange, thus it enhances the mean flux. Since the flux anomaly in the observation-based data is negative (representing enhanced uptake) the contribution of lower sea ice is negative, supporting enhanced uptake. For the model data, since the flux anomaly is positive (anomalous outgassing), but less sea ice allows for enhanced mean flux exchange, the sea ice contribution is negative.

Lastly, the accuracy between the sum of decomposition terms and flux anomaly for the observation-based data is greater compared to the results using model data. For example, with the observation-based data, the sum of the decomposition terms remains in the ensemble spread for the data for all eight regions. This statement does not hold for the model data. In the low-mid latitudes regions, the model decomposition sum is outside ensemble spread of the calculated monthly flux anomaly.

(a)

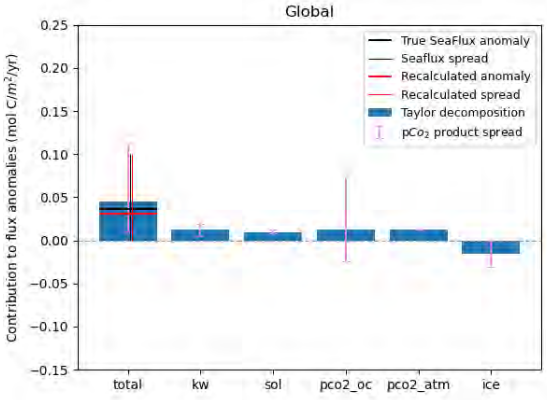

(b)

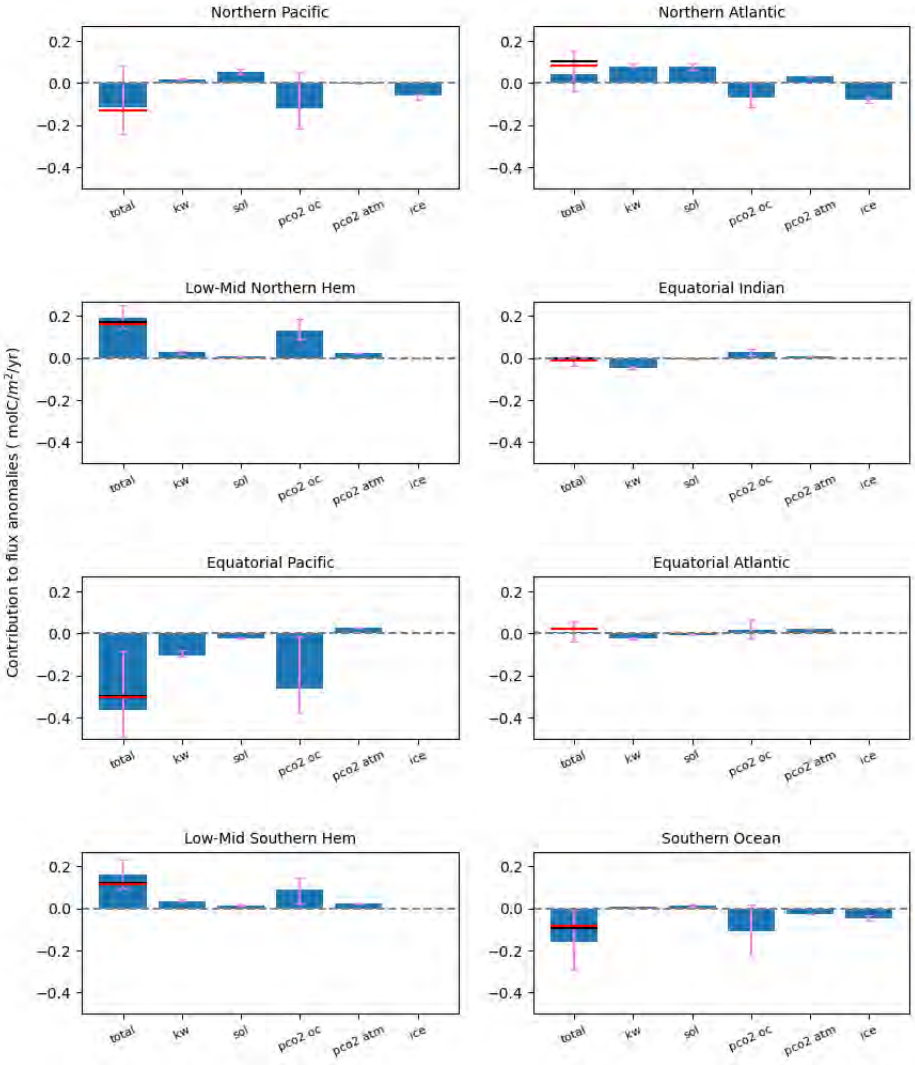

Figure 13: Global and regional Taylor decomposition of sea-air CO_2 flux drivers for the average observation-based pCO_2 and wind data. The blue bars are the average ensemble contribution for each flux component. The total bar is the sum of the five flux contributions. Data is for the time period 1990-2019. The horizontal black line is the true SeaFlux anomaly, with the pCO_2 product spread represented with the dashed black vertical line. The red line is the recalculated flux anomaly described in Section 3.5.3. The violet spread bars represent the range (minimum and maximum values) for each contribution between just the 6 pCO_2 data products.

(a)

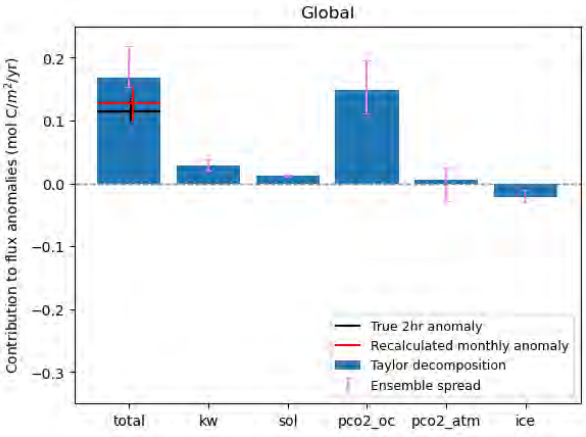

(b)

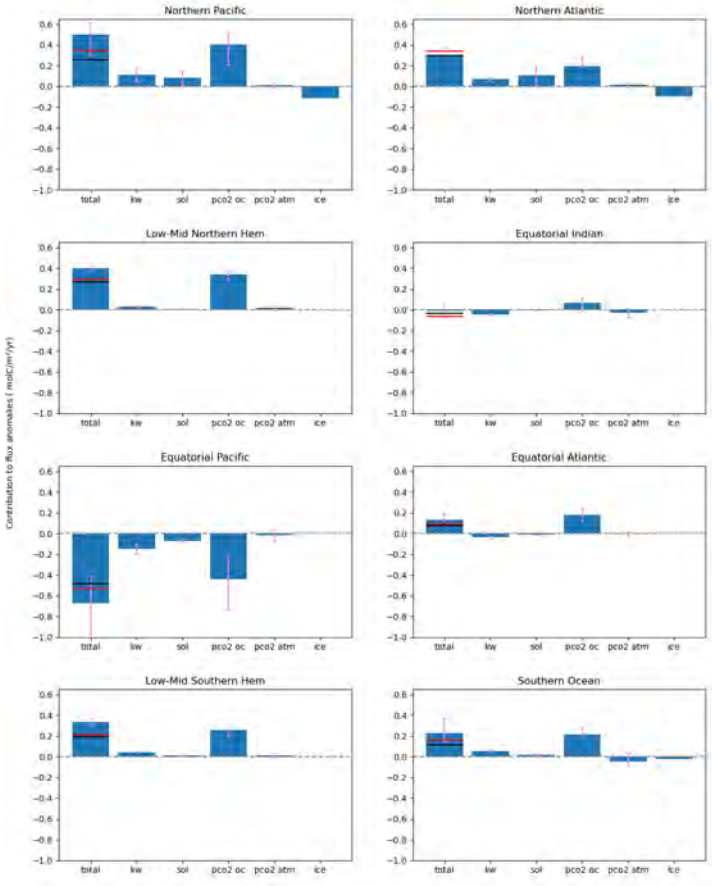

Figure 14: Global and regional Taylor decomposition of the sea-air CO_2 flux for the model ensemble average. The blue bars are the average ensemble contribution for each flux component. The total bar is the sum of the five flux contributions. Data is for the time period 1990-2019. The monthly flux anomaly (red line) is recalculated using monthly flux equation inputs as described in 3.5.3. The true 2 hourly flux anomaly (black line) is obtained from the model data which uses the original model out in 2 hour time-steps. The violet spread bars represents the ensemble range (minimum and maximum values) for each contribution.

4.3 Drivers of oceanic pCO_2 anomalies during MHWs

4.3.1 Mean state and anomalies of pCO_2 components

First, the four main components of oceanic pCO_2 (alkalinity, dissolved inorganic carbon, sea surface temperature, and salinity) are presented at mean state and as anomalies during MHWs for the observation-based and model data (Figure 15, 16). This is to illustrate how each pCO_2 component varies naturally and during MHWs across the global ocean. Results are limited to the area where all six observation-based pCO_2 products have data. For the observation-based data results, only DIC is reported with a spread as it is calculated from six different pCO_2 products. Observation-based alkalinity, salinity, and sea surface temperature were calculated with one product and therefore do not have an ensemble spread. For the model-based data, results are still presented as the ensemble average with the spread of the 30 members.

Alkalinity is not influenced by changes in temperature, pressure nor by the exchange of CO_2 between the ocean and atmosphere (Williams and Follows, 2011). This is why it is considered a conservative tracer and used as an input to measure other carbonate system parameters. At the surface, alkalinity is influenced by freshwater fluxes such as precipitation and evaporation which are exhibited in salinity changes. This is why we see alkalinity mimicking patterns of salinity: lower concentrations in the high latitude regions compared to subtropical areas and higher alkalinity concentrations in the open ocean particularly subtropical gyres (Figure 15a, 15c). Alkalinity distributions are also impacted by biological production at the surface such as calcification and production of soft matter, and dissolution and remineralization at depth (Planchat et al., 2023). The regional variations in alkalinity and salinity at mean state are mainly a result of the dominating effect of evaporation or precipitation which concentrate or dilute alkalinity and salinity.The main regions of high alkalinity concentrations at mean state emerge in the Northern Atlantic, South Atlantic, and eastern subtropical Pacific.

Since alkalinity acts as a conservative tracer, the global decrease in alkalinity during MHWs of -1.37 μmol/kg (observation-based) and -2.213 (-2.770 to -1.810) μmol/kg (model) can only be a result of indirect changes from warmer SSTs. During MHWs, alkalinity seems to experience a decrease in the tropics (especially in the equatorial Pacific and equatorial Atlantic). The decrease in alkalinity during MHWs is possibly a result of less mixing and dilution initiated by weaker winds. During MHWs, the weaker gas transfer velocities observed in section 4.2, can lead to less mixing, which results in less deep water brought to the surface. Thus, any parameter with a vertical profile could be impacted during MHWs. Since alkalinity generally increases with depth due to the dissolution of $CaCO_3$ in most regions (Takahashi et al., 1993), less mixing and upwelling of deep water results in lower alkalinity at the surface. Additionally, MHW events often bring more precipitation especially in the equatorial Pacific where MHWs are associated with El Niño which is characterized by weaker winds and warmer SSTs which warm the atmosphere above it, causing moisture-rich air to rise and develop into rain clouds. Greater precipitation dilutes the tracers, leading to lower alkalinity values. Likewise, salinity experiences a global decrease of -0.014 psu (observation-based) and -0.028 (-0.038 to -0.021) psu (model) during MHWs. The salinity and alkalinity anomalies relative to mean state are of similar magnitude. For the observation-based data salinity anomaly is about 0.04% and alkalinity is 0.06% relative to mean state; and for the model data salinity anomaly is 0.08% and alkalinity is 0.09% relative to mean state. The strongest decrease in salinity

occurs in the equatorial Pacific. On the other hand, some regions experience an increase in alkalinity and salinity such as the north Atlantic and areas of the mid latitudes. For alkalinity this could be due to the varying vertical profiles. For example, Takahashi et al. (2006) shows that total alkalinity *decreases* with depth in the North Atlantic. Thus, if MHW events cause less mixing and upwelling, this would lead to higher alkalinity values at the surface because the low-alkaline waters are not being brought to the surface.

Opposite to alkalinity, at mean state, DIC is lower in the low latitudes and increases toward the poles. This is mainly since the solubility of CO_2 in seawater increases with decreasing temperature. The spatial patterns of mean DIC and SST seem to share an inverse relationship (Figure 15e, 15g). DIC increases toward the poles and temperature decreases toward the poles. During MHWs where we have elevated SSTs globally and flux anomalies arising due to anomalously higher pCO_{2oc}, we see an net global decrease in DIC of -9.171 (-9.994 to -8.508) μmol/kg (observation-based) and -8.828 (-9.567 to -7.421) μmol/kg (model). These DIC anomalies are larger in absolute terms and relative to mean state compared to the alkalinity and salinity anomalies during MHWs. The negative DIC anomalies are a result of a global increase in oceanic pCO_2 (seen in section 4.2.2). Warmer temperatures increase the oceanic pCO_2, and to maintain equilibrium of pCO_2 between the atmosphere and ocean (following Henry's Law), DIC must decrease. Areas with stronger increases in SSTs during MHWs, align with the regions of stronger decreases in DIC (Figure 15f, 15h and Figure 16f, 16h). The decrease in DIC during MHWs can also be a result of less mixing and upwelling due to the weaker winds or thermal stratification occurring during MHWs. DIC increases with depth as organic particles sink and get remineralized (Takahashi et al., 2006), thus if less deep water is transported to the surface, DIC concentrations will be lower. Similarly, the warmer the surface waters, the lighter they become which increases density differences between cooler, heavier subsurface waters, making it more difficult for the surface and subsurface waters to mix.

In terms of comparisons between the observation-based and model data, the observation-based data exhibits a noticeable band of lower than usual alkalinity values during MHW along the equator and around 60°S, which is not seen with the model data. Instead the model data also shows a stronger decrease in alkalinity in the western equatorial Pacific and Indian Ocean, and positive alkalinity anomalies in the eastern equatorial Pacific. In addition, the similarity between the alkalinity and salinity anomalies is stronger in the model data compared to the observation-based data. Lastly, for DIC the model data shows some positive DIC anomalies in coastal areas such as the west coast of North America and east coast of South America whereas nearly no positive DIC anomalies emerge with the observation-based data.

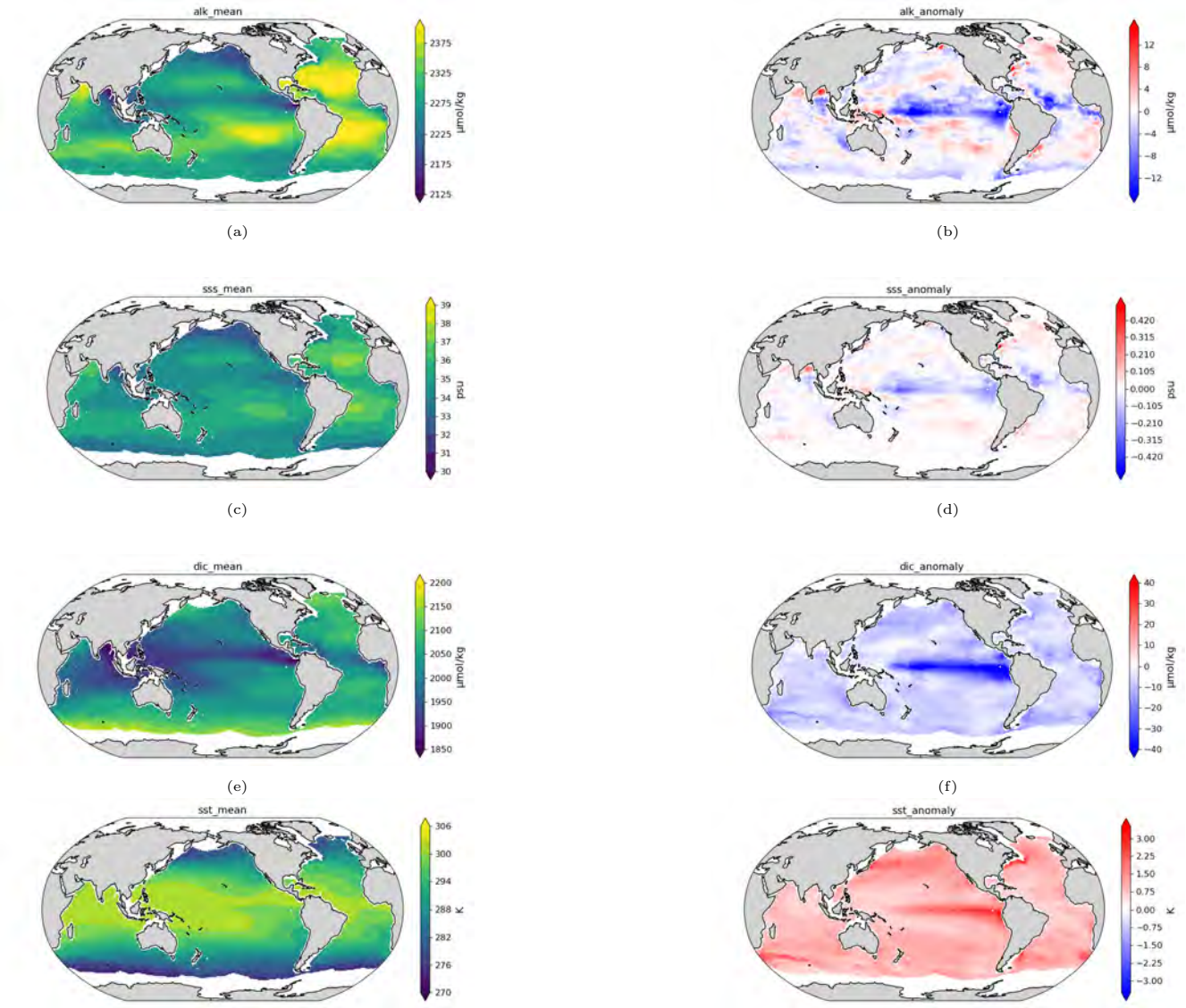

Figure 15: Global maps of the mean state (left column) and anomalies during MHWs (right column) of each contributing term to $pCO_{2_{oc}}$ for the observation-based data during 1990-2019. DIC is presented as the average between the six DIC products (derived from the six observation-based $p\mathrm{CO}_2$ products). The same areal mask used in the flux decomposition is applied.

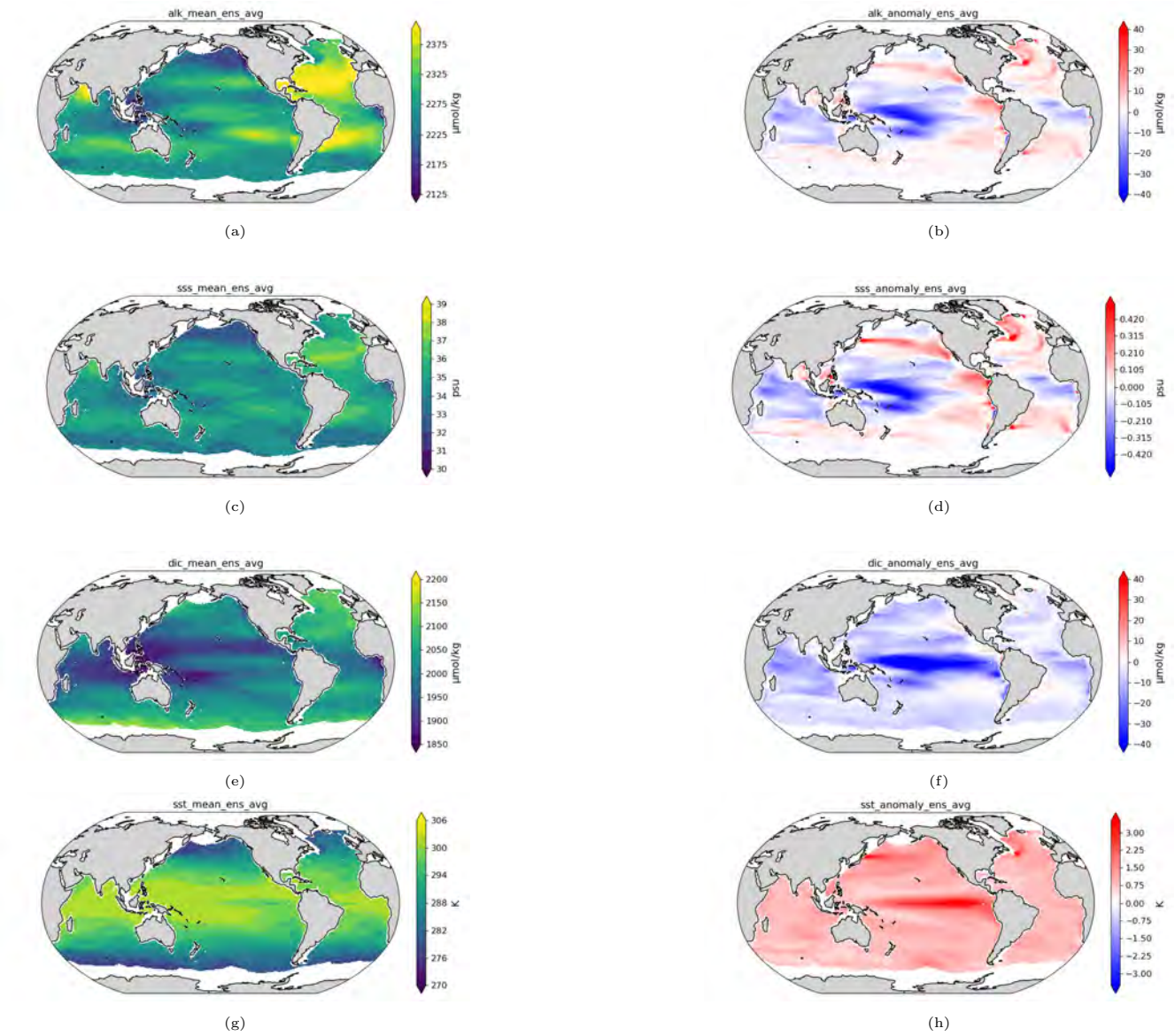

Figure 16: Global maps of the mean state (left column) and anomalies during MHWs (right column) of each contributing term to $pCO_{2_{\mathrm{oc}}}$ for the model ensemble average during 1990-2019. The same areal mask used in the flux decomposition is applied.

4.3.2 Global patterns of $p\mathrm{CO}_2$ decomposition

The Taylor decomposition of oceanic $p\mathrm{CO}_2$ anomalies during MHWs reveals on average, the $p\mathrm{CO}_{2oc}$ anomalies and consequently sea-air fluxes during MHWs are a result of higher-than-usual temperature and negative DIC anomalies. These two effects can be further understood. Firstly, higher temperature anomalies decrease the solubility of CO_2 in seawater, which causes an increase in oceanic $p\mathrm{CO}_2$ since oceanic $p\mathrm{CO}_2$ is a ratio of CO_2 and solubility (DeVris, 2022):

$$\mathrm{K}_0 = \frac{[\mathrm{CO}_2]_{\mathrm{ocean}}}{\mathrm{pCO}_{2_{\mathrm{ocean}}}} \tag{8}$$

As a result, temperature has a positive contribution to pCO_{2oc} anomalies (Figure 17g and 18g). The global average contribution of temperature to pCO_{2oc} anomalies is 15.360 (15.244 to 15.421) μatm (observation-based) and 15.9392 (14.388 to 16.963) μatm (model). On the other hand, the lower DIC concentrations during MHWs lead to lower oceanic pCO_2 (Figure 17f and 18f). Oceanic pCO_2 can be expressed through the relationship of carbonate and bicarbonate ions, and three equilibrium constants (Sarmiento and Gruber, 2006):

$$\mathrm{pCO_2} = \frac{[\mathrm{K_2}]}{\mathrm{K_0} \cdot \mathrm{K_1}} \cdot \frac{(\mathrm{HCO_3^-})^2}{\mathrm{CO_3^{2-}}} \tag{9}$$

Knowing DIC is a sum of carbonic acid (H_2CO_3), which dissociates into bicarbonate (HCO_3-) and carbonate ($CO_3{}^{2-}$), if DIC is lower during MHWs, then the oceanic pCO_2 will also be lower. The global mean contribution of DIC to pCO_{2oc} anomalies is -17.253 (-18.478 to -16.003) μatm (observation-based) and -16.085 (-17.602 to -13.470) μatm (model). DIC and SST act as competing factors and nearly cancel out each other's effect on pCO_{2oc} anomalies on a global scale (Figure 17b and 18b). As a result, the global sum of the pCO_{2oc} decomposition terms is 0.616 (-0.440 to 1.452) μatm (observations) and 2.364 (1.789 to 3.023) μatm (model) (Figure 19a and 20a). The temperature effect on oceanic pCO_2 dominates at the global scale. However, the inharmonious sign of the pCO_{2oc} anomalies suggests that depending on the region, the dominating effect on pCO_{2oc} varies.

Alkalinity and salinity play a less influential role on oceanic pCO_2 anomalies during MHWs compared to DIC and temperature. Nevertheless, the global average of lower alkalinity concentrations during MHWs results in anomalously higher pCO_{2oc}. Alkalinity and pCO_{2oc} generally share an inverse relationship. A decrease in alkalinity means a weaker dissolution reaction of carbon dioxide in seawater, increasing H_2CO_3, and consequently increasing the partial pressure of CO_2 in the ocean. The global contribution of alkalinity to higher pCO_{2oc} is minor: 2.195 (2.159 to 2.213) μatm (observation-based) and 2.792 (2.235 to 3.546) μatm (model). The largest positive alkalinity contribution occurs in the equatorial Pacific where the largest negative alkalinity anomalies are observed (Figure 17d and 18d). In contrast, the north Atlantic and some mid latitude regions where higher than usual alkalinity concentrations are observed during MHWs contribute to negative pCO_{2oc} anomalies. Higher alkalinity concentrations shift the dissolution reaction of carbon dioxide in water to form carbonic acid to the right by consuming hydrogen ions, thus lowering the concentration of CO_2 in the ocean and hence the partial pressure of CO_2 in the ocean.

The weakest contribution of the four components of pCO_{2oc} is salinity. Oceanic pCO_2 is not strongly influenced by changes in salinity. The contribution of salinity to oceanic pCO_2 anomalies during MHWs is only -0.159 (-0.160 to -0.157) μatm (observation-based) and -0.282 (-0.373 to 0.219) μatm (model) (Figure 17e and 18e).

On average the pCO_{2oc} decomposition is able to replicate the pCO_{2oc} anomalies during MHWs. For both the observation-based and model, the spatial patterns of pCO_{2oc} anomalies are well captured by the decomposition. Globally, the observation-based decomposition slightly overestimates the SeaFlux pCO_{2oc} anomaly, with a difference of -0.440 (-0.723 to 1.49) μatm. This overestimation by the decomposition can be observed in the north Pacific, Atlantic Ocean, and edge of the Southern Ocean. At the same time, in the equatorial Pacific, the pCO_{2oc} decomposition underestimates the SeaFlux pCO_{2oc} anomaly (Figure 17c and 18c). For the model data, the sum of the pCO_{2oc} decomposition terms slightly underestimates

the positive pCO_{2oc} anomaly, with a global difference of 0.745 (0.679 to 0.810) μatm (model). The region of largest disagreement (largest underestimation by the decomposition) is in the eastern central Pacific (Figure 18c). The regional patterns are described in more detail in the next section.

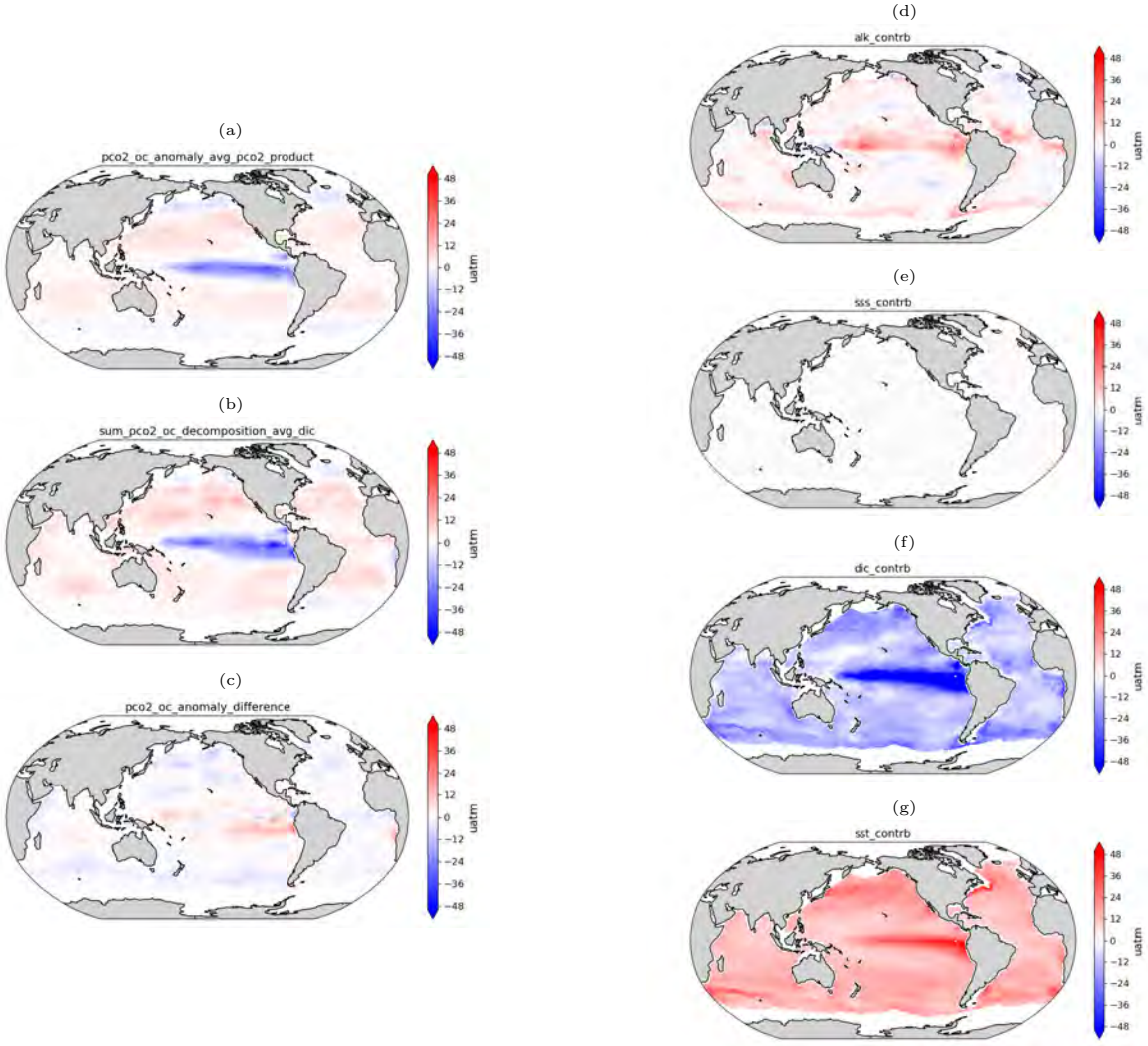

Figure 17: Global maps of the oceanic pCO_2 decomposition for observation-based data using the average of the six DIC products for the time-period 1990-2019. The right hand column shows the Taylor decomposition contributions of each pCO_{2oc} component to the overall pCO_{2oc} anomaly during MHWs (alkalinity, salinity, dissolved inorganic carbon, and sea surface temperature). The left column shows SeaFlux pCO_{2oc} flux anomaly during MHWs (a), the sum of the pCO_{2oc} decomposition contributions (b), and the difference between the two (a - b). The data is masked to include only the regions where all six DIC products.

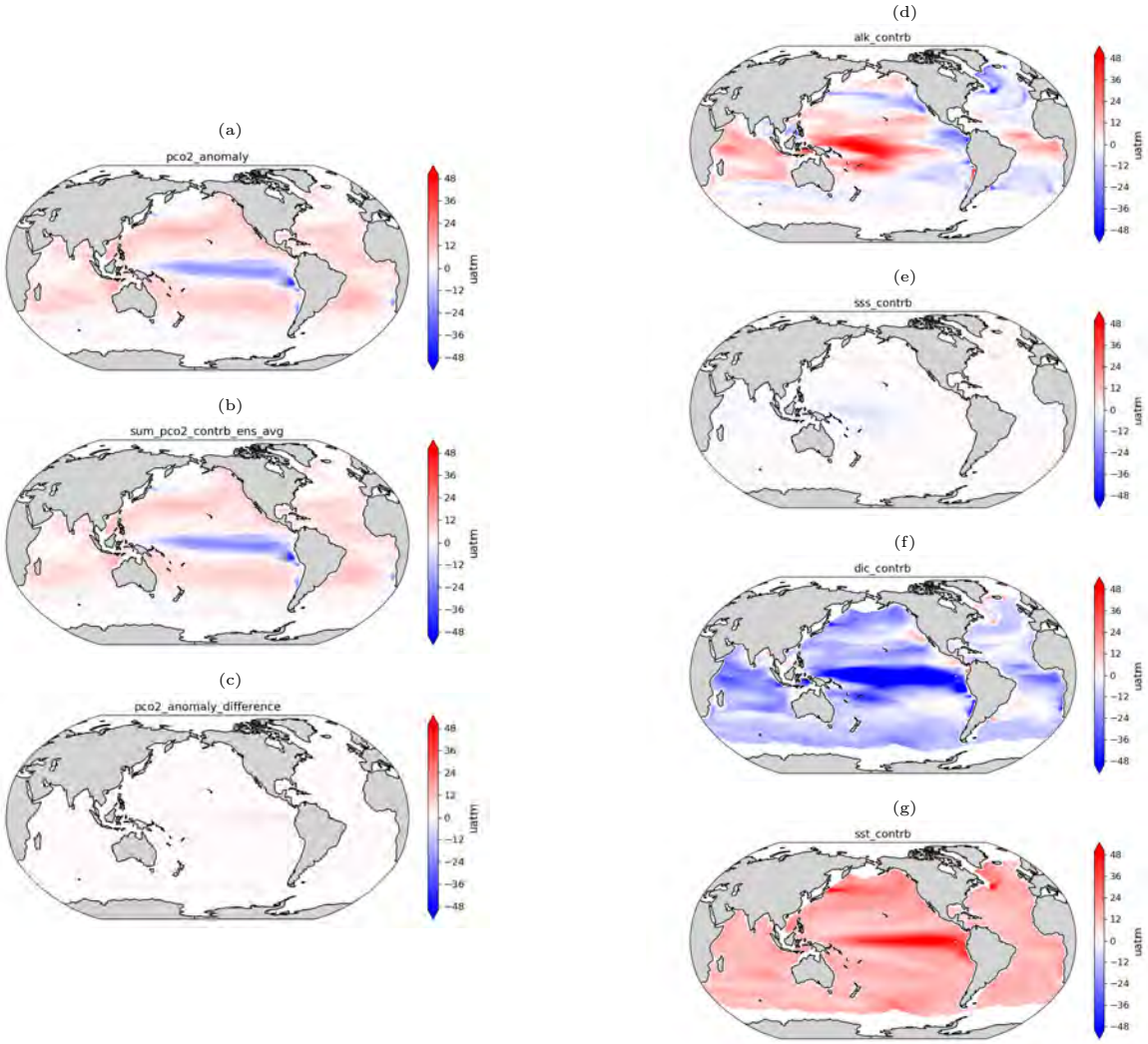

Figure 18: Global maps of the oceanic pCO_2 decomposition for the ensemble model average for time-period 1990-2019. The right hand column shows the Taylor decomposition contributions of each pCO_{2oc} component to the overall pCO_{2oc} anomaly during MHWs (alkalinity, salinity, dissolved inorganic carbon, and sea surface temperature). The left column shows ESM2M pCO_{2oc} flux anomaly during MHWs (a), the sum of the pCO_{2oc} decomposition contributions (b), and the difference between the two (a - b). The data is masked to include only the regions where all six observation-based DIC products have data for consistency during comparisons.

4.3.3 Regional patterns pCO_2 decomposition

The Taylor decomposition reveals the lower DIC to be the dominating contribution to the negative pCO_{2oc} anomaly during MHWs in the equatorial Pacific (Figure 19b, 20b). It is also the region with the largest negative contribution of DIC. In the equatorial Pacific, the DIC contribution is -37.220 (-41.428 to -27.819) μatm (observation-based) and -50.079 (-68.445 to -32.604) μatm (model). At the same time, the contribution of higher sea surface temperatures to increased pCO_{2oc} is 18.679 (18.488 to 18.977) μatm (observation-based) and 29.470 (21.943 to 34.826) μatm (model). Alkalinity also contributes to positive pCO_{2oc} anomalies by 7.325 (7.178 to 7.469) μatm (observation-based) and 10.960 (5.015 to 18.342) μatm (model). The DIC effect on pCO_{2oc} is able to offset the temperature and alkalinity effect of increased pCO_{2oc}, leading to a net result of lower than usual pCO_{2oc} and a reduced outgassing flux during MHWs. The stronger DIC effect on pCO_{2oc} in the equatorial Pacific is most likely a result of weaker trade winds in the region which can have cascading effects. Vogt et al. (2022) found over three-quarters of MHWs to

co-occur with El Niño, which is characterized by an eastward shift of the low pressure system and warmer SSTs. During El Niño events, easterly trade winds weaken and even reverse in the western and central equatorial Pacific. This induces eastward propagating Kelvin waves which deepen the thermocline (Feely et al., 2002). A deeper thermocline contributes to warmer surface waters as it pushes down further the cold water that feeds upwelling. However, the depth of the thermocline and strength of trade winds control the upwelling rate of deeper waters with higher DIC concentrations. Thus, weaker winds and a steeper thermocline reduce the upwelling of subsurface water which leads to lower surface DIC concentrations and lower $p\mathrm{CO}_2$ anomalies. Comparing the observation-based and model based results in equatorial Pacific, we see the model data results have a slightly greater accuracy of the decomposition to the 'true' $p\mathrm{CO}_2$ anomaly than the observation-based results. For example, in the model data, the difference between the true $p\mathrm{CO}_2$ anomaly (-10.036 μatm) and the sum of the $p\mathrm{CO}_2$ decomposition terms in the equatorial Pacific region is 0.543 μatm. Whereas in the observation-based data, the difference is -2.394 μatm (for a true $p\mathrm{CO}_2$ anomaly of -9.574 μatm).

In the low-mid latitudes, temperature generally has the dominating effect on the $pCO_{2_{\mathrm{oc}}}$ anomalies (Figure 19b and 20b). In the Northern Hemisphere low-mid latitude region, the temperature contribution is 13.404 (12.635 to 14.081) μatm (observation-based) and 14.291 (13.555 to 14.970) μatm (model). Similarly, in the Southern Hemisphere low-mid latitude region the temperature contribution is 14.523 (14.171 to 14.800) μatm (observation-based) and 14.094 (12.985 to 15.026) μatm (model). The DIC contribution is -13.543 (-14.622 to -12.52524) μatm (observation-based) and -7.722 (-9.134 to -6.376) μatm (model) in the NH; and -13.303 (-14.884 to -12.316) μatm (observation-based) and -10.289 (-11.831 to -9.045) μatm (model) in the SH. The dominating thermal effect on $p\mathrm{CO}_2$ in the low-mid latitudes is more clearly exhibited in the model data. For the observation-based decomposition, the stronger thermal effect on $p\mathrm{CO}_{2oc}$ is evident in the SH low-mid latitudes. In the observation-based results for the NH low-mid latitude, the decomposition underestimates the total increase in $p\mathrm{CO}_{2oc}$. The temperature and DIC contribution are nearly in balance, but the positive contribution of lower alkalinity concentrations on $p\mathrm{CO}_{2oc}$ in the NH low-mid latitude tips the balance in favor of a thermally driven increase in $p\mathrm{CO}_{2oc}$. The contribution of alkalinity in the observation-based NH low-mid latitude is nearly double the contribution of alkalinity in the SH low-mid latitude region. The alkalinity contribution to $p\mathrm{CO}_{2oc}$ are: 1.214 (1.141 to 1.283) μatm (observation-based) and -0.636 (-1.740 to 0.883 μatm (model) for the NH low-mid latitudes; and 0.402 (0.390 to 0.410) μatm (observation-based) and 0.549 (-0.297 to 2.063) μatm (model) for the SH low-mid latitudes. Nonetheless, the anomalous outgassing observed in the low-mid latitudes is a more often a result of the warmer temperatures causing positive $p\mathrm{CO}_{2oc}$ anomalies which is partly dampened due to anomalously lower DIC.

Finally, for the Southern Ocean the observation-based data reveals the stronger ingassing flux during MHWs is a result of lower than usual DIC concentrations leading to negative $p\mathrm{CO}_{2oc}$ anomalies which offset the thermally driven increase in oceanic $p\mathrm{CO}_2$. The ocean is able to take up more CO_2 and the ingassing flux is strengthened during MHWs. As for the model data results, the anomalous outgassing or reduced uptake of the Southern Ocean is a result of a dominating thermal effect on oceanic $p\mathrm{CO}_2$. Several speculations can be made as to why we see a dominating thermal effect in the model data and dominating DIC effect in the observation-based data. First of all, differences can be related to the spatial variability in the Southern Ocean's sea-air CO_2 flux and the model's ability to simulate the same spatial

variability and circulation patterns. We already see differences between the observation-based and model data in the sign of the sea-air flux anomalies during MHWs - the first step of the analysis. Additionally, a weaker model simulation of vertical mixing with DIC rich subsurface waters could be one factor causing a lower DIC effect seen in the model data compared to observation-based data.

(a)

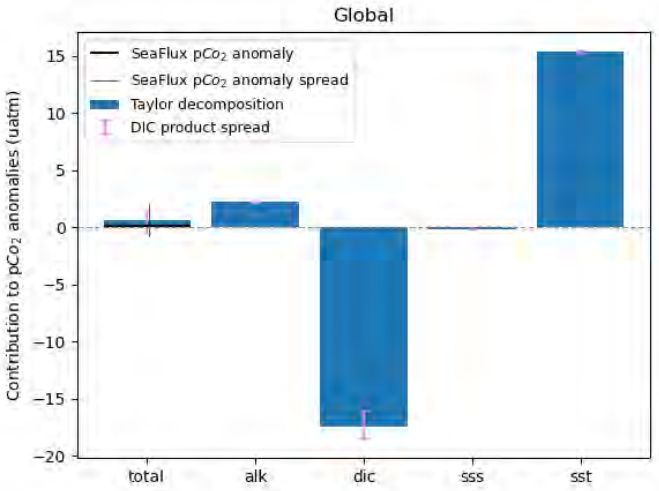

(b)

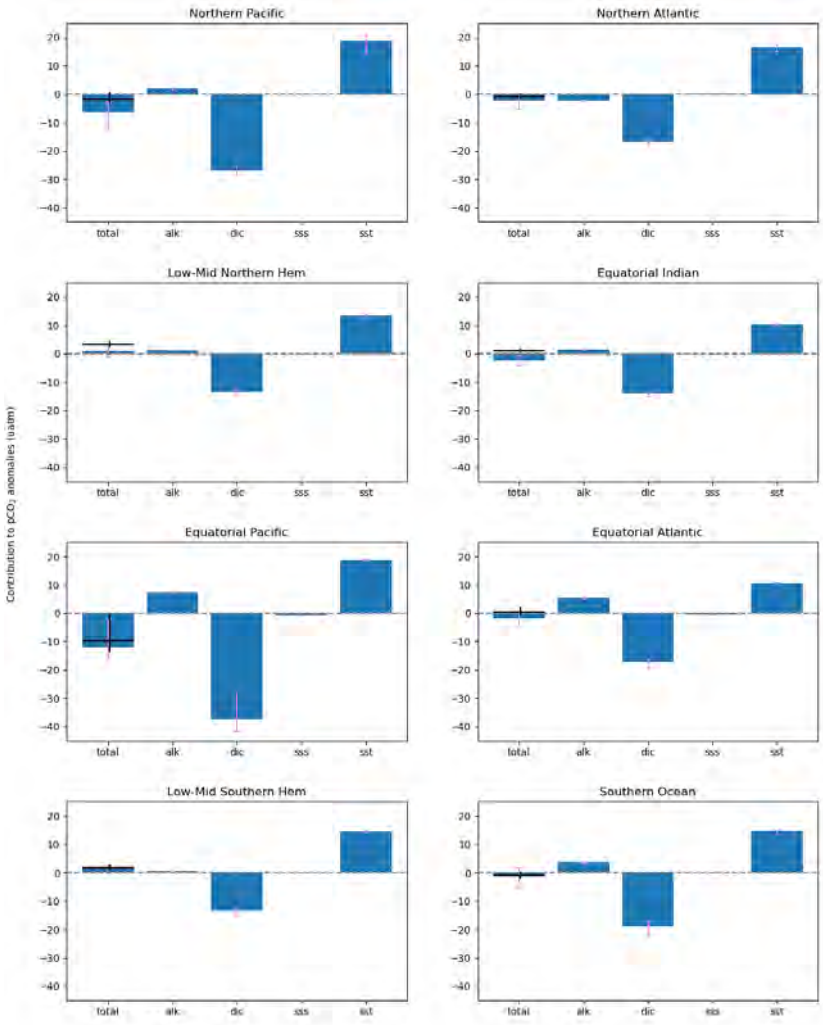

Figure 19: Global and regional flux decomposition of oceanic pCO_2 anomalies for the average observation-based DIC data for 1990-2019. The blue bars represent the average for each of the pCO_{2oc} decomposition contribution terms. The violet error bars correspond to the blue bars, and represent the range (minimum and maximum values) of each contribution across the 6 DIC data products. The black horizontal line represents the average pCO_{2oc} anomaly and the black vertical line represents the spread of these pCO_{2oc} anomalies between the six products.

(a)

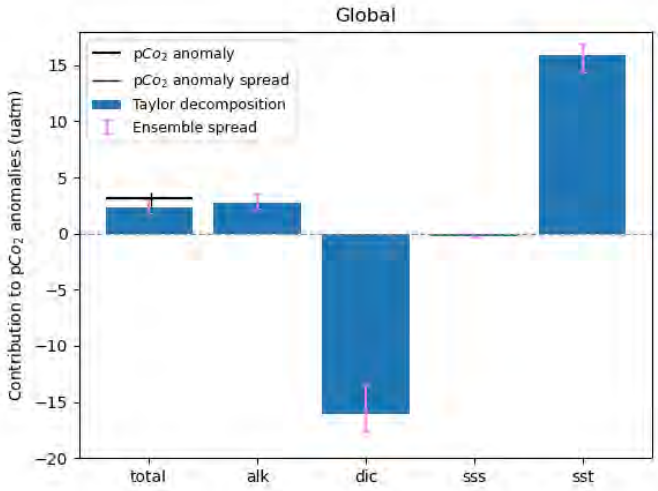

(b)

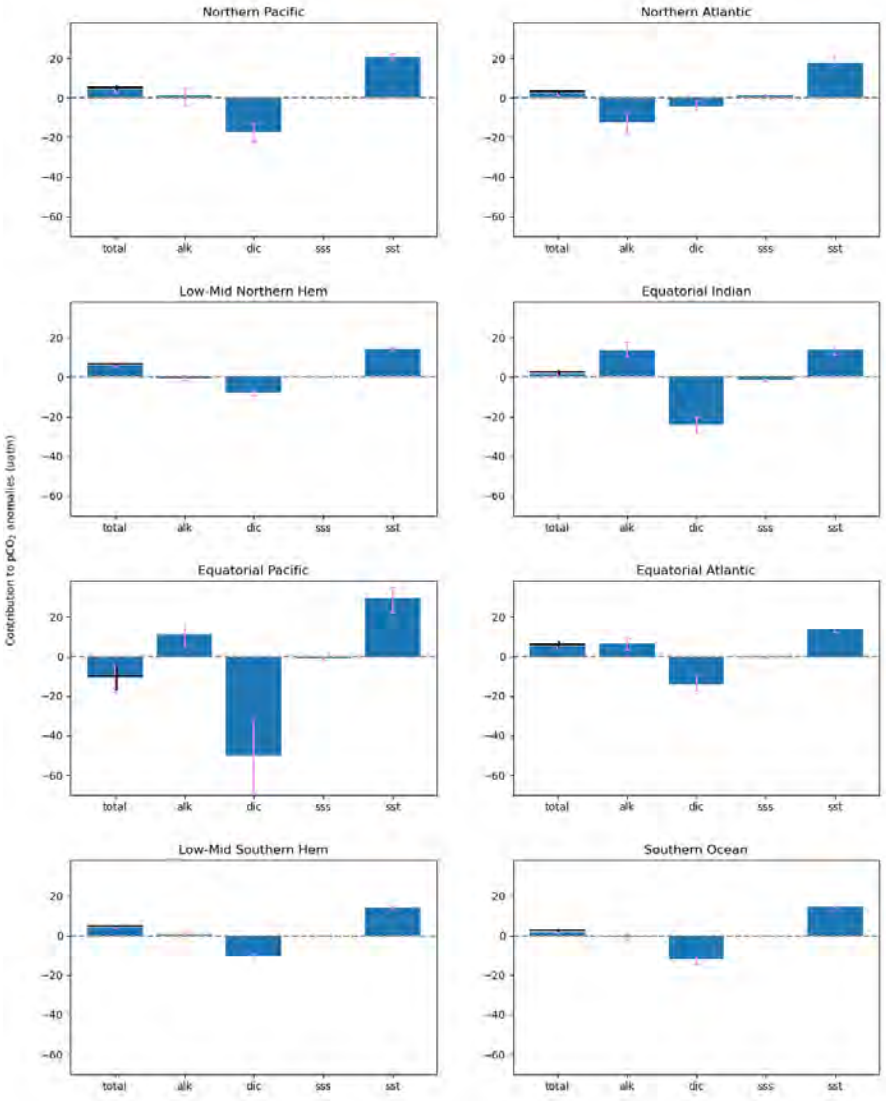

Figure 20: Same as Figure 19 but for ESM2M model ensemble data.

5 Discussion

Observation-based and model data show that during MHW events over the time period 1990 to 2019, the global ocean's average uptake of CO_2 is slightly reduced. This is in contrast to climate extremes in the terrestrial biosphere which have substantial impacts on carbon fluxes between the land and air (Reichstein et al., 2013). However, regional sea-air CO_2 fluxes can be substantial. In agreement with a previous study (Mignot et al., 2021) on sea-air CO_2 fluxes during MHWs, we find the sea-air CO_2 flux is reduced in the equatorial Pacific and low-mid latitude regions. Due to the differing directions of the mean sea-air exchange between these regions, a decrease in the flux during MHWs equates to an anomalous ingassing in the equatorial Pacific and anomalous outgassing in the low to mid latitudes of the Northern and Southern Hemisphere. Several studies (Fay and McKinley, 2017; Sarmiento and Gruber, 2006; Doney et al., 2009) on seasonal variations in sea-air CO_2 flux anomalies established flux changes to be a balance between thermal and non-thermal components. We find the sea-air CO_2 flux anomalies during MHWs to be mainly driven by oceanic pCO_2 anomalies which are a net result of two competing mechanisms: higher than usual temperatures (thermal effect) and lower than usual DIC (non-thermal DIC effect). This agrees with established findings that the most important factors to oceanic pCO_2 are temperature and DIC (Takahashi et al., 1993). Positive temperature anomalies lead to a reduction in the solubility of CO_2 in ocean water due to a lower Henry's law constant (Gilbert et al., 2016), causing an increase the pCO_2 in the ocean. An higher partial pressure of pCO_{2oc} directly causes a reduction in the ocean's ability to hold CO_2. While about two-thirds of the sensitivity of pCO_{2oc} to temperature is due to solubility changes, the dissociation constants that control the carbon system reactions also directly influence the sensitivity of pCO_{2oc} to temperature (Sarmiento and Gruber, 2006). On the contrary, lower DIC levels during MHWs induce negative pCO_{2oc} anomalies and increase the ocean's uptake ability, acting in contrast to the thermal effect on pCO_{2oc}. Depending on the region, the thermal or DIC dominates.

In agreement with Mignot et al. (2021) we find in the equatorial Pacific, the DIC effect on pCO_{2oc} dominates over the temperature effect. The tropical pacific study region of Mignot et al. (2021) can be compared to our equatorial Pacific study region. In our study we find the region's flux reduced by about -31% (-3% to -49%) (observation-based) and -39% (26% to 50%) (model), which on average is of similar magnitude found by Mignot et al. (2021) (40±9%). The good agreement in this reason can be due to the similar observation-based pCO_2 products used in the analysis. The four observation-based products used by Mignot et al. (2021) (JENA, CMEMS, CSIR, MPI) are also used in this thesis in addition to two others (JMA-MLR, NIES-FNN). Moreover, the high agreement in flux anomalies with Mignot et al. (2021) despite their consideration of only 'persistent' MHW events (lasting longer than 38 days and with a mean sea surface temperature anomaly of 2.3 degrees Celsius), could be due to the fact that MHW events in this region are known to manifest as long-lasting MHWs driven by El Niño (Holbrook et al., 2019). Additionally, these results align with Feely et al. (2002) who found lower sea-air CO_2 fluxes in the equatorial Pacific during El Niño periods of warmer SSTs particularly in 1991-94 and 1997-98. In fact, the occurrence of anomalous ocean uptake during El Niño events is well known (Keeling and Revelle, 1985; Bacastow, 1976).

In the low-to-mid latitude net ingassing study areas, our findings of reduced ingassing (or anomalous outgassing) mainly due to the dominant thermal effect on pCO_{2oc} is in agreement with what Mignot

et al. (2021) finds in their mid latitude North Pacific region. The low-mid latitude Northern Hemisphere study region of this thesis includes most of Mignot et al. (2021)'s North Pacific sink region (23.5°N–59.5°N, 123.5°E-121.5°W). In our study we find the region's flux reduced by about -30% (24-% to -34%) (observation-based) and 42% (37% to 47%) (model) which on average is of similar magnitude found by Mignot et al. (2021) (29±11%). Additionally, several studies (Fay and McKinley, 2017; Takahashi et al., 2002) on the seasonal variation of sea-air CO_2 fluxes find, during summertime in subtropical regions, the thermally driven increase in pCO_{2oc} is slightly counteracted by the decrease in pCO_{2oc} due to increase stratification which brings less DIC to the surface but, in the end, the thermal effect dominates. Furthermore, our findings of a reduced flux in the Northern Hemisphere low-mid latitudes agree with a recently published case study on sea-air CO_2 fluxes during MHWs in the Mid Atlantic (MAB) and South Atlantic Bight (SAB) (Edwing et al., 2024). Edwing et al. (2024) considers the two longest MHW events in the MAB and SAB which fall into the NH low-mid latitude study region of this thesis. In general, Edwing et al. (2024) attributes the reduced ingassing flux during MHWs to increased pCO_{2oc}, with the thermal effect as the main contributor the pCO_{2oc} anomalies despite an offset by non-thermal factors. Edwing et al. (2024) takes the analysis a step further by analyzing MHW months that exceed the 75th percentile of CO_2 flux anomalies and is able to identify conditions during substantial flux changes. This element is something to consider for future analyses to provide a better understanding of the drivers of substantial sea-air flux anomalies during MHWs.

We can further compare our findings to the recent publication by Duke et al. (2023). It must be noted that Duke et al. (2023) considers a specific region in the Northeast Pacific (45-62°N, 120-155°W). This region makes up just half of our North Pacific region. Thus, we must refer to global maps for comparison and not the regional results of our North Pacific region. Consistent with Duke et al. (2023), we observe this northeastern Pacific study region to be on average a net sink of CO_2 (albeit stronger in the model data than the observation-based data). Duke et al. (2023) considers sea-air flux anomalies during the strongest MHW ('the Blob' late 2013-2015) and another heatwave (mid 2018-2020). The Blob was associated with declines in local wind speed, decreased the mixing of deep, cold water to the surface and higher sea surface temperatures. These impacts are consistent with our observation-based findings of reduced gas transfer velocity (from weaker winds) and lower pCO_2 from reduced DIC at the surface. Duke et al. (2023) concludes impact of reduced winter mixing (because of decreased winds and increased density stratification) tipped the balance toward enhanced atmospheric CO_2 uptake during these marine heat waves. We both find a non-thermal effect driving lower pCO_2, leading to enhanced uptake of CO_2.

The Southern Ocean study region encompasses sea-air flux anomalies of opposite signs between the observation-based and model data but on average acts as a net sink CO_2 sink for both. The observation-based results indicate a strengthening in the sea-air CO_2 exchange (stronger ingassing) during MHWs. This is a result of negative DIC anomalies reducing the oceanic pCO_2 at the surface and allowing for greater CO_2 uptake. This result would be consistent with Lerner et al. (2021), which states in the Southern Ocean seasonal changes in sea-air CO_2 fluxes are mainly caused by changes in DIC. However, our model results suggest a decrease in the Southern Ocean's net uptake during MHWs as a result of the strong thermal effect increasing the pCO_2. The opposing findings between our observation-based and model data and the limited availability of observational-based data products for the Southern Ocean prevents a clear conclusion on how the Southern Ocean sea-air CO_2 flux reacts during MHWs. Mignot

et al. (2021) does not analyze results for the Southern Ocean, due to the minimal CO_2 flux anomalies during persistent marine heatwaves. Greater coverage and more robust observation-based data products are needed to understand the changes and drivers of sea-air CO_2 fluxes during MHWs in the mid-high latitude Southern Ocean.

This brings us to the limitations of the thesis research. Firstly, observation data is limited for pCO_2. The six observation-based pCO_2 products all use SOCAT pCO_2 data albeit different versions. Although this data coverage has increased four-fold from the 1990s to the 2000s, there are still regions where data is sparse such as the Southern Ocean and Indian Ocean. For context, Figure 21 shows on the top panel the measured data observations from 1957 onward, the middle panel shows the measured data observations for November 2020 to January 2021, and the bottom panel is shows data mainly for the period 2018-2020. For the period 2018-2021, there is minimal data in the Southern Ocean, south Pacific Ocean, Indian Ocean. This emphasizes the need for caution when interpreting observation-based results and comparing model results to them. Secondly, we use monthly sea surface temperature data during our identification of marine heatwaves. Ideally, SST data with daily resolution should be used to identify and characterize MHWs according to Hobday et al. (2016). For example, monthly SSTs cannot resolve many individual MHWs directly, since many events are shorter in duration than 1 month (Oliver et al., 2018; Vogt et al., 2022). In terms of the model-related limitations, only data from the GFDL ESM2M model is used. Ocean models with different resolutions simulate temperature extremes differently due to different choices of parameters, limitations, and as a result can differently simulate processes that can give rise to MHWs (Pilo et al., 2019). Thus, the usage of an ensemble of ESM model data would improve the robustness of the presented results. For instance, Frölicher et al. (2018) used a suite of ESM model simulations to assess MHW metrics for historical data of the past few decades. Additionally, the horizontal resolution (1°) of the ocean model component in the GFDL ESM2M is quite coarse which presents challenges in simulating small scale circulation patterns and basin-scale ocean variability particularly in smaller basins and coastal regions (Turi et al., 2018; Saba et al., 2016). The ocean model resorts to applying the Gent-McWilliams parameterization to simulate mesoscale (10-100km) circulation patterns (Dunne et al., 2012). An ideal improvement would be to use a global high-resolution model that resolves ocean eddies and has greater performance in coastal regions. Regarding the Taylor decomposition of the sea-air CO_2 flux, it assumes linearity but not all the components of the equation have linear functions. For example, the gas transfer velocity has a quadratic dependence on wind speed. As a result, the Taylor decomposition results can only provide an approximation. Other methods to understand the drivers of the sea-air CO_2 flux anomalies could be explored in future analyses such as a nonlinear regression which would take into account any nonlinear dependencies, a principal component analysis, or machine learning techniques. Additionally, the Taylor decomposition is performed with monthly data for solubility, gas transfer velocity, oceanic and atmospheric pCO_2 and sea ice fraction. However, the model is able to produce flux data in 2 hourly time steps. Theoretically this decomposition could be replicated using model output for the flux variables at daily or even 2 hourly time steps to possibly improve the accuracy of results and allow for a direct comparison between the true 2 hour flux anomalies and decomposition sum anomalies. Furthermore, using a higher temporal resolution data in the decomposition would give the opportunity for a more precise analysis such as comparing drivers between seasons and during the onset and decline phases of MHWs.

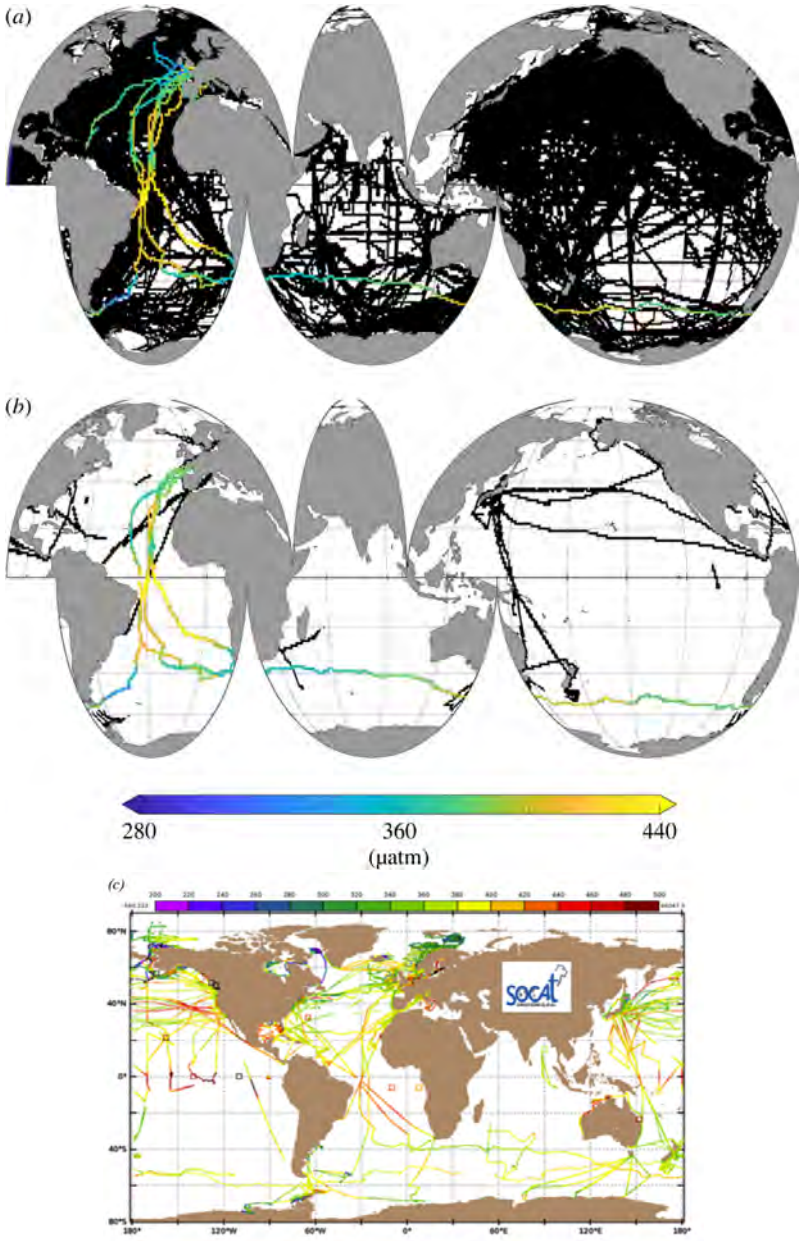

Figure 21: Measurements from ship and sailboat tracks in SOCAT version 2022 shown in black. The colored line indicates the measured fugacity of CO_2. The top panel (a) shows all data from 1957 onward and the middle panel (b) shows the data from November 2020 through January 2021. Figure from: Landschützer et al. (2023). Finally, the bottom panel (c) shows the new measurements for the SOCAT 2021 version, which is mostly data from 2018-2020. Figure from: Metzl (2021). It should be noted that the difference between partial pressure and fugacity is less than 1% (DeVris, 2022).

6 Conclusion

In this thesis we investigated the impact of MHW events on sea-air CO_2 fluxes across the global ocean for the time period 1990-2019. While the global average uptake of CO_2 is only slightly reduced during MHWs, regional sea-air CO_2 flux anomalies appear substantial, mainly in the equatorial Pacific, low to mid latitudes of the Northern and Southern Hemisphere and the Southern Ocean. The impact of marine heatwave events on sea-air CO_2 fluxes depend on several often competing climatic factors that influence the sea-air CO_2 flux. Firstly, the magnitude and sign of the sea-air CO_2 flux depends on solubility, gas transfer velocity, sea ice, and the difference between oceanic and atmospheric pCO_2. A Taylor decomposition of the sea-air CO_2 flux anomalies during marine heatwaves reveals oceanic pCO_2 to be the dominating factor. Oceanic pCO_2 depends on the interaction of several factors such as sea surface temperatures, dissolve inorganic carbon, salinity, and alkalinity. Decomposing the change in oceanic pCO_2 during marine heatwaves, reveals oceanic pCO_2 anomalies are mainly a net result of changes in temperature (thermal effect) and DIC (non-thermal effect). During marine heatwaves, the thermal and non-thermal effects on pCO_2 counteract each other: warmer sea surface temperatures increase oceanic pCO_2 (thermal effect) while lower DIC decreases pCO_2 (non-thermal effect). Depending on the oceanic region, either the thermal or non-thermal DIC effect emerges as the dominating mechanism behind the pCO_2 anomalies and thus the sea-air CO_2 flux anomalies during MHWs. In general, the thermal effect dominates in the tropics and the DIC effect dominates in the low to mid latitude regions. Greater variation and areas of mismatch arise in the high latitude regions and between the observation-based and model results. However on average, the DIC effect dominates the high latitudes in the observation-based data.

This thesis presents the ability of ESM data to replicate observation-based flux anomalies and their drivers during MHWs, thus the next step in this research could be to investigate the physical and biogeochemical processes leading to negative DIC and and positive temperature anomalies during MHWs using carbon and temperature tendency terms. The DIC anomalies can be caused by many different processes such as, vertical diffusion, vertical advection, freshwater anomalies, and biological activities (Mignot et al., 2021). It would be interesting to uncover which is causing the changes in DIC and compare results between regions. Likewise, the temperature change at the ocean surface is caused by several processes such as the net sea-air heat exchange (net incoming longwave and shortwave radiation, and net latent and sensible heat fluxes), vertical diffusion, and mixing (Vogt et al., 2022). Comparing the drivers of temperature anomalies between regions would also be of interest. In looking at the underlying drivers of the DIC and temperature anomalies, it would also be of interest to conduct an analysis with a seasonal component. This thesis considers all seasons at once but the dominating effect (thermal or non-thermal) on oceanic pCO_2 can vary depending on the season. Additionally, since the focus of this research is to understand how MHW events impact the sea-air CO_2 flux, and with MHWs becoming more intense, frequent, and longer in duration over the last few decades (Oliver et al., 2018; Frölicher et al., 2018; Laufkötter et al., 2020) it would be logical to extend the study into the future to assess impacts and drivers under different global warming levels. This would offer insights on whether the driving processes of sea-air CO_2 flux anomalies during MHWs depend on the background climate state.

7 Supplementary Information

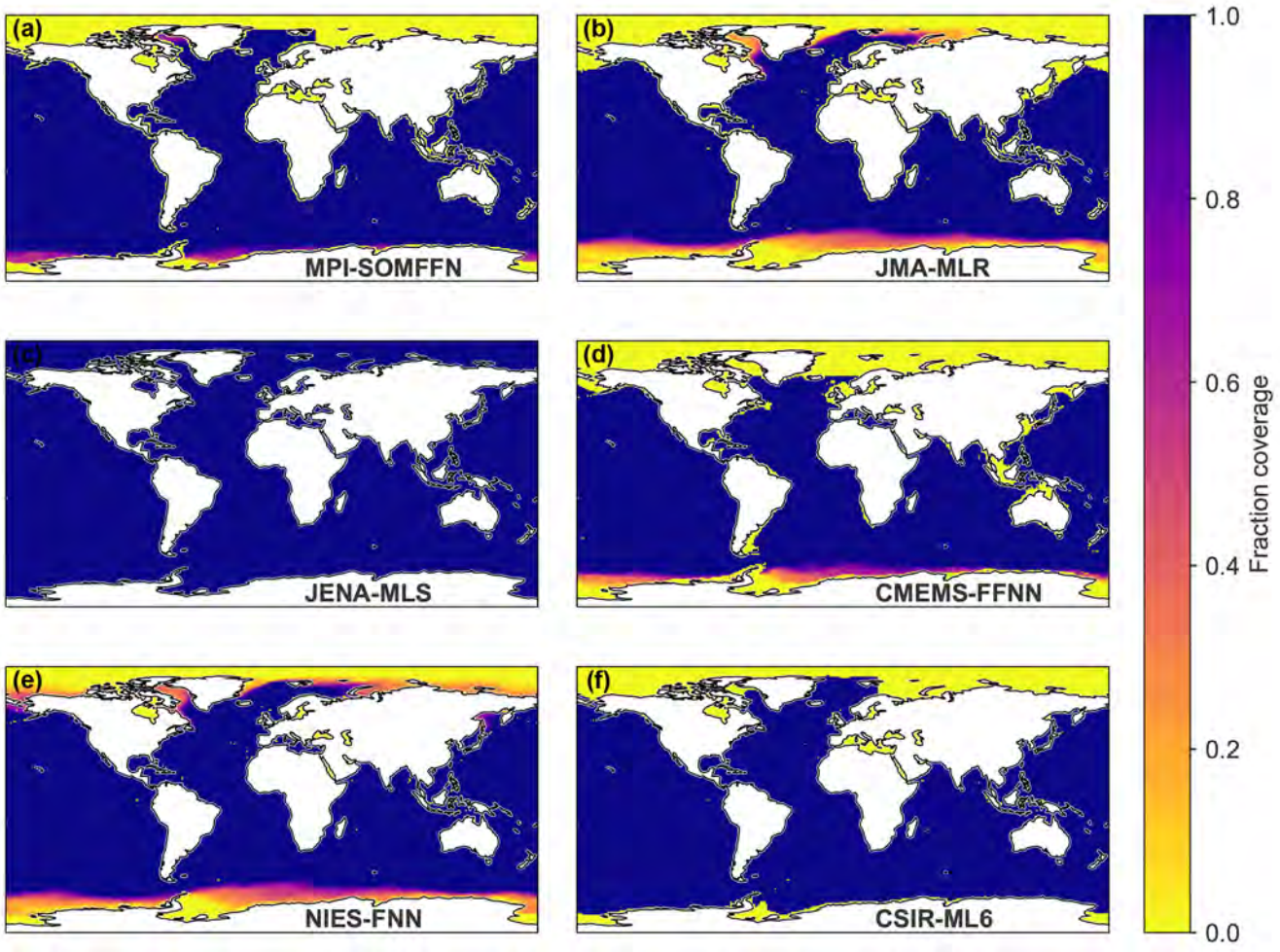

Supplementary Figure 1: Map of fraction of months from 1990 to 2019 with coverage available for each of the six observation-based pCO_2 data products. Yellow areas show regions with no reported pCO_2 values for any month of the time series. Figure from: Fay et al. (2021)

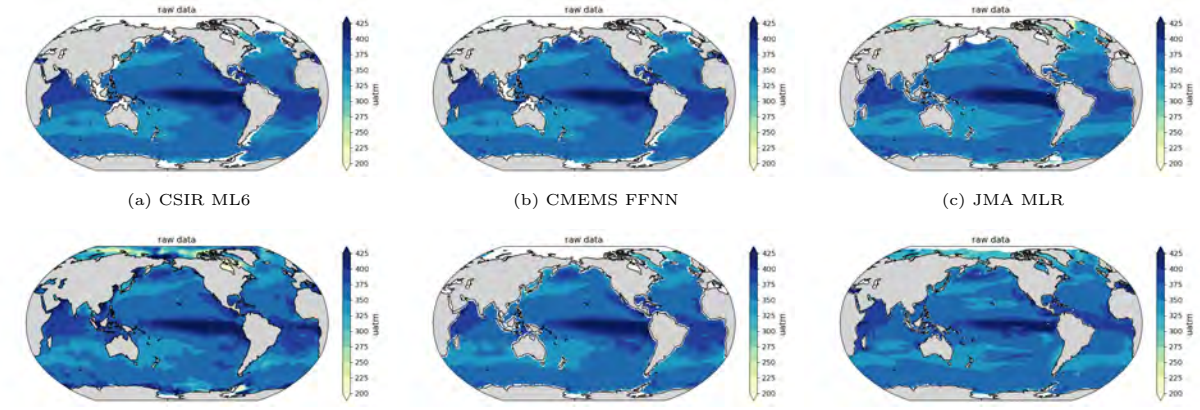

(a) CSIR ML6 (b) CMEMS FFNN (c) JMA MLR

(d) JENA MLS (e) MPI SOMFFN (f) NIES FNN

Supplementary Figure 2: The raw pCO_2 data for 1990-2019 for each of the six observation-based pCO_2 products (CSIR-ML6, CMEMS-FFNN, JMA-MLR, JENA-MLS, MPI-SOMFFN, NIES-FNN).

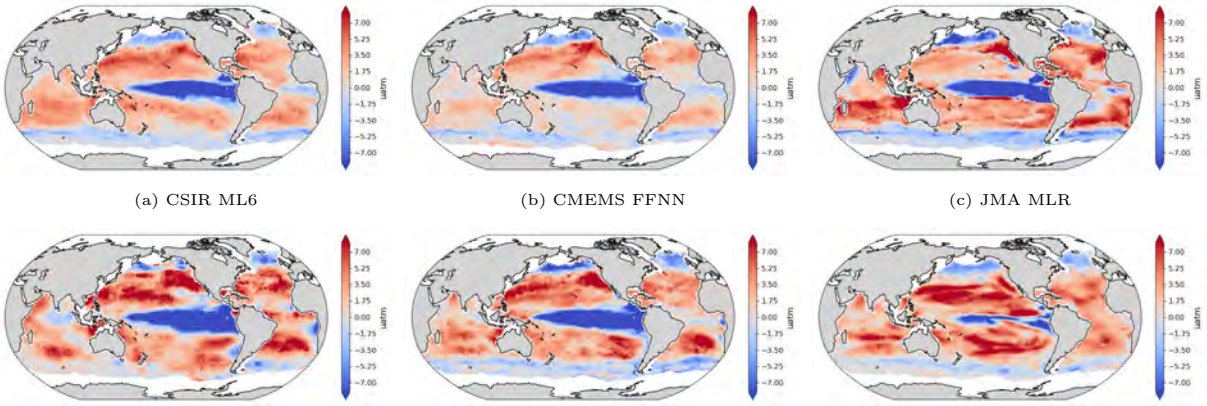

(a) CSIR ML6 (b) CMEMS FFNN (c) JMA MLR

(d) JENA MLS (e) MPI SOMFFN (f) NIES FNN

Supplementary Figure 3: The pCO_2 anomaly during MHWs (1990-2019) for each of the six observation-based pCO_2 products (CSIR-ML6, CMEMS-FFNN, JMA-MLR, JENA-MLS, MPI-SOMFFN, NIES-FNN).

(a)

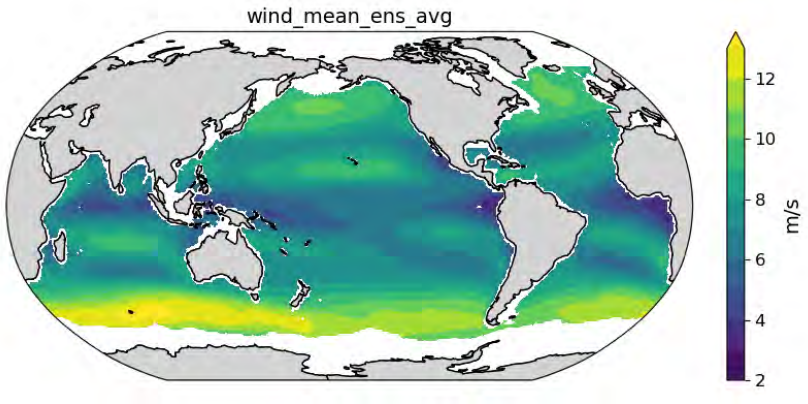

(b)

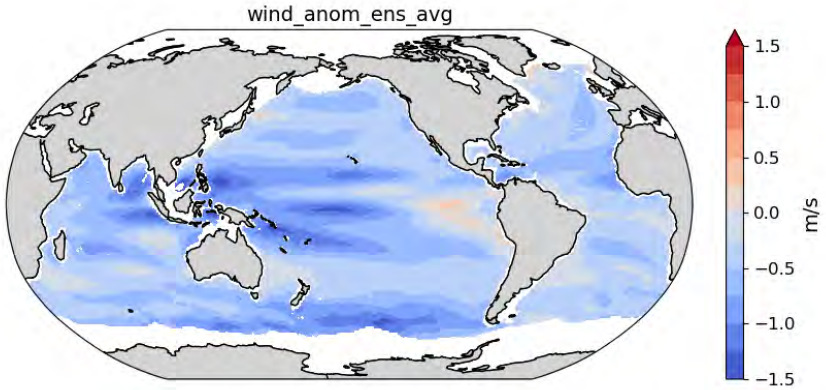

Supplementary Figure 4: Global map of ESM2M ensemble average wind speed (in m/s) at mean state and anomaly during MHWs, for 1990-2019.

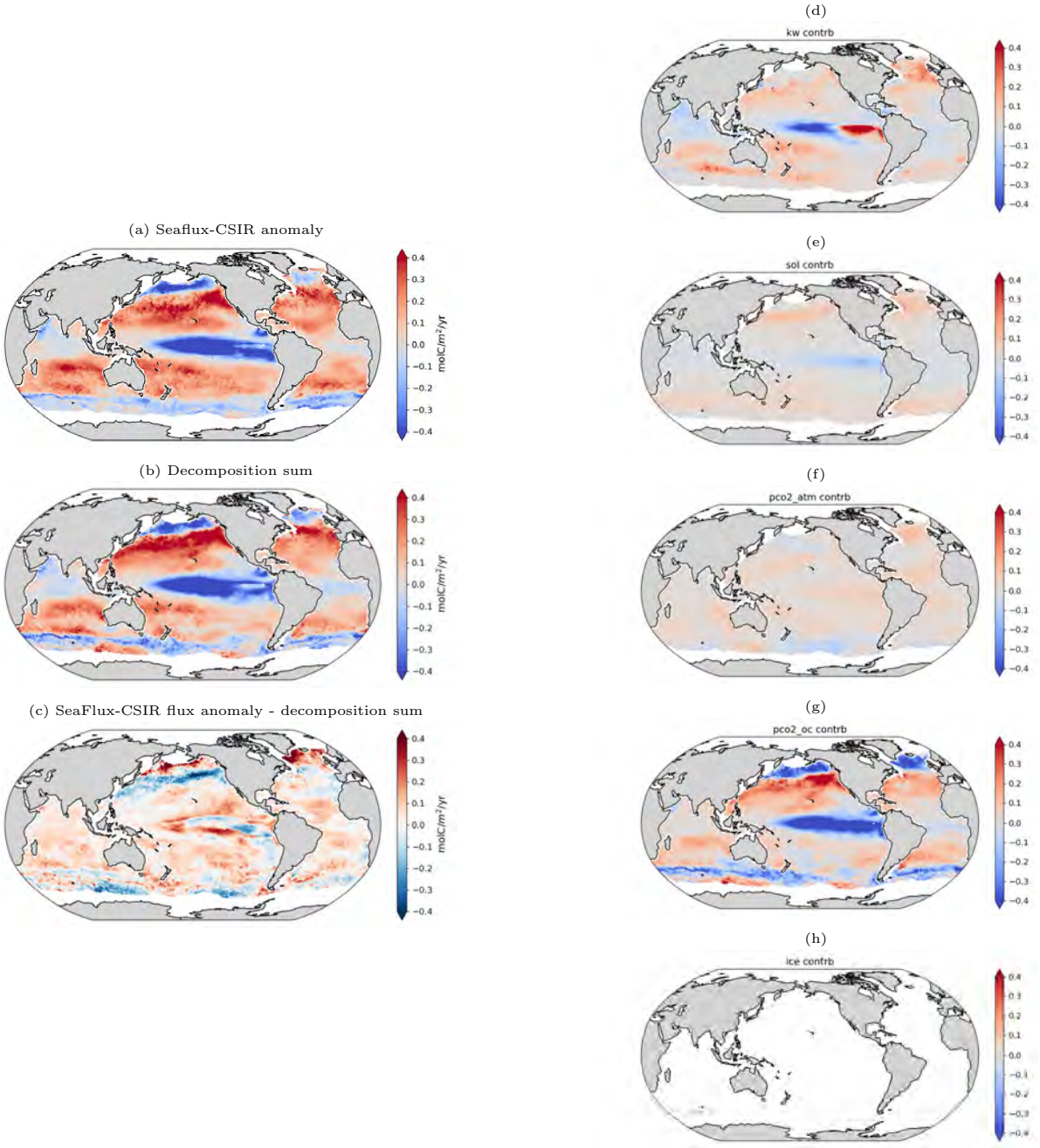

Supplementary Figure 5: Global depiction of the flux decomposition for observation-based data using the CSIR $p\mathrm{CO}_2$ product and average wind product for the time-period 1990-2019. The right hand column shows the Taylor decomposition contributions of each flux component to the overall sea-air CO2 flux anomaly during MHWs (k_w, solubility, $pCO_{2_{\mathrm{atm}}}$, $pCO_{2_{\mathrm{oc}}}$, ice. The left column shows the SeaFlux sea-air CO_2 flux anomaly during MHWs (a), the sum of the flux decomposition contributions (b), and the difference between the two (a - b). The data is masked to include only the regions where all six products have data.

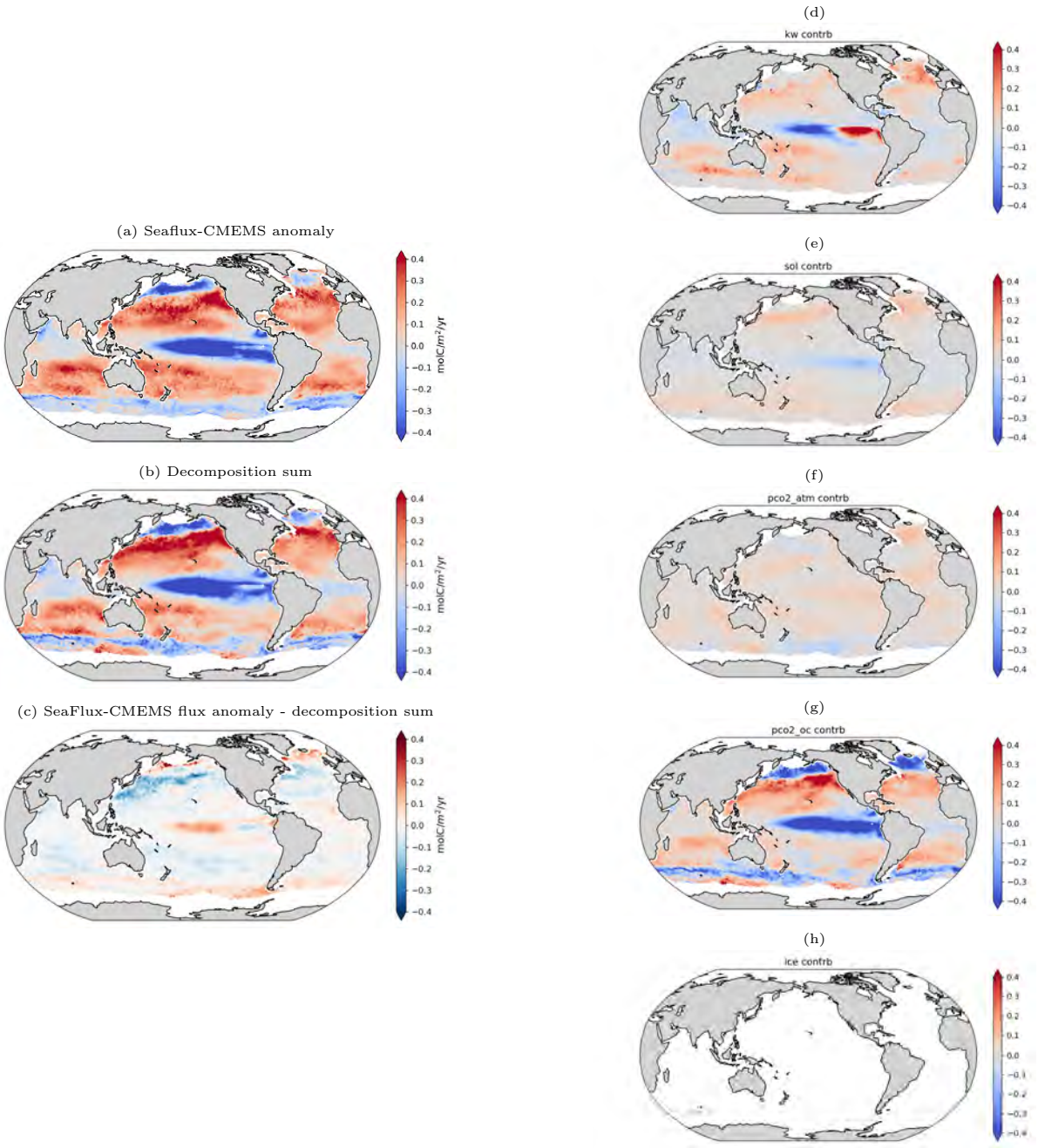

Supplementary Figure 6: Global depiction of the flux decomposition for observation-based data using the CMEMS pCO_2 product and average wind product for the time-period 1990-2019. The right hand column shows the Taylor decomposition contributions of each flux component to the overall sea-air CO2 flux anomaly during MHWs (k_w, solubility, $pCO_{2_{\mathrm{atm}}}$, $pCO_{2_{\mathrm{oc}}}$, ice. The left column shows the SeaFlux sea-air CO_2 flux anomaly during MHWs (a), the sum of the flux decomposition contributions (b), and the difference between the two (a - b). The data is masked to include only the regions where all six products have data.

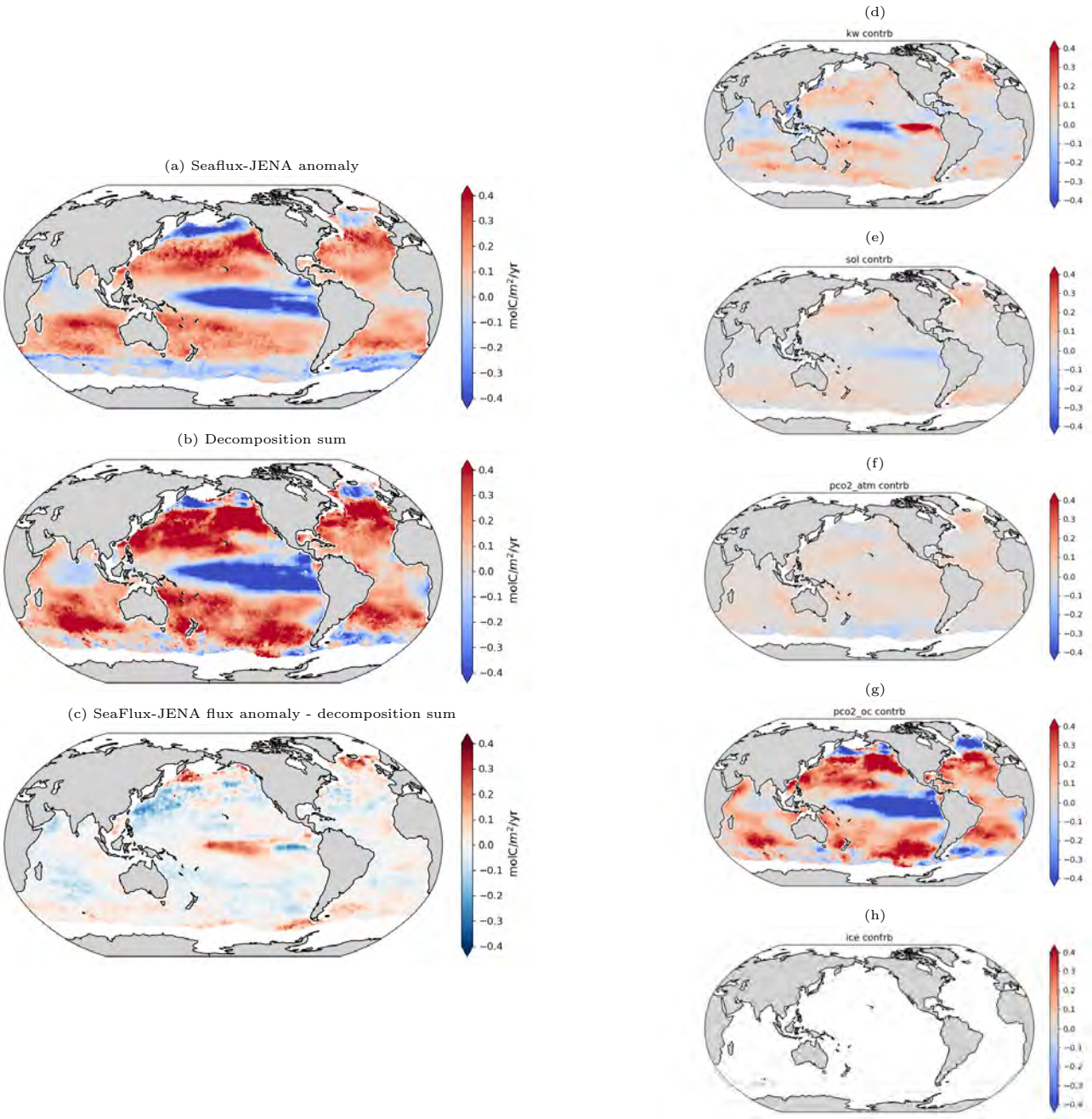

Supplementary Figure 7: Global depiction of the flux decomposition for observation-based data using the JENA $p\mathrm{CO}_2$ product and average wind product for the time-period 1990-2019. The right hand column shows the Taylor decomposition contributions of each flux component to the overall sea-air CO2 flux anomaly during MHWs (k_w, solubility, $pCO_{2_{\mathrm{atm}}}$, $pCO_{2_{\mathrm{oc}}}$, ice. The left column shows the SeaFlux sea-air CO_2 flux anomaly during MHWs (a), the sum of the flux decomposition contributions (b), and the difference between the two (a - b). The data is masked to include only the regions where all six products have data.

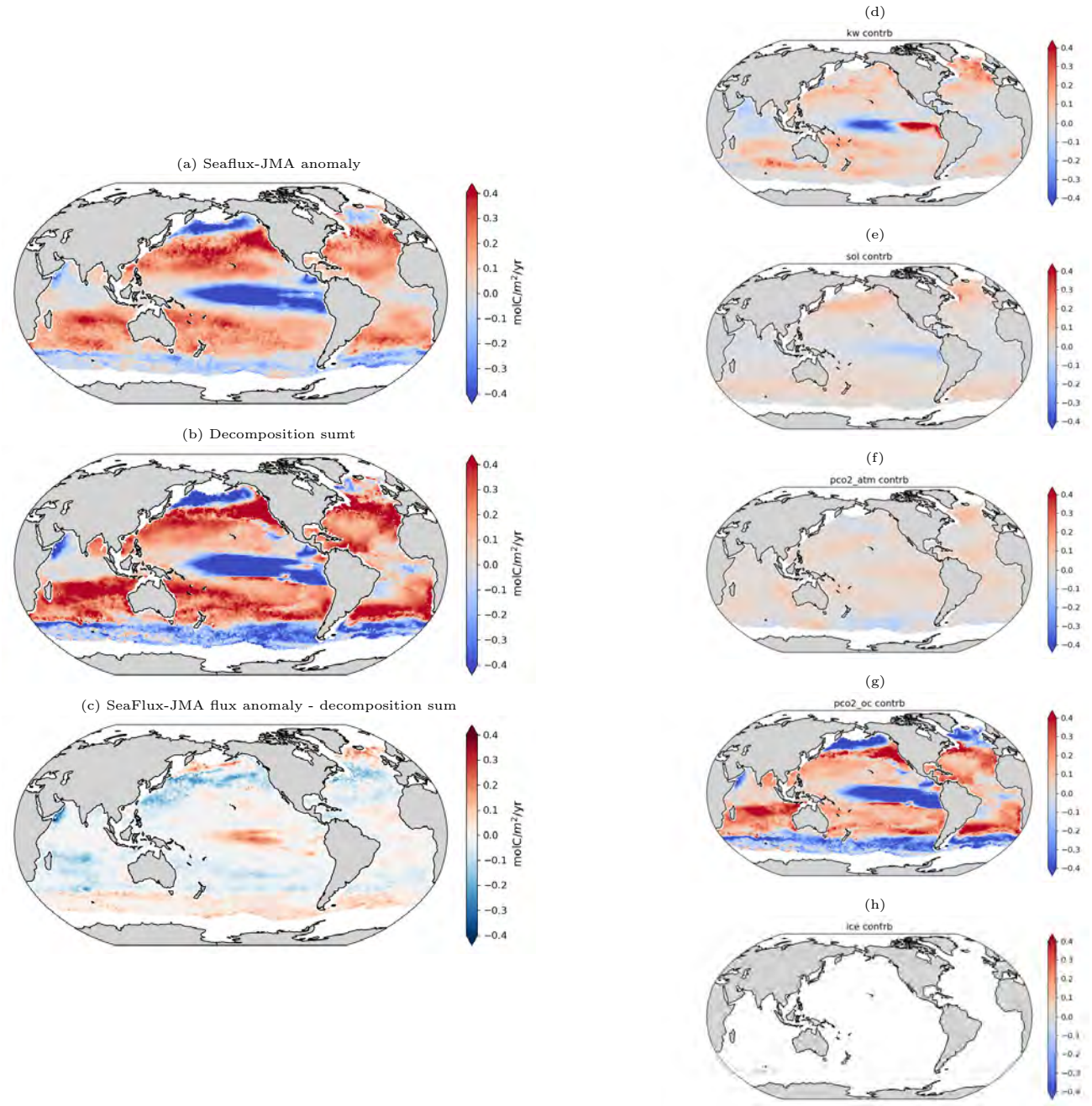

Supplementary Figure 8: Global depiction of the flux decomposition for observation-based data using the JMA pCO_2 product and average wind product for the time-period 1990-2019. The right hand column shows the Taylor decomposition contributions of each flux component to the overall sea-air CO2 flux anomaly during MHWs (k_w, solubility, $pCO_{2_{\mathrm{atm}}}$, $pCO_{2_{\mathrm{oc}}}$, ice. The left column shows the SeaFlux sea-air CO_2 flux anomaly during MHWs (a), the sum of the flux decomposition contributions (b), and the difference between the two (a - b). The data is masked to include only the regions where all six products have data.

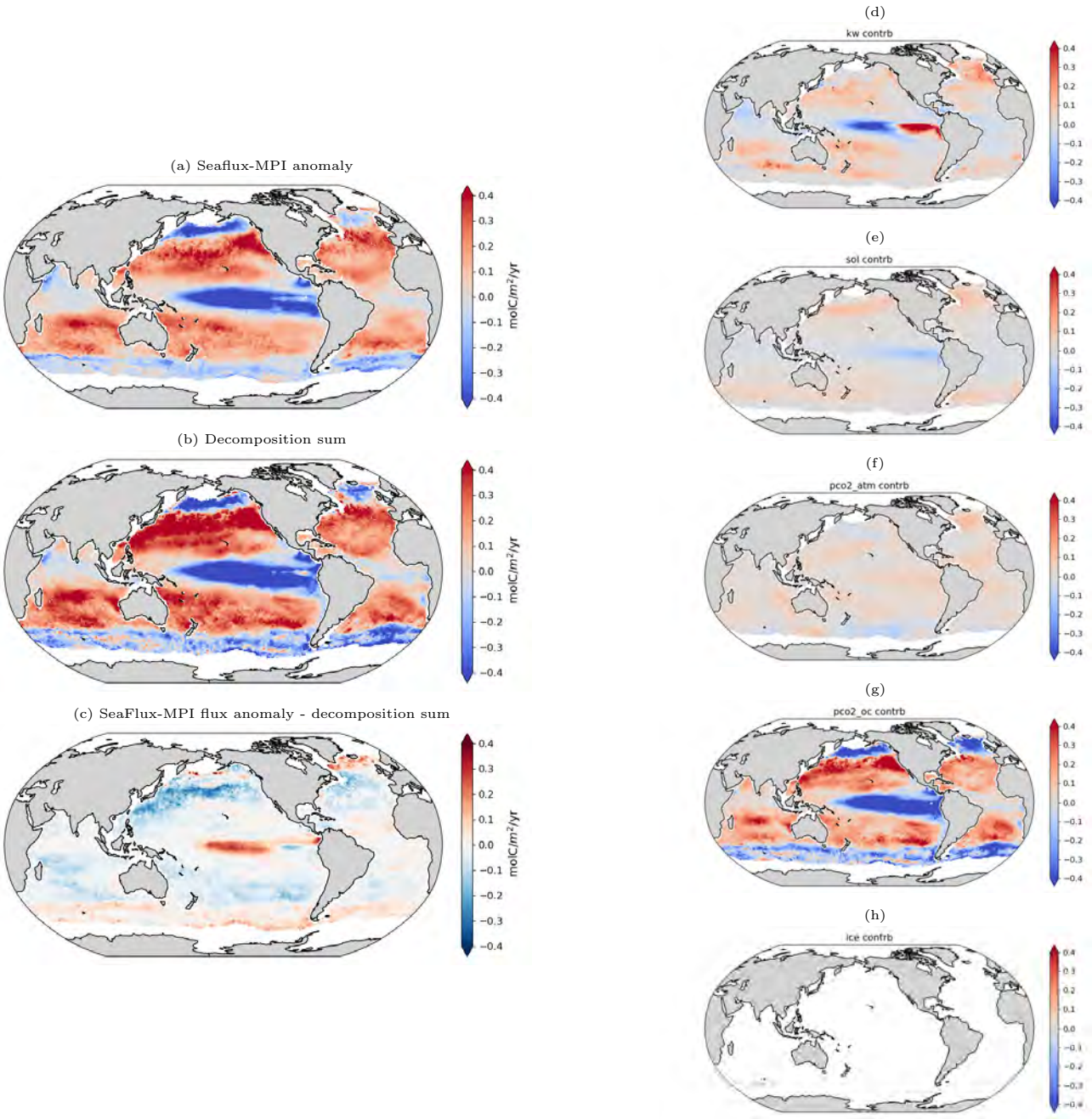

Supplementary Figure 9: Global depiction of the flux decomposition for observation-based data using the MPI pCO_2 product and average wind product for the time-period 1990-2019. The right hand column shows the Taylor decomposition contributions of each flux component to the overall sea-air CO2 flux anomaly during MHWs (k_w, solubility, $pCO_{2_{\mathrm{atm}}}$, $pCO_{2_{\mathrm{oc}}}$, ice. The left column shows the SeaFlux sea-air CO_2 flux anomaly during MHWs (a), the sum of the flux decomposition contributions (b), and the difference between the two (a - b). The data is masked to include only the regions where all six products have data.

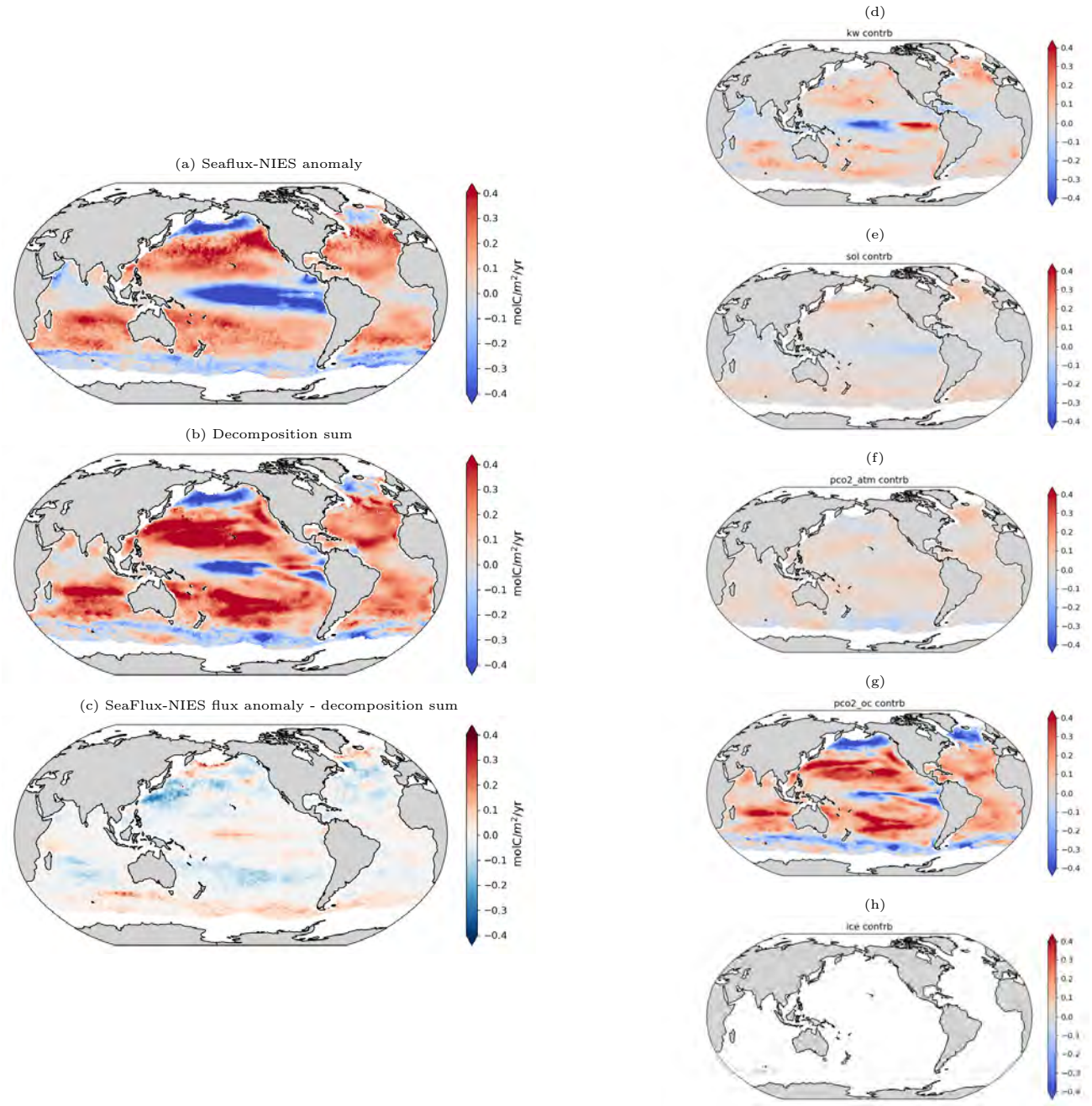

Supplementary Figure 10: Global depiction of the flux decomposition for observation-based data using the NIES pCO_2 product and average wind product for the time-period 1990-2019. The right hand column shows the Taylor decomposition contributions of each flux component to the overall sea-air CO2 flux anomaly during MHWs (k_w, solubility, $pCO_{2_{\mathrm{atm}}}$, $pCO_{2_{\mathrm{oc}}}$, ice. The left column shows the SeaFlux sea-air CO_2 flux anomaly during MHWs (a), the sum of the flux decomposition contributions (b), and the difference between the two (a - b). The data is masked to include only the regions where all six products have data.

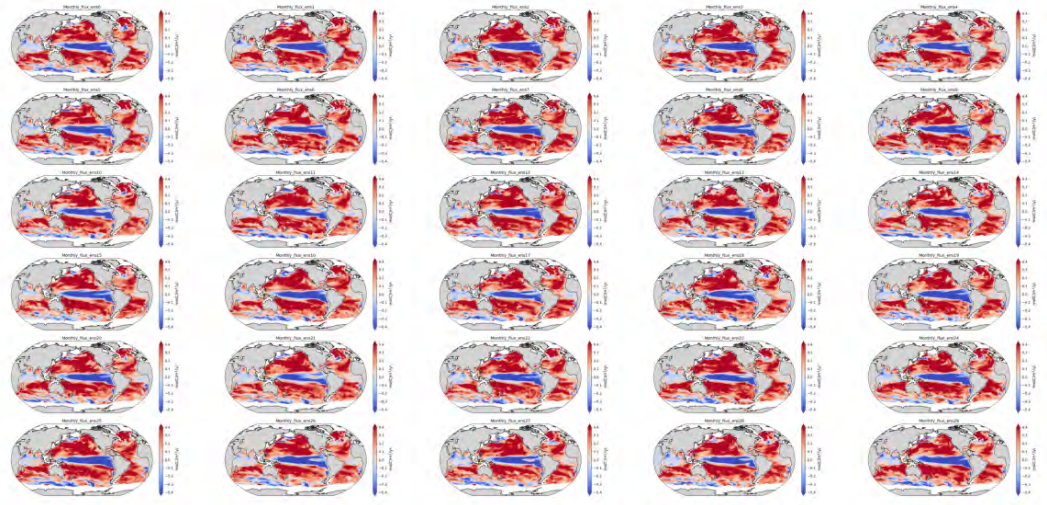

(a)

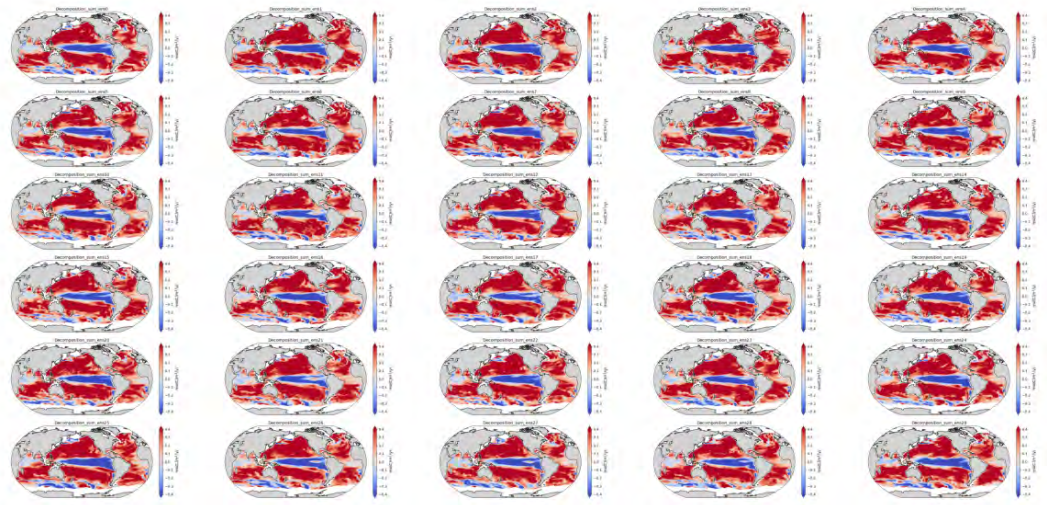

(b)

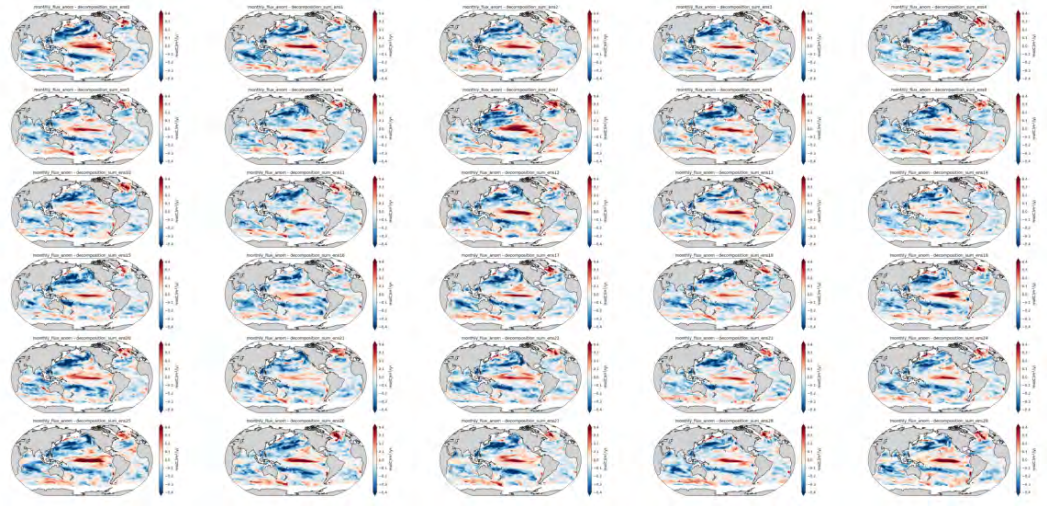

(c)

Supplementary Figure 11: For each ESM2M ensemble member the flux decomposition results: (a) the recalculated monthly flux anomaly during MHWs, (b) the sum of the flux decomposition contributions, and (c) and the difference between the two.

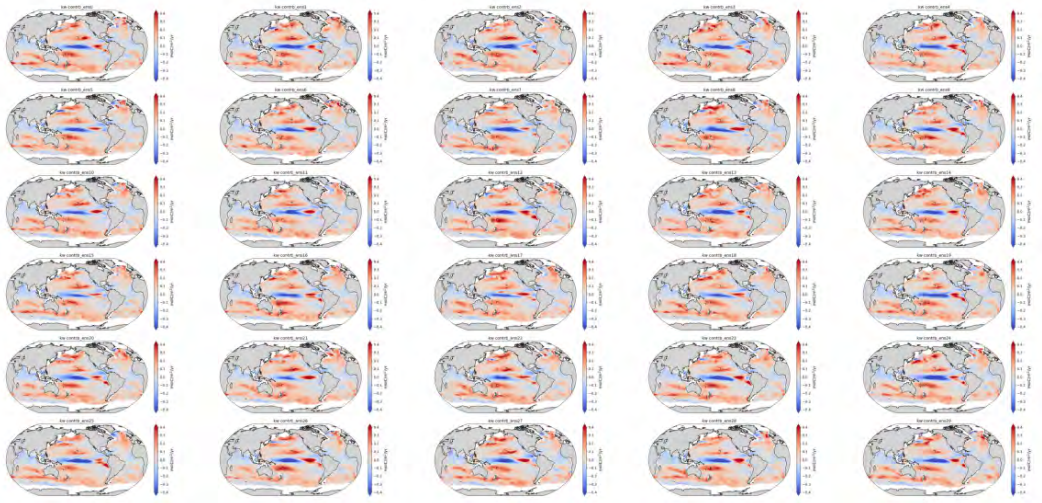

(a)

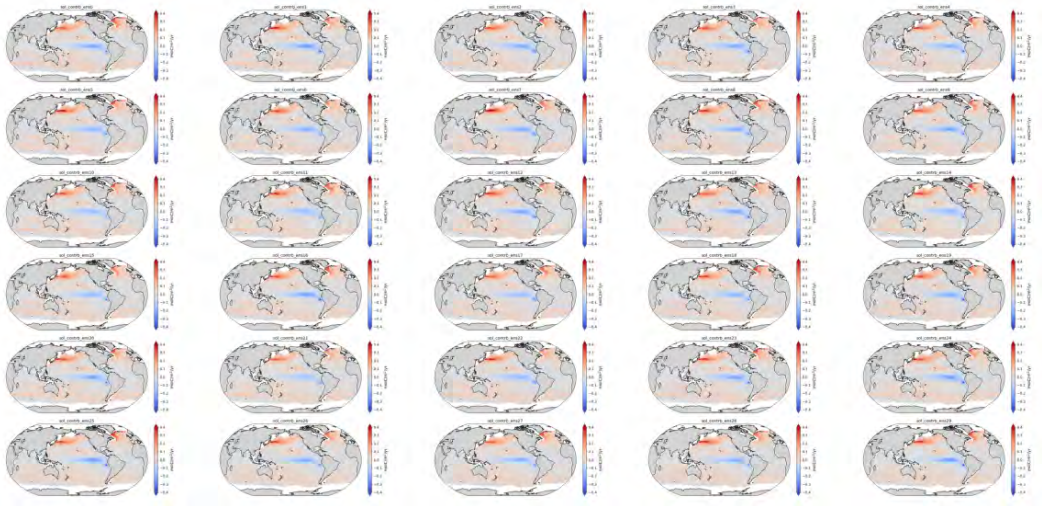

(b)

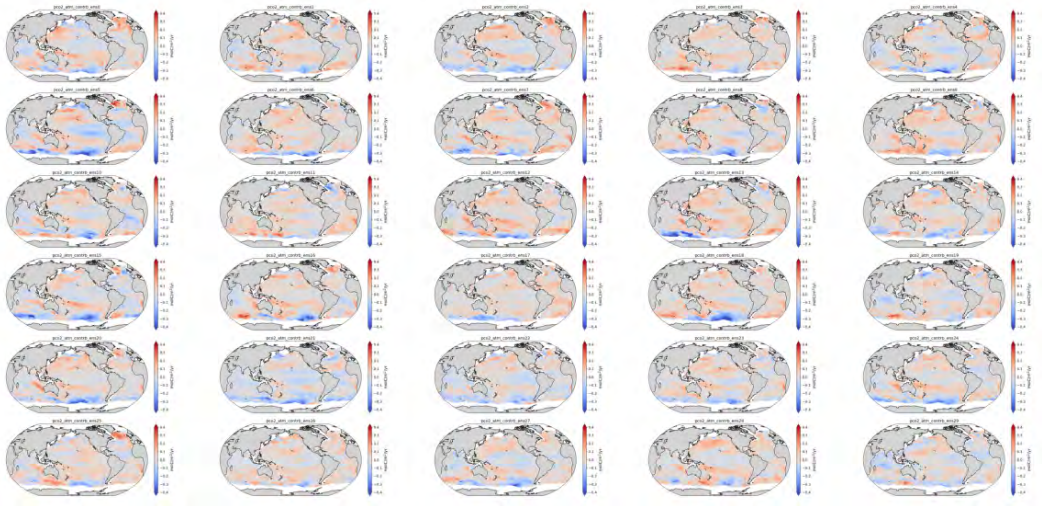

(c)

Supplementary Figure 12: For each ESM2M ensemble member the contribution of the gas transfer velocity (a), solubility (b), and atmospheric pCO_2 (c) to flux anomalies during MHWs.

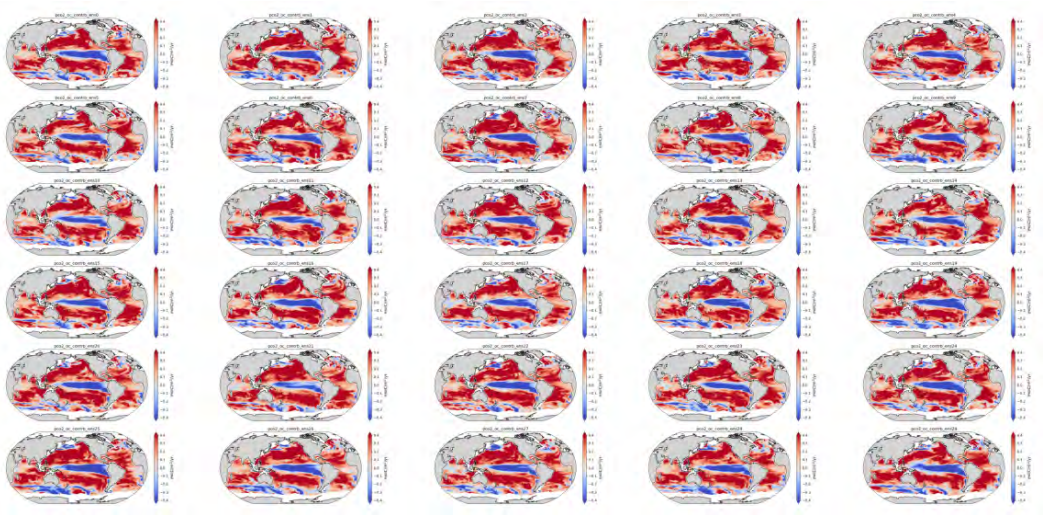

(d)

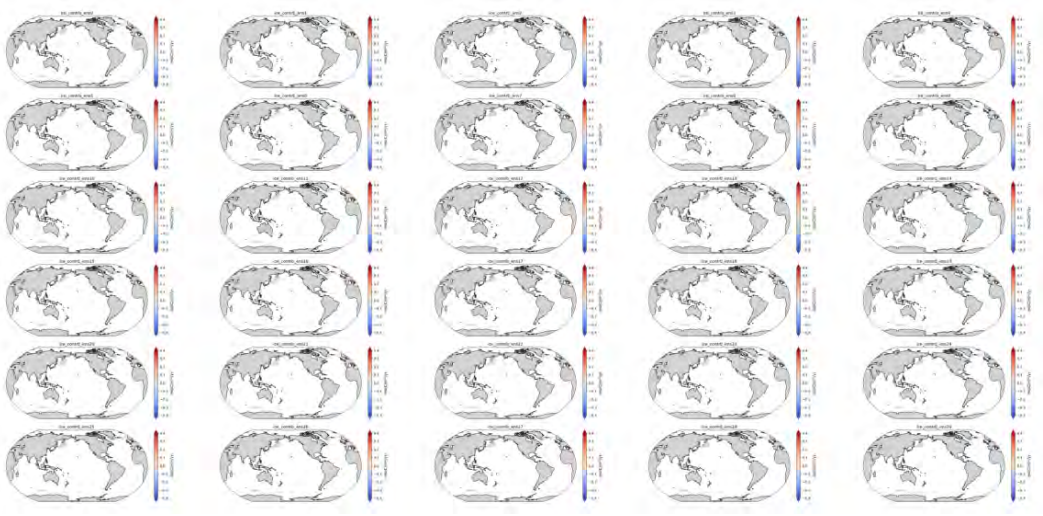

(e)

The contribution of oceanic pCO_2 (d) and ice (e) to flux anomalies during MHWs.

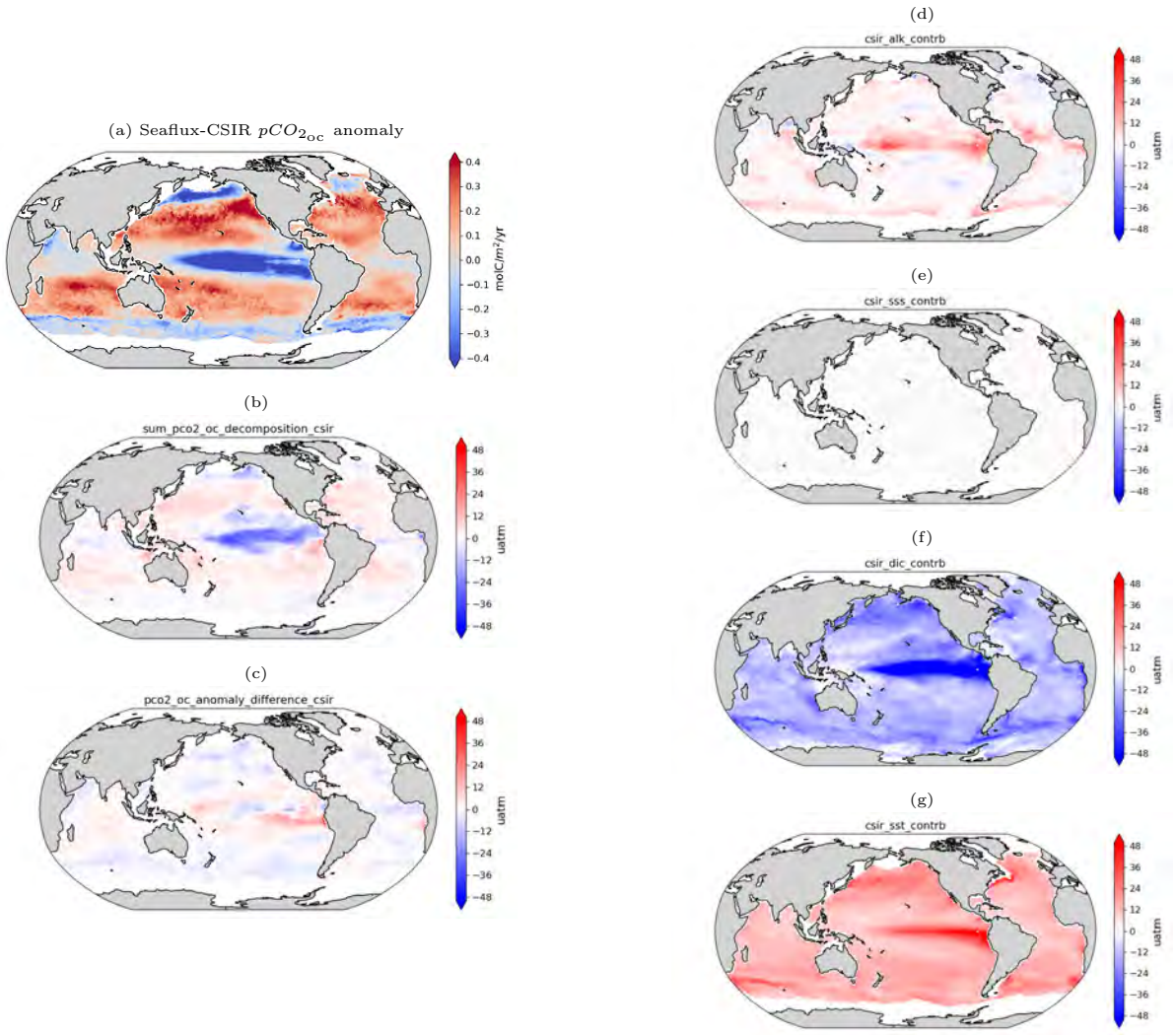

Supplementary Figure 13: Global maps of the oceanic $p\mathrm{CO}_2$ decomposition for observation-based data using the CSIR DIC product for the time-period 1990-2019. The right hand column shows the Taylor decomposition contributions of each $p\mathrm{CO}_2$ component to the overall $pCO_{2_{oc}}$ anomaly during MHWs (alkalinity, salinity, dissolved inorganic carbon, and sea surface temperature). The left column shows SeaFlux-CSIR $p\mathrm{CO}_2$ flux anomaly during MHWs (a), the sum of the $pCO_{2_{oc}}$ decomposition contributions (b), and the difference between the two (a - b).

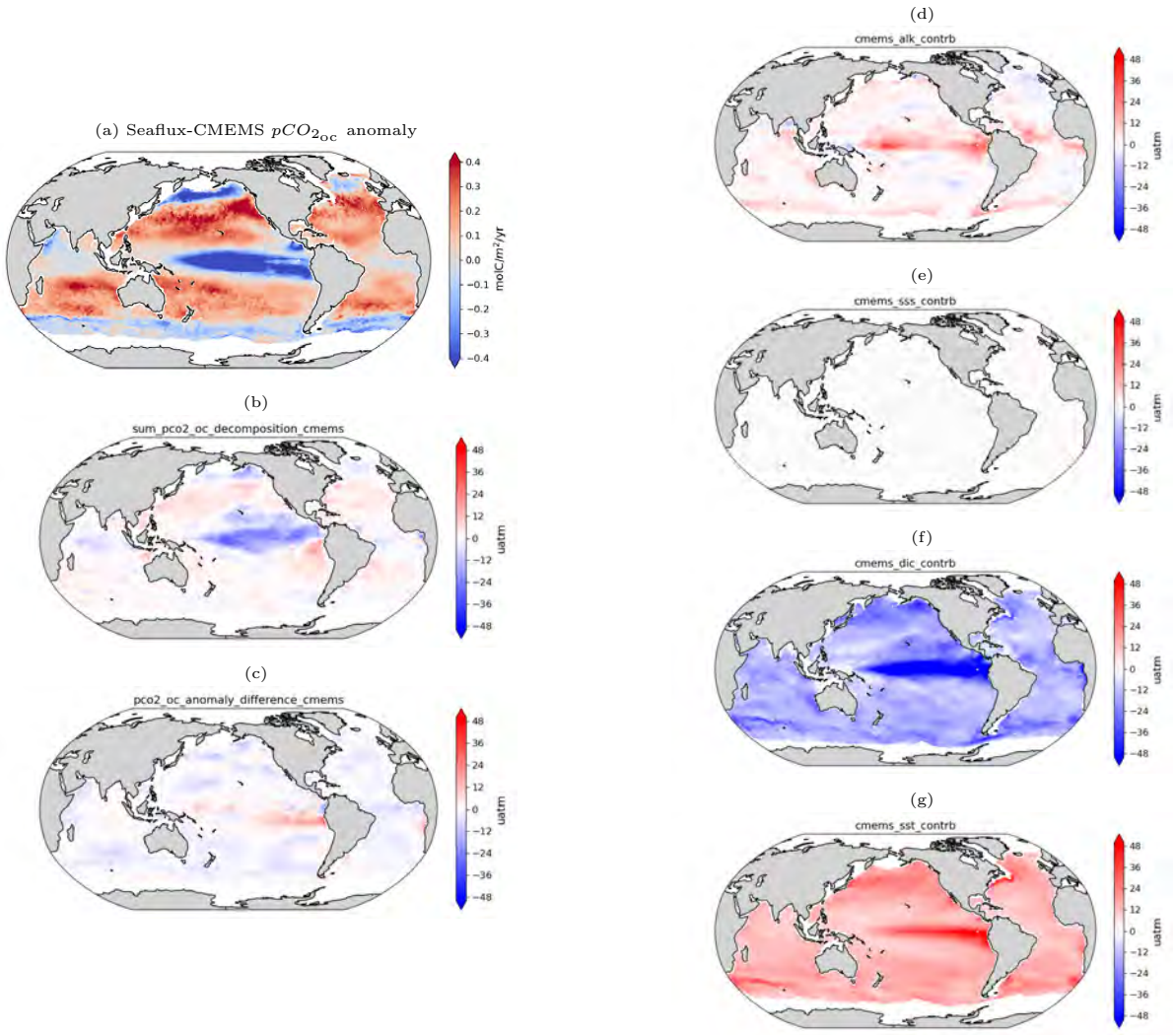

Supplementary Figure 14: Global maps of the oceanic $p\mathrm{CO}_2$ decomposition for observation-based data using the CMEMS DIC product for the time-period 1990-2019. The right hand column shows the Taylor decomposition contributions of each $p\mathrm{CO}_2$ component to the overall $pCO_{2_{oc}}$ anomaly during MHWs (alkalinity, salinity, dissolved inorganic carbon, and sea surface temperature). The left column shows SeaFlux-cmems $p\mathrm{CO}_2$ flux anomaly during MHWs (a), the sum of the $pCO_{2_{oc}}$ decomposition contributions (b), and the difference between the two (a - b).

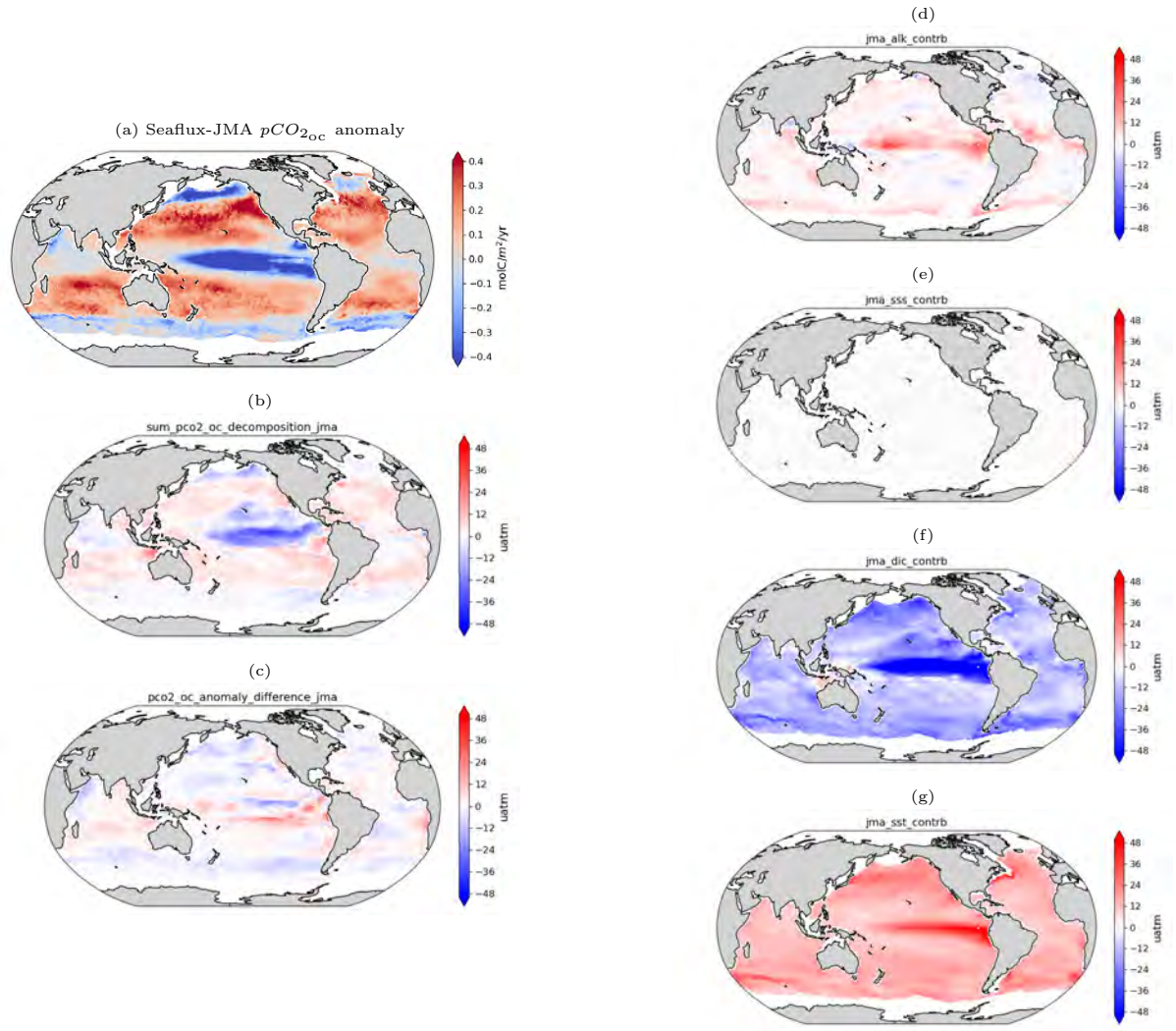

Supplementary Figure 15: Global maps of the oceanic $p\mathrm{CO}_2$ decomposition for observation-based data using the JMA DIC product for the time-period 1990-2019. The right hand column shows the Taylor decomposition contributions of each $p\mathrm{CO}_2$ component to the overall $pCO_{2_{oc}}$ anomaly during MHWs (alkalinity, salinity, dissolved inorganic carbon, and sea surface temperature). The left column shows SeaFlux-jma $p\mathrm{CO}_2$ flux anomaly during MHWs (a), the sum of the $pCO_{2_{oc}}$ decomposition contributions (b), and the difference between the two (a - b).

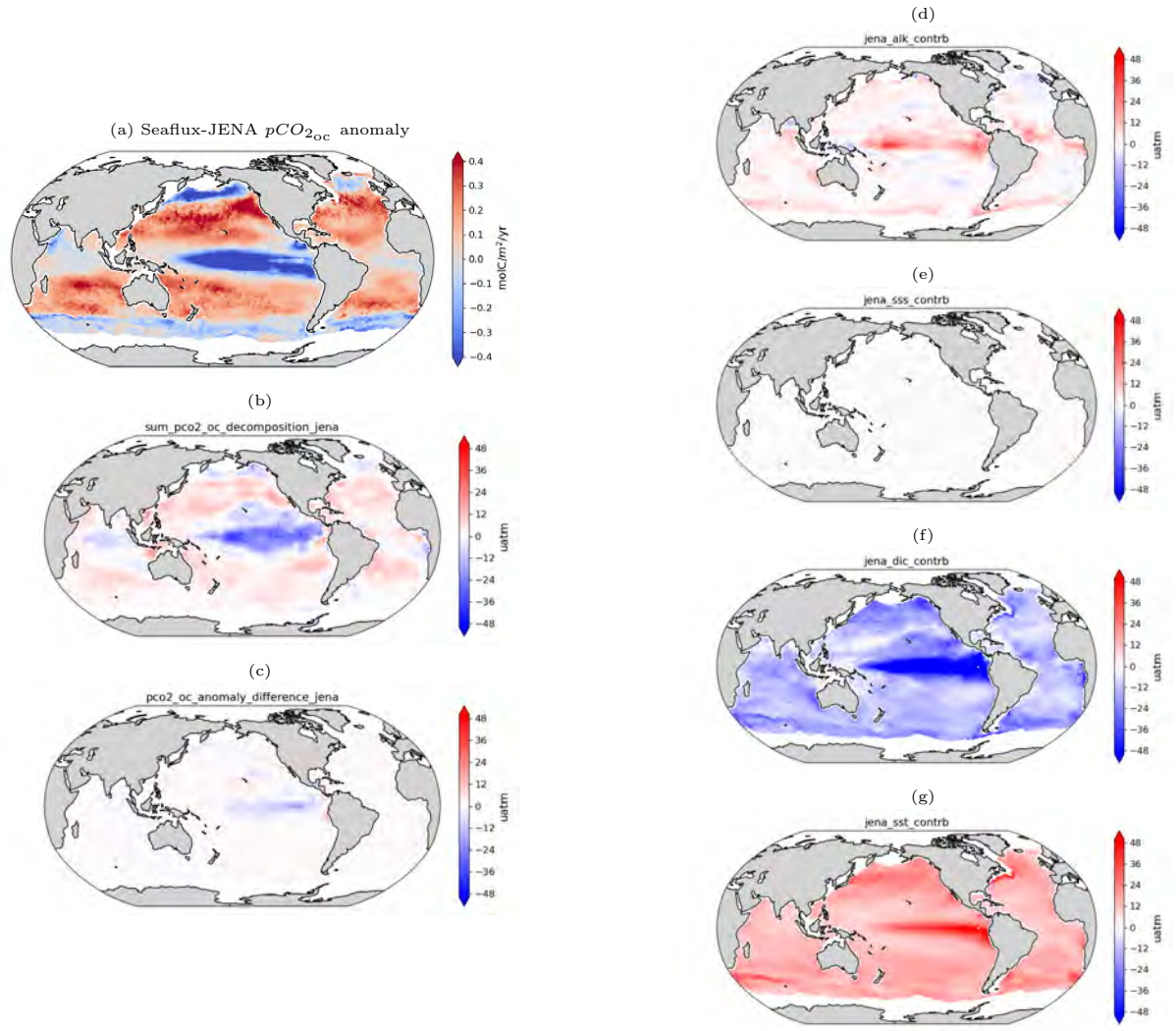

Supplementary Figure 16: Global maps of the oceanic $p\mathrm{CO}_2$ decomposition for observation-based data using the JENA DIC product for the time-period 1990-2019. The right hand column shows the Taylor decomposition contributions of each $p\mathrm{CO}_2$ component to the overall $pCO_{2_{oc}}$ anomaly during MHWs (alkalinity, salinity, dissolved inorganic carbon, and sea surface temperature). The left column shows SeaFlux-jena $p\mathrm{CO}_2$ flux anomaly during MHWs (a), the sum of the $pCO_{2_{oc}}$ decomposition contributions (b), and the difference between the two (a - b).

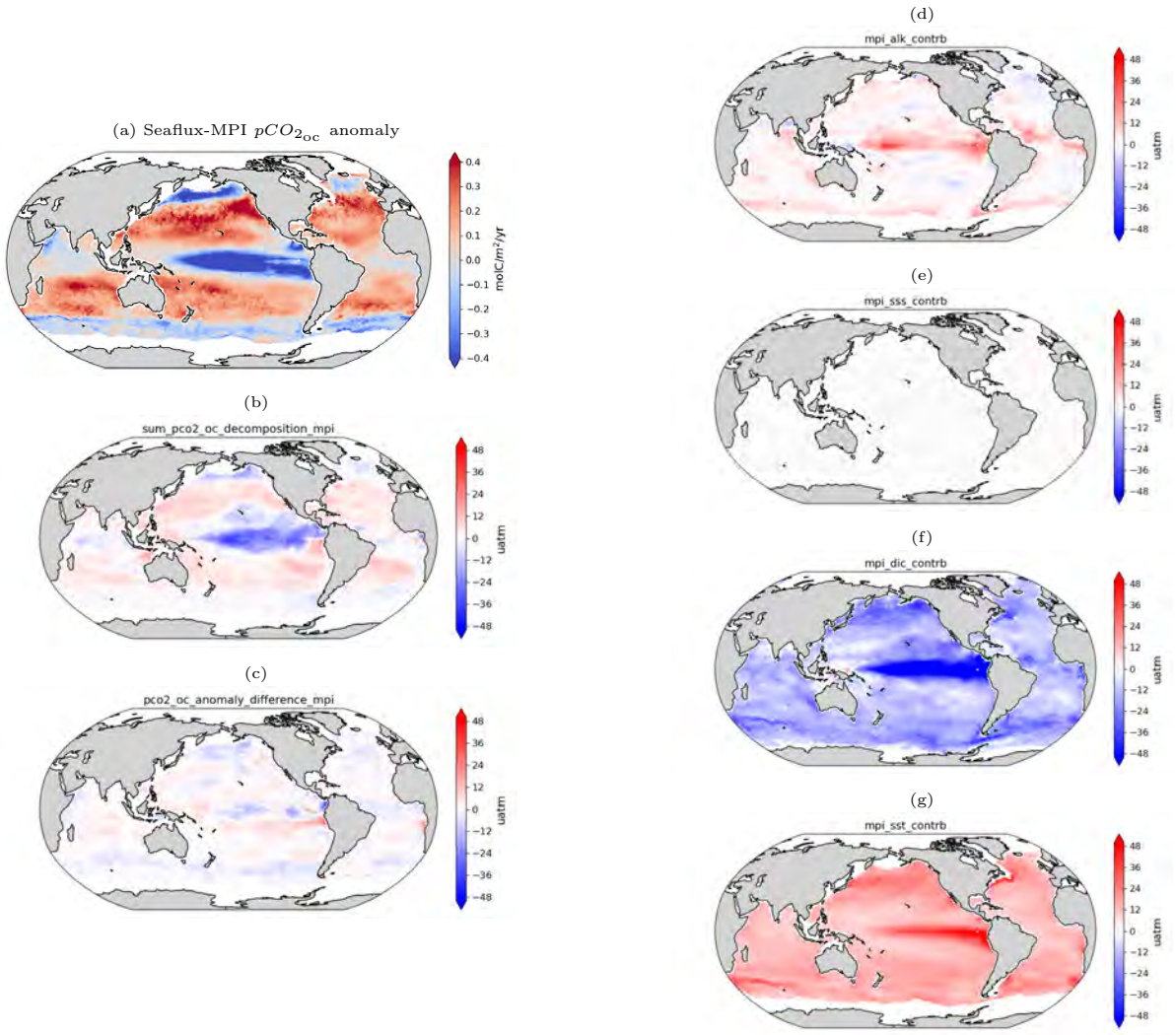

Supplementary Figure 17: Global maps of the oceanic $p\mathrm{CO}_2$ decomposition for observation-based data using the MPI DIC product for the time-period 1990-2019. The right hand column shows the Taylor decomposition contributions of each $p\mathrm{CO}_2$ component to the overall $pCO_{2_{oc}}$ anomaly during MHWs (alkalinity, salinity, dissolved inorganic carbon, and sea surface temperature). The left column shows SeaFlux-mpi $p\mathrm{CO}_2$ flux anomaly during MHWs (a), the sum of the $pCO_{2_{oc}}$ decomposition contributions (b), and the difference between the two (a - b).

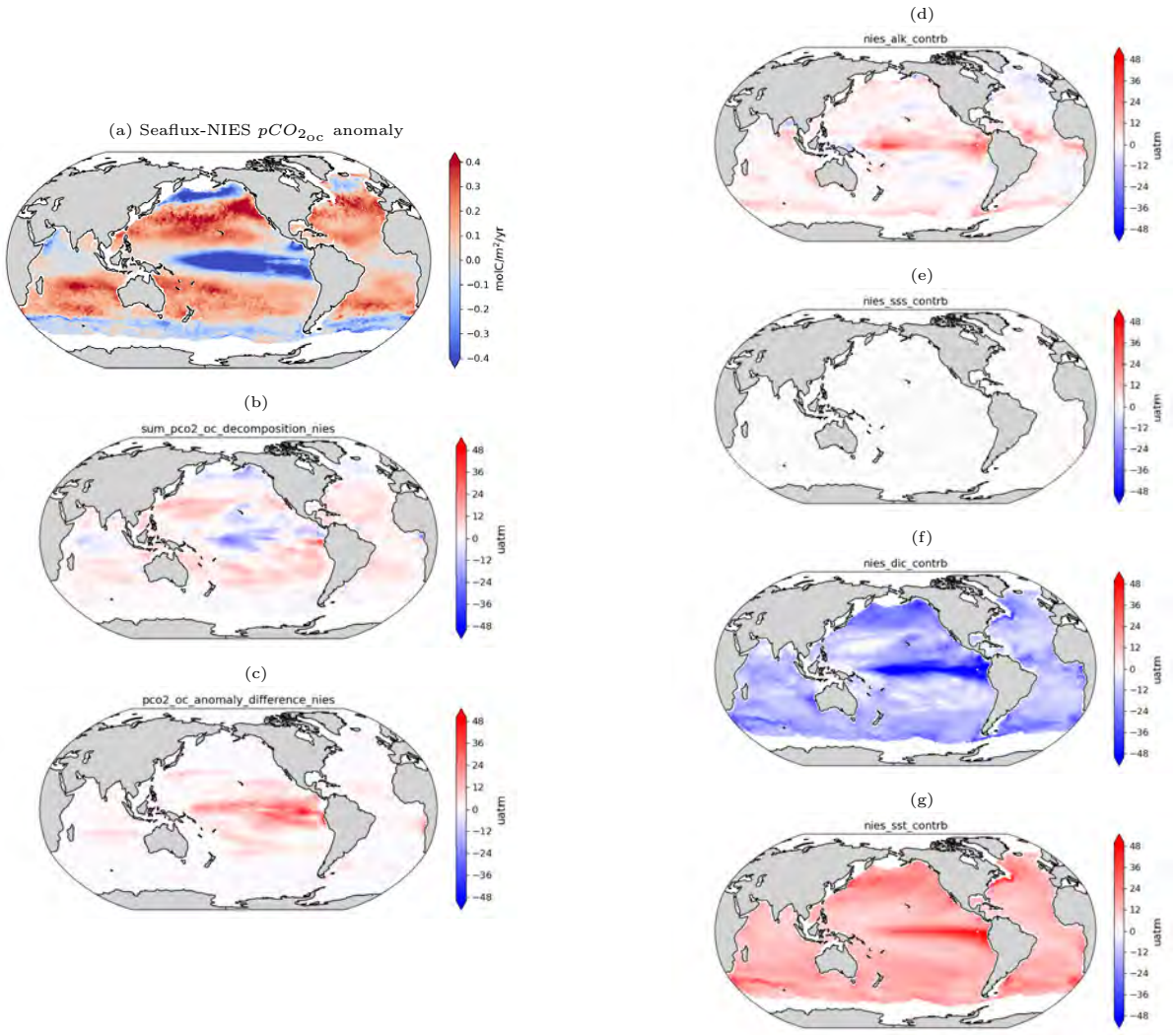

Supplementary Figure 18: Global maps of the oceanic $p\mathrm{CO}_2$ decomposition for observation-based data using the NIES DIC product for the time-period 1990-2019. The right hand column shows the Taylor decomposition contributions of each $p\mathrm{CO}_2$ component to the overall $pCO_{2_{oc}}$ anomaly during MHWs (alkalinity, salinity, dissolved inorganic carbon, and sea surface temperature). The left column shows SeaFlux-nies $p\mathrm{CO}_2$ flux anomaly during MHWs (a), the sum of the $pCO_{2_{oc}}$ decomposition contributions (b), and the difference between the two (a - b).

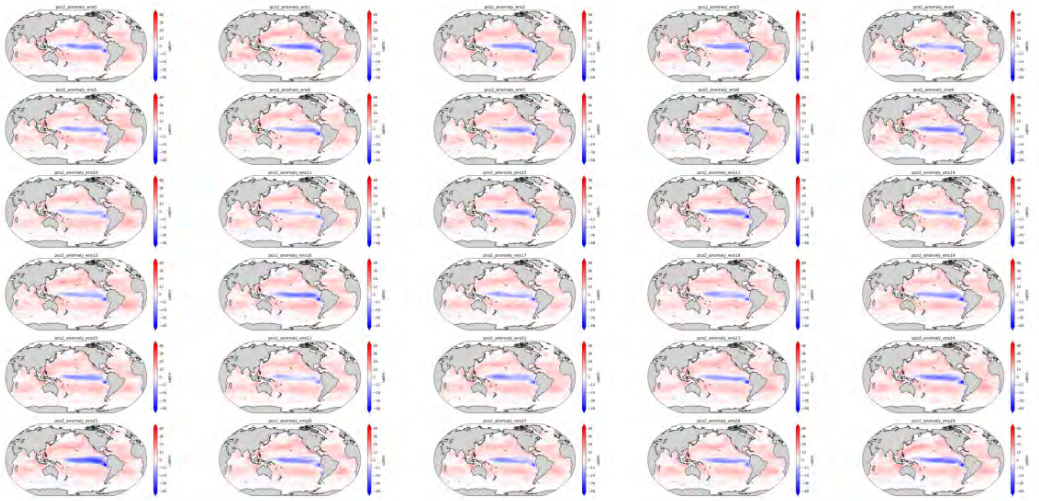

(a)

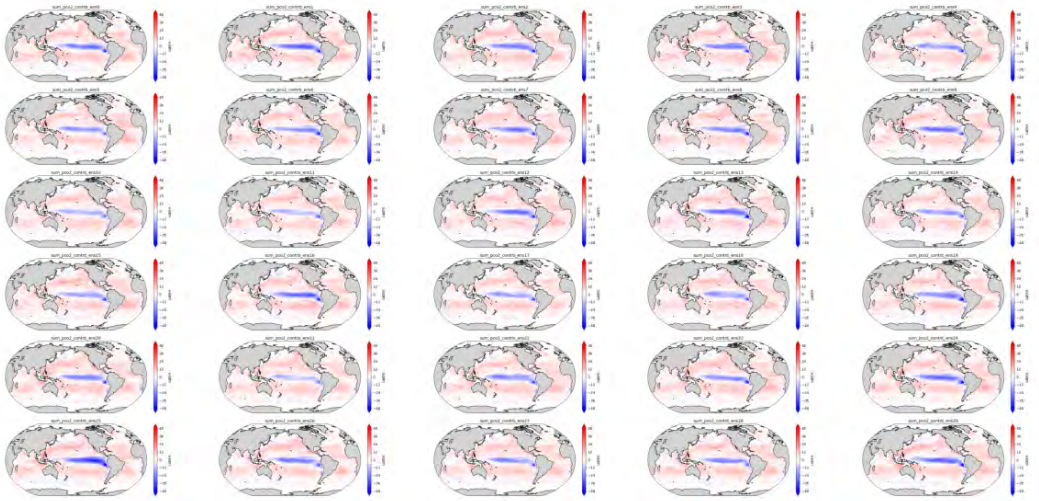

(b)

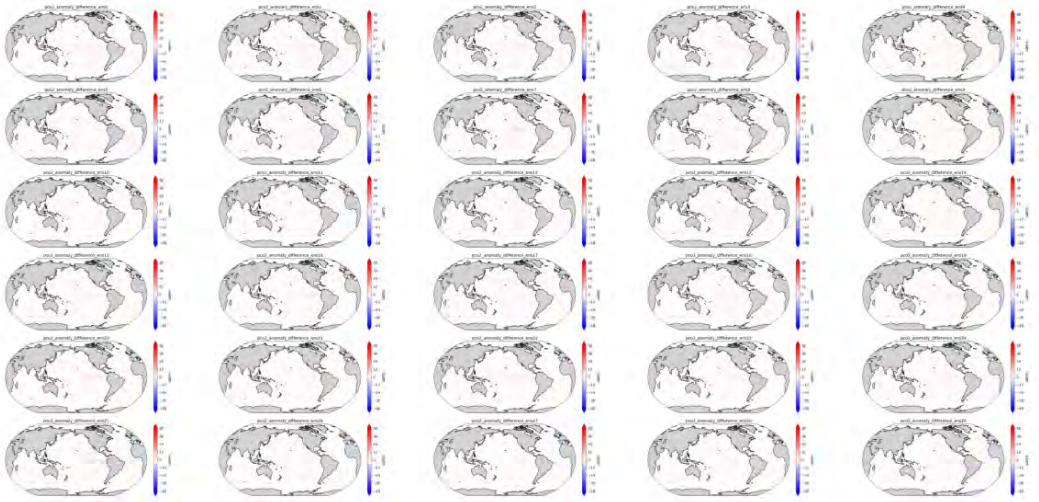

(c)

Supplementary Figure 19: For each ESM2M ensemble member the ocean pco2 decomposition results: (a) the pCO_2 anomaly, (b) sum of pCO_2 decomposition terms, and (c) the difference between the anomaly and decomposition sum.

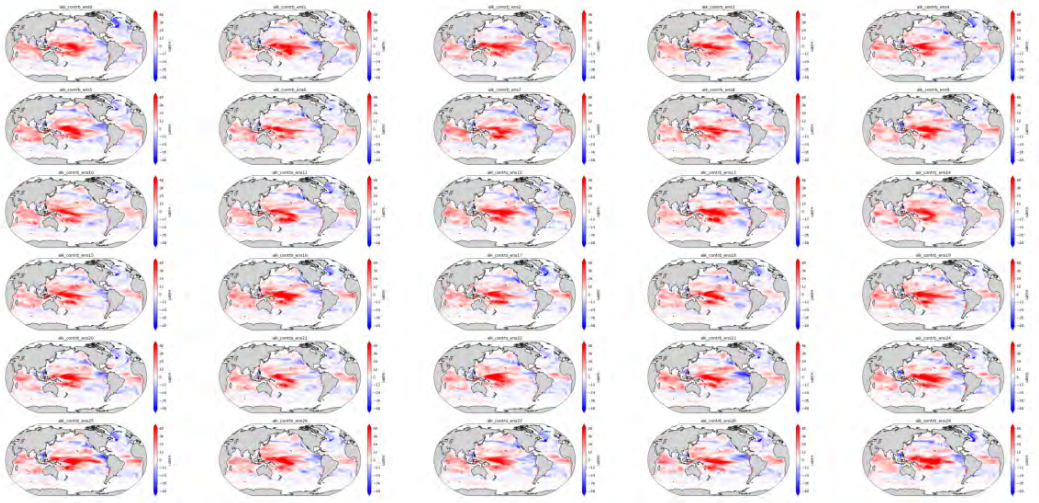

(a)

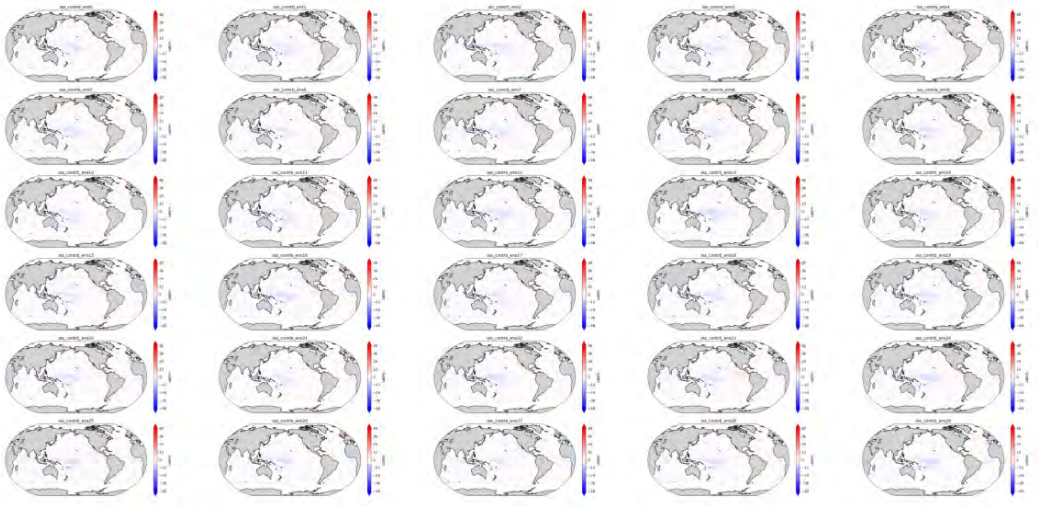

(b)

Supplementary Figure 20: For each ESM2M ensemble member the contribution of alkalinity (a), salinity (b) on oceanic pCO_2 anomalies during MHWs.

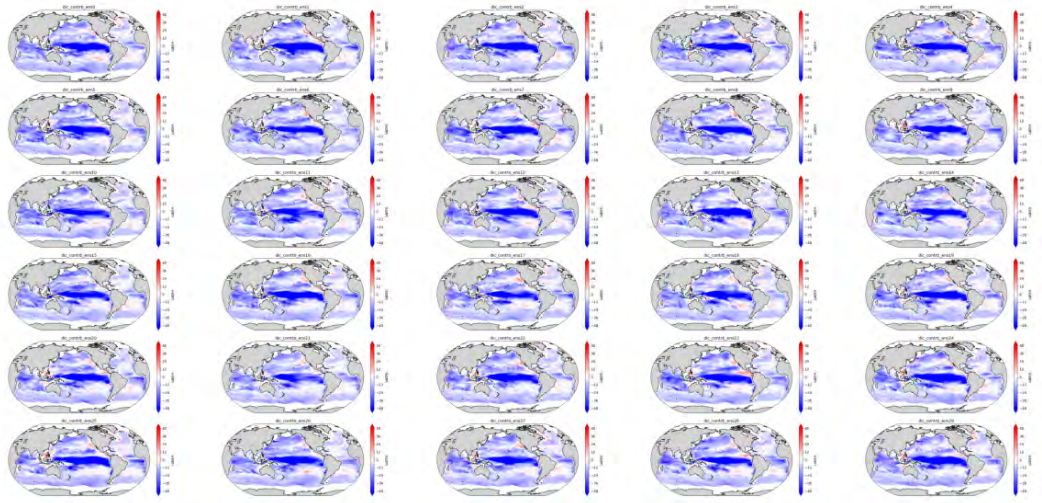

(c)

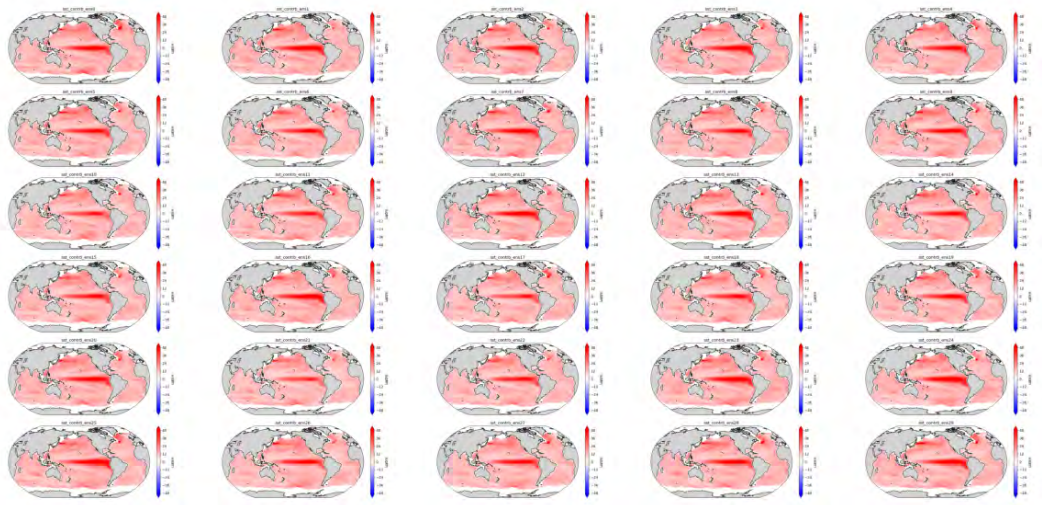

(d)

The contribution of dissolved inorganic carbon (c), and sea surface temperature (d) on oceanic pCO_2 anomalies during MHWs.

References

Anderson, J. L., V. Balaji, a. A. B., Cooke, W., Delworth, T., Dixon, K., Donner, L., Dunne, K., Freidenreich, S., Garner, S., Gudgel, R., Gordon, C., Held, I., Hemler, R., Horowitz, L., Klein, S., Knutson, T., Kushner, P., Langenhost, A., Lau, N.-C., Liang, Z., Malyshev, S., Milly, P. C. D., Nath, M., Ploshay, J., Ramaswamy, V., Schwarzkopf, M., Shevliakova, E., Sirutis, J., Soden, B., Stern, W., Thompson, L., Wilson, R., Wittenberg, A., , and Wyman, B. (2004). The new GFDL global atmosphere and land model AM2–LM2: Evaluation with prescribed SST simulations. *Journal of Climate*, 17:4641–4673.

Atlas R., and, H. R. N., Ardizzone J. and, L. M., and C., J. J. (2009). The cross-calibrated, multi-platform (CCMP) ocean surface wind product: Current status and plans. *AGU Fall Meeting Abstracts*, pages 157–174.

Bacastow, R. B. (1976). Modulation of atmospheric carbon dioxide by the Southern Oscillation. *Nature*, 261(5556):116–118.

Bakker, D. C., Pfeil, B., Landa, C. S., Metzl, N., O'Brien, K. M., Olsen, A., Smith, K., Cosca, C., Harasawa, S., Jones, S. D., Nakaoka, S. I., Nojiri, Y., Schuster, U., Steinhoff, T., Sweeney, C., Takahashi, T., Tilbrook, B., Wada, C., Wanninkhof, R., Alin, S. R., Balestrini, C. F., Barbero, L., Bates, N. R., Bianchi, A. A., Bonou, F., Boutin, J., Bozec, Y., Burger, E. F., Cai, W. J., Castle, R. D., Chen, L., Chierici, M., Currie, K., Evans, W., Featherstone, C., Feely, R. A., Fransson, A., Goyet, C., Greenwood, N., Gregor, L., Hankin, S., Hardman-Mountford, N. J., Harlay, J., Hauck, J., Hoppema, M., Humphreys, M. P., Hunt, C. W., Huss, B., Ibánhez, J. S. P., Johannessen, T., Keeling, R., Kitidis, V., Körtzinger, A., Kozyr, A., Krasakopoulou, E., Kuwata, A., Landschützer, P., Lauvset, S. K., Lefèvre, N., Monaco, C. L., Manke, A., Mathis, J. T., Merlivat, L., Millero, F. J., Monteiro, P. M., Munro, D. R., Murata, A., Newberger, T., Omar, A. M., Ono, T., Paterson, K., Pearce, D., Pierrot, D., Robbins, L. L., Saito, S., Salisbury, J., Schlitzer, R., Schneider, B., Schweitzer, R., Sieger, R., Skjelvan, I., Sullivan, K. F., Sutherland, S. C., Sutton, A. J., Tadokoro, K., Telszewski, M., Tuma, M., Heuven, S. M. V., Vandemark, D., Ward, B., Watson, A. J., and Xu, S. (2016). A multi-decade record of high-quality fCO_2 data in version 3 of the surface ocean CO_2 atlas (SOCAT). *Earth System Science Data*, 8(2).

Bopp, L., Resplandy, L., Orr, J. C., Doney, S. C., Dunne, J. P., Gehlen, M., Halloran, P., Heinze, C., Ilyina, T., Séférian, R., Tjiputra, J., and Vichi, M. (2013). Multiple stressors of ocean ecosystems in the 21st century: projections with CMIP5 models. *Biogeosciences*, (10).

Burger, F. A. and Frölicher, T. L. (2023). Drivers of surface ocean acidity extremes in an earth system model. *Global Biogeochemical Cycles*, 37(9).

Carter, B. R., Feely, R. A., Williams, N. L., Dickson, A. G., Fong, M. B., and Takeshita, Y. (2018). Updated methods for global locally interpolated estimation of alkalinity, pH, and nitrate. *Limnology and Oceanography: Methods*, 16(2):119–131.

Chau, T. T. T., Gehlen, M., and Chevallier, F. (2022). A seamless ensemble-based reconstruction of surface ocean pCO_2 and air-sea CO_2 fluxes over the global coastal and open oceans. *Biogeosciences*, 19:1087–1109.

Cheung, W. W. L. and Frölicher, T. L. (2020). Marine heatwaves exacerbate climate change impacts for fsheries in the northeast pacific. *Scientific Reports*, 10.

Cheung, W. W. L., Frölicher, T. L., Lam, V. W. Y., Oyinlola, M. A., Reygondeau, G., Sumaila, U. R., Tai, T. C., Teh, L. C. L., and Wabnitz, C. C. C. (2021). Marine high temperature extremes amplify the impacts of climate change on fish and fisheries. *Science Advances*, 7(40).

Ciais, P., Sabine, C., Bala, G., Bopp, L., Brovkin, V., Canadell, J., Chhabra, A., DeFries, R., Galloway, J., Heimann, M., Jones, C., Quéré, C. L., Myneni, R., Piao, S., P. Thornton [Stocker, T.F., D. Q. G.-K. P. M. T. S. A. J. B. A. N. Y. X. V. B., and (eds.)], P. M. (2013). Carbon and other biogeochemical cycles. in: Climate change 2013: The physical science basis. contribution of Working Group I to the fifth assessment report of the Intergovernmental Panel on Climate Change. Technical report, Cambridge University Press, Cambridge, United Kingdom and New York, NY, USA.

Collins, M., Sutherland, M., Bouwer, L., Cheong, S.-M., Frölicher, T., Jacot Des Combes, H., Koll Roxy, M., Losada, I., McInnes, K., Ratter, B., Rivera-Arriaga, E., Susanto, R., Swingedouw, D., and Tibig, L. (2019). Extremes, abrupt changes and managing risk. in: IPCC special report on the ocean and cryosphere in a changing climate. Technical report, Cambridge University Press.

Denvil-Sommer, A., Gehlen, M., Vrac, M., and Mejia, C. (2019). LSCE-FFNN-v1: A two-step neural network model for the reconstruction of surface ocean pCO_2 over the global ocean. *Geoscientific Model Development*, 12(5):2091–2105.

DeVris, T. (2022). The ocean carbon cycle. *Annual Review of Environment and Resources*, 46:317–341.

Dickson, A., Chris, S., and Christian, J. (2007). Guide to best practices for ocean CO_2 measurements PICES special publication 3. Technical report, North Pacific Marine Science Organization.

Dickson, A. G. (1990). Thermodynamics of the dissociation of boric acid in synthetic seawater from 273.15 to 318.15 k. *Deep Sea Research Part A. Oceanographic Research Papers*, 37:755–766.

Doney, S. C., Lima, I., Feely, R. A., Glover, D. M., Lindsay, K., Mahowald, N., Moore, J. K., and Wanninkhof, R. (2009). Mechanisms governing interannual variability in upper-ocean inorganic carbon system and air–sea CO_2 fluxes: Physical climate and atmospheric dust. *Deep Sea Research Part II: Topical Studies in Oceanography*, 56(8):640–655.

Duke, P. J., Hamme, R. C., Ianson, D., Landschützer, P., Ahmed, M. M. M., Swart, N. C., and Covert, P. A. (2023). Estimating marine carbon uptake in the northeast Pacific using a neural network approach. *Biogeosciences*, 20:3919–3941.

Dunne, J. P., Gnanadesikan, A., Sarmiento, J. L., and Slater, R. D. (2010). Technical description of the prototype version (v0) of tracers of phytoplankton with allometric zooplankton (TOPAZ) ocean biogeochemical model as used in the princeton ifmip model. *Biogeosciences*, 7:3593.

Dunne, J. P., John, J. G., Adcroft, A. J., Griffies, S. M., Hallberg, R. W., Shevliakova, E., Stouffer, R. J., Cooke, W., Dunne, K. A., Harrison, M. J., Krasting, J. P., Malyshev, S. L., Milly, P. C. D., Phillipps, P. J., Sentman, L. T., Samuels, B. L., Spelman, M. J., Winton, M., Wittenberg, A. T., and Zadeh, N. (2012). GFDL's ESM2M global coupled climate–carbon earth system models. part I: Physical formulation and baseline simulation characteristics. *Journal of Climate*, 25:6646–6665.

Dunne, J. P., John, J. G., Shevliakova, E., Stouffer, R. J., Krasting, J. P., Malyshev, S. L., Milly, P. C. D., Sentman, L. T., Adcroft, A. J., Cooke, W., Dunne, K. A., Griffies, S. M., Hallberg, R. W., Harrison, M. J., Levy, H., Wittenberg, A. T., Phillips, P. J., and Zadeh, N. (2013). GFDL's ESM2M global coupled climate–carbon earth system models. part II: Carbon system formulation and baseline simulation characteristics. *Journal of Climate*, 26(7):2247 – 2267.

Edwing, K., Wu, Z., Lu, W., Li, X., Cai, W.-J., and Yan, X.-H. (2024). Impact of marine heatwaves on air-sea CO_2 flux along the US east coast. *Geophysical Research Letters*, 51(1).

Fay, A. R., Gregor, L., Landschützer, P., McKinley, G. A., Gruber, N., Gehlen, M., Iida, Y., Laruelle, G. G., Rödenbeck, C., Roobaert, A., and Zeng, J. (2021). Seaflux: Harmonization of air-sea CO_2 fluxes from surface pCO_2 data products using a standardized approach. *Earth System Science Data*, 13(10):4693 – 4710.

Fay, A. R. and McKinley, G. A. (2017). Correlations of surface ocean pCO_2 to satellite chlorophyll on monthly to interannual timescales. *Global Biogeochemical Cycles*, 31(3):436–455.

Feely, R. A., Boutin, J., Cosca, C., Dandonneau, Y., Etcheto, J., Inoue, H. Y., Ishill, M., Corinne, L. Q., Mackey, D. J., McPhaden, M., Metzl, N., Poisson, A., and Wanninkhof, R. (2002). Seasonal and interannual variability of CO_2 in the equatorial pacific. *Deep-Sea Research Part II: Topical Studies in Oceanography*, 49:2443–2469.

Friedlingstein, P., O'Sullivan, M., Jones, M. W., Andrew, R. M., Gregor, L., Hauck, J., Quéré, C. L., Luijkx, I. T., Olsen, A., Peters, G. P., Peters, W., Pongratz, J., Schwingshackl, C., Sitch, S., Canadell, J. G., Ciais, P., Jackson, R. B., Alin, S. R., Alkama, R., Arneth, A., Arora, V. K., Bates, N. R., Becker, M., Bellouin, N., Bittig, H. C., Bopp, L., Chevallier, F., Chini, L. P., Cronin, M., Evans, W., Falk, S., Feely, R. A., Gasser, T., Gehlen, M., Gkritzalis, T., Gloege, L., Grassi, G., Gruber, N., Özgür Gürses, Harris, I., Hefner, M., Houghton, R. A., Hurtt, G. C., Iida, Y., Ilyina, T., Jain, A. K., Jersild, A., Kadono, K., Kato, E., Kennedy, D., Goldewijk, K. K., Knauer, J., Korsbakken, J. I., Landschützer, P., Lefèvre, N., Lindsay, K., Liu, J., Liu, Z., Marland, G., Mayot, N., McGrath, M. J., Metzl, N., Monacci, N. M., Munro, D. R., Nakaoka, S.-I., Niwa, Y., O'Brien, K., Ono, T., Palmer, P. I., Pan, N., Pierrot, D., Pocock, K., Poulter, B., Resplandy, L., Robertson, E., Rödenbeck, C., Rodriguez, C., Rosan, T. M., Schwinger, J., Séférian, R., Shutler, J. D., Skjelvan, I., Steinhoff, T., Sun, Q., Sutton, A. J., Sweeney, C., Takao, S., Tanhua, T., Tans, P. P., Tian, X., Tian, H., Tilbrook, B., Tsujino, H., Tubiello, F., van der Werf, G. R., Walker, A. P., Wanninkhof, R., Whitehead, C., Wranne, A. W., Wright, R., Yuan, W., Yue, C., Yue, X., Zaehle, S., Zeng, J., and Zheng, B. (2022). Global carbon budget 2022. *Earth System Science Data*, 13(14):4811–4900.

Frölicher, T. L., Fischer, E. M., and Gruber, N. (2018). Marine heatwaves under global warming. *Nature*, 560:360–364.

Frölicher, T. L. and Laufkötter, C. (2018). Emerging risks from marine heat waves. *Nature Communications*, 9.

Frölicher, T. L., Sarmiento, J. L., Paynter, D. J., Dunne, J. P., Krasting, J. P., and Winton, M. (2015). Dominance of the Southern Ocean in anthropogenic carbon and heat uptake in CMIP5 models. *Journal of Climate*, 28(2):862–886.

Gilbert, K., Bennett, P. C., Wolfe, W., Zhang, T., and Romanak, K. D. (2016). CO_2 solubility in aqueous solutions containing Na^+, Ca^{2+}, Cl^-, SO_4^{2-} and HCO_{3^-}: The effects of electrostricted water and ion hydration thermodynamics. *Applied Geochemistry*, 67:59–67.

Gregor, L., Lebehot, A. D., Kok, S., and Scheel Monteiro, P. M. (2019). A comparative assessment of the uncertainties of global surface ocean CO_2 estimates using a machine-learning ensemble (CSIR-ML6 version 2019a) – have we hit the wall? *Geoscientific Model Development*, 12:5113–5136.

Griffies, S. M. (2009). Elements of MOM4p1. Technical Report 6, GFDL Ocean Group.

Gruber, N., Gloor, M., Fletcher, S. E. M., Doney, S. C., Dutkiewicz, S., Follows, M. J., Markus Gerber, Andrew R. Jacobson, F. J., Lindsay, K., Menemenlis, D., Anne Mouchet, S. A. M., Sarmiento, J. L., , and Takahashi, T. (2009). Oceanic sources, sinks, and transport of atmospheric CO_2. *Global Biogeochemical Cycles*, 23.

Gupta, M., Follows, M. J., and Lauderdale, J. M. (2020). The effect of antarctic sea ice on Southern Ocean carbon outgassing: Capping versus light attenuation. *Global Biogeochemical Cycles*, 34(8).

Hersbach, H., Bell, B., Berrisford, P., Hirahara, S., Horányi, A., Muñoz-Sabater, J., Nicolas, J., Peubey, C., Radu, R., Schepers, D., Simmons, A., Soci, C., Abdalla, S., Abellan, X., Balsamo, G., Bechtold, P., Biavati, G., Bidlot, J., Bonavita, M., De Chiara, G., Dahlgren, P., Dee, D., Diamantakis, M., Dragani, R., Flemming, J., Forbes, R., Fuentes, M., Geer, A., Haimberger, L., Healy, S., Hogan, R. J., Hólm, E., Janisková, M., Keeley, S., Laloyaux, P., Lopez, P., Lupu, C., Radnoti, G., de Rosnay, P., Rozum, I., Vamborg, F., Villaume, S., and Thépaut, J.-N. (2020). The ERA5 global reanalysis. *Quarterly Journal of the Royal Meteorological Society*, 146:1999–2049.

Hobday, A. J., Alexander, L. V., Perkins, S. E., Smale, D. A., Straub, S. C., Oliver, E. C., Benthuysen, J. A., Burrows, M. T., Donat, M. G., Feng, M., Holbrook, N. J., Moore, P. J., Scannell, H. A., Gupta, A. S., and Wernberg, T. (2016). A hierarchical approach to defining marine heatwaves. *Progress in Oceanography*, 141:227–238.

Holbrook, N., Scannell, H. A., Gupta, A. S., Benthuysen, J. A., Feng, M., Oliver, E. C. J., Alexander, L. V., Burrows, M. T., Donat, M. G., Hobday, A. J., Moore, P. J., Perkins-Kirkpatrick, S. E., Smale, D. A., Straub, S. C., and Wernberg, T. (2019). A global assessment of marine heatwaves and their drivers. *Nature Communications*, 10.

Huang, B., Liu, C., Banzon, V., Freeman, E., Graham, G., Hankins, B., Smith, T., and Zhang, H. M. (2021). Improvements of the daily optimum interpolation sea surface temperature (DOISST, Version 2.1. *Journal of Climate*, 34(8).

Hughes, T., Kerry, J., Alvarez-Noriega, M., Álvarez Romero, J., Anderson, K., Baird, A., Babcock, R., Beger, M., Bellwood, D., Berkelmans, R., Bridge, T., Butler, I., Byrne, M., Cantin, N., Comeau, S., Connolly, S., Cumming, G., Dalton, S., Diaz-Pulido, G., and Wilson, S. (2017). Global warming and recurrent mass bleaching of corals. *Nature*, 543:373–377.

Iida, Y., Y., T., A., K., and Ishii, M. (2020). Global trends of ocean CO_2 sink and ocean acidifcation: an observation-based reconstruction of surface ocean inorganic carbon variables. *Journal of Oceanography*, 77:323–358.

Jiang, L.-Q., Dunne, J., Carter, B. R., Tjiputra, J. F., Terhaar, J., Sharp, J. D., Olsen, A., Alin, S., Bakker, D. C. E., Feely, R. A., Gattuso, J.-P., Hogan, P., Ilyina, T., Lange, N., Lauvset, S. K., Lewis, E. R., Lovato, T., Palmieri, J., Santana-Falcón, Y., Schwinger, J., Séférian, R., Strand, G., Swart, N., Tanhua, T., Tsujino, H., Wanninkhof, R., Watanabe, M., Yamamoto, A., and Ziehn, T. (2023). Global surface ocean acidification indicators from 1750 to 2100. *Journal of Advances in Modeling Earth Systems*, 15(3).

Jähne, B., Münnich, K. O., BöSinger, R., Dutzi, A., Huber, W., and Libner, P. (1987). On the parameters influencing air-water gas exchange. *Journal of Geophysical Research: Oceans*, 92(C2):1937–1949.

Kalnay, E., Kanamitsu, M., Kistler, R., Collins, W., Deaven, D., Gandin, L., Iredell, M., Saha, S., White, G., Woollen, J., Zhu, Y., Chelliah, M., Ebisuzaki, W., Higgins, W., Janowiak, J., Mo, K. C., Ropelewski, C., Wang, J., Leetmaa, A., Reynolds, R., Jenne, R., and Joseph, D. (1996). The NCEP/NCAR 40-year reanalysis project. *Bulletin of the American Meteorological Society*, 77:437–472.

Kanamitsu, M., Ebisuzaki, W., Woollen, J., Yang, S.-K., Hnilo, J. J., Fiorino, M., and Potter, G. L. (2002). NCEP–DOE AMIP-II reanalysis. *Bulletin of the American Meteorological Society*, 83:1631–1644.

Keeling, C. D. and Revelle, R. (1985). Effects of El Nino/Southern Oscillation on the atmospheric content of carbon dioxide. *Meteoritics*, 20(2).

Kobayashi, S., Ota, Y., Harada, Y., Ebita, A., Moriya, M., Onoda, H., Onogi, K., Kamahori, H., Kobayashi, C., Endo, H., Miyaoka, K., and Takahasi, K. (2015). The JRA-55 reanalysis: General specifications and basic characteristics. *Journal of the Meteorological Society of Japan*, 93:5–48.

Landschützer, P., Gruber, N., and Bakker, D. C. E. (2020a). An observation-based global monthly gridded sea surface pCO_2 product from 1982 onward and its monthly climatology. *NOAA National Centers for Environmental Information.*

Landschützer, P., Gruber, N., Bakker, D. C. E., and Schuster, U. (2014). Recent variability of the global ocean carbon sink. *Global Biogeochemical Cycles*, 28(9):927–949.

Landschützer, P., Laruelle, G. G., Roobaert, A., and Regnier, P. (2020b). A uniform $p\mathrm{CO}_2$, climatology combining open and coastal oceans. *Earth System Science Data*, 12:2537–2553.

Landschützer, P., Tanhua, T., Behncke, J., and Keppler, L. (2023). Sailing through the Southern Seas of air–sea CO_2 flux uncertainty. *Philosophical Transactions of the Royal Society A: Mathematical, Physical and Engineering Sciences*, 381(2249).

Laufkötter, C., Zscheischler, J., and Frölicher, T. L. (2020). High-impact marine heatwaves attributable to human-induced global warming. *Science*, 369(6511):1621–1625.

Le Grix, N., Zscheischler, J., Rodgers, K., Yamaguchi, R., and Frölicher, T. L. (2022). Hotspots and drivers of compound marine heatwave and low net primary production extremes. *Biogeosciences*, 19:5807–5835.

Lee, J.-Y., Marotzke, J., Bala, G., Cao, L., S. Corti, a. J. D., Engelbrecht, F., Fischer, E., Fyfe, J., Jones, C., Maycock, A., Mutemi, J., Ndiaye, O., Panickal, S., and Zhou, T. (2021). Future global climate: Scenario-based projections and nearterm information. In Climate Change 2021: The Physical Science Basis. Contribution of Working Group I to the Sixth Assessment Report of the Intergovernmental Panel on Climate Change. Technical report, Intergovernmental Panel on Climate Change.

LeGrix, N., Zscheischler, J., Laufkötter, C., Rousseaux, C. S., and Frölicher, T. L. (2021). Compound high-temperature and low-chlorophyll extremes in the ocean over the satellite period. *Biogeosciences*, 18(6).

Lerner, P., Romanou, A., Kelley, M., Romanski, J., Ruedy, R., and Russell, G. (2021). Drivers of air-sea CO_2 flux seasonality and its long-term changes in the nasa-giss model CMIP6 submission. *Journal of Advances in Modeling Earth Systems*, 13(2).

Lueker, T. J., Dickson, A. G., and Keeling, C. D. (2000). Ocean $p\mathrm{CO}_2$ calculated from dissolved inorganic carbon, alkalinity, and equations for k1 and k2: validation based on laboratory measurements of CO_2 in gas and seawater at equilibrium. *Marine Chemistry*, 70(1):105–119.

Martin, T. and Adcroft, A. (2010). Parameterizing the fresh-water flux from land ice to ocean with interactive icebergs in a coupled climate model. *Ocean Modelling*, 34(3):111–124.

Mehrbach, C., a. C. C., Hawley, J., and Pytkowicx, R. (1973). Measurement of the apparent dissociation constants of carbonic acid in seawater at atmospheric pressure. *Limnology and Oceanography*, 18.

Metzl, N. (2021). SOCAT version 2021 for quantification of ocean CO_2 uptake. *IPSL Article Climate Science*.

Mignot, A., von Schuckmann, K., Peter Landschützer, a. F. G., van Gennip, S., Perruche, C., Lamouroux, J., and Amm, T. (2021). Projected marine heatwaves in the 21st century and the potential for ecological impact. *Frontiers in Marine Science*, 6.

Millero, F. J. (1995). Thermodynamics of the carbon dioxide system in the oceans. *Geochimica et Cosmochimica Acta*, 59(4):661–677.

Mucci, A. (1983). The solubility of calcite and aragonite in seawater at various salinities, temperatures, and one atmosphere total pressure. *American Journal of Science*, 283(7):780–799.

Naegler, T. (2009). Reconciliation of excess 14C-constrained global CO_2 piston velocity estimate. *Tellus B: Chemical and Physical Meteorology*, 61(2):372–384.

Najjar, R. G. and Orr, J. C. (1998). Design of OCMIP-2 simulations of chlorofluorocarbons, the solubility pump and common biogeochemistry.

Oliver, E. C. J., Benthuysen, J. A., Darmaraki, S., Donat, M. G., Hobday, A. J., Holbrook, N. J., Schlegel, R. W., and Gupta, A. S. (2021). Marine heatwaves. *Annual Review of Marine Science*, 13:313–342.

Oliver, E. C. J., Burrows, M. T., Donat, M. G., Sen Gupta, A., Alexander, L. V., Perkins-Kirkpatrick, S. E., Benthuysen, J. A., Hobday, A. J., Holbrook, N. J., Moore, P. J., Thomsen, M. S., Wernberg, T., and Smale, D. A. (2019). Projected marine heatwaves in the 21st century and the potential for ecological impact. *Frontiers in Marine Science*, 6.

Oliver, E. C. J., Donat, M. G., Burrows, M. T., Moore, P. J., Smale, D. A., Alexander, L. V., Benthuysen, J. A., Feng, M., Gupta, A. S., Hobday, A. J., Holbrook, N. J., Perkins-Kirkpatrick, S. E., Scannell, H. A., Straub, S. C., and Wernberg, T. (2018). Longer and more frequent marine heatwaves over the past century. *Nature Communications*, 9:1–12.

Orr, J. C. and Epitalon, J.-M. (2015). Improved routines to model the ocean carbonate system: mocsy 2.0. *Geoscientific Model Development*, 8:485–499.

Orr, J. C., Najjar, R. G., Aumont, O., Bopp, L., Bullister, J. L., Danabasoglu, G., Doney, S. C., Dunne, J. P., Dutay, J.-C., Graven, H., Griffies, S. M., John, J. G., Joos, F., Levin, I., Lindsay, K., Matear, R. J., McKinley, G. A., Mouchet, A., Oschlies, A., Romanou, A., Schlitzer, R., Tagliabue, A., Tanhua, T., and Yool, A. (2017). Biogeochemical protocols and diagnostics for the cmip6 ocean model intercomparison project (OMIP). *Geoscientific Model Development*, 10:2169–2199.

Perez, F. F. and Fraga, F. (1987). Association constant of fluoride and hydrogen ions in seawater. *Marine Chemistry*, 21(2):161–168.

Pilo, G. S., Holbrook, N. J., Kiss, A. E., and Hogg, A. M. (2019). Sensitivity of marine heatwave metrics to ocean model resolution. *Geophysical Research Letters*, 46(24):14604–14612.

Planchat, A., Kwiatkowski, L., Bopp, L., Torres, O., Christian, J. R., Butenschön, M., Lovato, T., Séférian, R., Chamberlain, M. A., Aumont, O., Watanabe, M., Yamamoto, A., Yool, A., Ilyina, T., Tsujino, H., Krumhardt, K. M., Schwinger, J., Tjiputra, J., Dunne, J. P., and Stock, C. (2023). The representation of alkalinity and the carbonate pump from CMIP5 to CMIP6 earth system models and implications for the carbon cycle. *Biogeosciences*, 20(7):1195–1257.

Reichstein, M., Michael Bahn and, Philippe Ciais and, D. F. a. M. D. M. a. S. I. S. a. J. Z. a. C. B. a. N. B. a. D. C. F. a. D. P. a. A. R. a. P. S. a. K. T. a. M. v. d. V. a. S. V. a. A. W., and Wattenbach, M. (2013). Climate extremes and the carbon cycle. *Nature*, (500):287–295.

Rödenbeck, C., Keeling, R. F., Bakker, D. C. E., Metzl, N., Olsen, A., Sabine, C., and Heimann, M. (2013). Global surface-ocean pCO_2 and sea–air CO_2 flux variability from an observation-driven ocean mixed-layer scheme. *Ocean Science*, 9:193–216.

Saba, V. S., Griffies, S. M., Anderson, W. G., Winton, M., Alexander, M. A., Delworth, T. L., Hare, J. A., Harrison, M. J., Rosati, A., Vecchi, G. A., and Zhang, R. (2016). Enhanced warming of the Northwest Atlantic Ocean under climate change. *Journal of Geophysical Research: Oceans*, 121(1):118–132.

Sabine, C. L., Feely, R. A., Gruber, N., Key, R. M., Lee, K., Bullister, J. L., Wanninkhof, R., Wong, C. S., Wallace, D. W. R., Tilbrook, B., Millero, F. J., Peng, T.-H., Kozyr, A., Ono, T., and Rios, A. F. (2004). The oceanic sink for anthropogenic CO_2. *Science*, 305(5682):367–371.

Sarmiento, J. L. and Gruber, N. (2006). *Ocean Biogeochemical Dynamics*. Princeton University Press.

Shevliakova, E., Pacala, S. W., Malyshev, S., Hurtt, G. C., Milly, P. C. D., Caspersen, J. P., Sentman, L. T., Fisk, J. P., Wirth, C., and Crevoisier, C. (2009). Carbon cycling under 300 years of land use change: Importance of the secondary vegetation sink. *Global Biogeochemical Cycles*, 23.

Smale, D. A., Wernberg, T., Oliver, E. C. J., Thomsen, M., Harvey, B. P., Straub, S. C., Burrows, M. T., Alexander, L. V., Jessica A. Benthuysen, M. G. D., Feng, M., Hobday, A. J., Holbrook, N. J., Perkins-Kirkpatrick, S. E., Scannell, H. A., Gupta, A. S., Payne, B. L., and Moore, P. J. (2019). Marine heatwaves threaten global biodiversity and the provision of ecosystem services. *Nature Climate Change*, 9:306–312.

Takahashi, T., Goddard, J. G., Chipman, D. W., Sutherland, S. C., and Olafsson, J. (1993). Seasonal variation of CO_2 and nutrients in the high-latitude surface oceans: A comparative study. 7(4).

Takahashi, T., Sutherland, S. C., Sweeney, C., Poisson, A., Metzl, N., Tilbrook, B., Bates, N., Wanninkhof, R., Feely, R. A., Sabine, C., Olafsson, J., and Nojiri, Y. (2002). Global sea–air CO_2 flux based on climatological surface ocean pCO_2, and seasonal biological and temperature effects. *Deep Sea Research Part II: Topical Studies in Oceanography*, 49(9):1601–1622.

Takahashi, T., Wallace, S., Broecker, Arnold, E., and Bainbridge (2006). The alkalinity and total carbon dioxide concentration in the world oceans. In *Carbon Cycle Modelling*.

Turi, G., Alexander, M., Lovenduski, N. S., Capotondi, A., Scott, J., Stock, C., Dunne, J., John, J., and Jacox, M. (2018). Response of O_2 and pH to ENSO in the California Current System in a high-resolution global climate model. *Ocean Science*, 14(1).

Vogt, L., Burger, F. A., Griffies, S. M., and Frölicher, T. L. (2022). Local drivers of marine heatwaves: a global analysis with an Earth System Model. *Frontiers in climate*, 4.

Wanninkhof, R. (1992). Relationship between wind speed and gas exchange over the ocean revisited. *Journal of Geophysical Research*, 97(C5):7373–7382.

Weiss, R. (1974). Carbon dioxide in water and seawater: the solubility of a non-ideal gas. *Marine Chemistry*, 2(3):203–215.

Williams, R. G. and Follows, M. J. (2011). *Ocean Dynamics and the Carbon Cycle: Principles and Mechanisms*, chapter 6 carbonate chemistry fundamentals, page 125–156. Cambridge University Press.

Winton, M. (2000). A reformulated three-layer sea ice model. *Journal of Atmospheric Oceanic Technology*, 17:525–531.

Zeng, J., Nojiri, Y., Landschützer, P., Telszewski, M., and Nakaoka, S.-i. (2014). A global surface ocean fCO_2 climatology based on a feed-forward neural network. *Journal of Atmospheric and Oceanic Technology*, 31(8):1838–1849.

Declaration of consent

on the basis of Article 30 of the RSL Phil.-nat. 18

Name/First Name: Li, Catherine

Registration Number: 21-128-038

Study program: Climate Sciences

Bachelor ☐ Master ☑ Dissertation ☐

Title of the thesis: Global Assessment of Marine Heatwaves and Their Impact on Sea-Air CO2 Fluxes

Supervisor: Prof. Dr. Thomas Frölicher

I declare herewith that this thesis is my own work and that I have not used any sources other than those stated. I have indicated the adoption of quotations as well as thoughts taken from other authors as such in the thesis. I am aware that the Senate pursuant to Article 36 paragraph 1 litera r of the University Act of 5 September, 1996 is authorized to revoke the title awarded on the basis of this thesis.

For the purposes of evaluation and verification of compliance with the declaration of originality and the regulations governing plagiarism, I hereby grant the University of Bern the right to process my personal data and to perform the acts of use this requires, in particular, to reproduce the written thesis and to store it permanently in a database, and to use said database, or to make said database available, to enable comparison with future theses submitted by others.

Bern 14.01.2024

Place/Date

Signature